SEARCHES FOR CONTINUUM AND RESONANT PRODUCTION
OF Z BOSON PAIRS USING THE ATLAS DETECTOR

Approved by:

Prof. Robert Kehoe

Prof. Fredrick Olness

Prof. Jingbo Ye

Prof. Ping Gui

SEARCHES FOR CONTINUUM AND RESONANT PRODUCTION OF Z BOSON PAIRS USING THE ATLAS DETECTOR

A Dissertation Presented to the Graduate Faculty of the

Dedman College

Southern Methodist University

in

Partial Fulfillment of the Requirements

for the degree of

Doctor of Philosophy

with a

Major in Physics

by

Azeddine Kasmi

(B.S., Oujda University (Morocco), 1999)
(M.S., North Texas University, 2004)

December 19, 2009

ACKNOWLEDGMENTS

First and foremost, I would like to express my sincere gratitude to my advisor Prof. Robert Kehoe for his continuous support of my Ph.D study and research, and for his patience, motivation, enthusiasm, and immense knowledge. His guidance helped me in all of my research and in the writing of this thesis.

My sincere thanks also go to Prof. Ryszard Stroynowski for his insight into physics, helpful ideas, support, and his original idea for a three lepton analysis. I am also grateful for his encouragement to me to pursue my own approach.

I would like to thank the members of my thesis committee: Prof. Fredrick Olness, Prof. Jingbo Ye, and Prof. Ping Gui, for their encouragement, insightful comments, and hard questions.

I am indebted to many of my colleagues during my graduate studies from whom I learned many things: David Joffe, Peter Renkel, Pavel Zarzhitsky, Haleh Hadavand, Julia Hoffman, and Daniel Goldin. I would like to thank the department staff: Shirley Melton, Carol Carroll, and Justin Ross for their help.

I would like also to thank Randy Scalise and David Joffe for proof reading my thesis as well as Profs. Roberto Vega and Kent Hornbostel who were always willing to answer my theoretical questions.

Last but not least, I would like to thank my family for their support and encouragement, especially my mother and my cousin Youssef. I would like to thank Carmen McLean for her support as well as my friends H. Yanouri, M. Deraaoui, H. Hammou, and M. Jeffali.

Kasmi , Azeddine

B.S., Oujda University (Morocco), 1999
M.S., North Texas University, 2004

Searches for Continuum and Resonant Production
of Z Boson Pairs Using the ATLAS Detector

Advisor: Professor Prof. Robert Kehoe
Doctor of Philosophy degree conferred December 19, 2009
Dissertation completed September 30, 2009

We present a search for Z boson pair production in a 3 lepton channel using the ATLAS detector at $\sqrt{s} = 14$ TeV. The search was motivated by the inefficiencies in electron reconstruction in the 4 lepton channel. Although the 3 lepton channel has a higher acceptance, it suffers from a high background which consists of $Zb\bar{b}$, Zb, WZ, and $t\bar{t}$. We used different clustering algorithms with a higher η coverage to partially identify the missing electron. The analysis was performed using Monte Carlo samples generated by different event generators, and the ATLAS detector was simulated by the GEANT4 software. We estimate a gain of 38% of the acceptance of ZZ events with respect to an explicit fully reconstructed 4 lepton final state $ZZ \rightarrow 4l$. In terms of the significance defined as $\frac{S}{\sqrt{S+B}}$, we obtain an increase from 3.6 to 4.1.

We also performed a Higgs search in the mass range of $m_H \geq 180$ GeV in the channel $H \rightarrow ZZ \rightarrow 4l$, where the two Z's are on-shell. This allowed us to use the same event selection criteria used in the case of the ZZ analysis. For a Higgs boson mass of 200 GeV, the luminosity required to achieve 5σ decreases from 6.8 fb^{-1} with a fully reconstructed 4 lepton final state to 5.4 fb^{-1} when the 3 lepton analysis is combined with the 4 lepton channel. We present also how one fares for a lower mass study.

TABLE OF CONTENTS

LIST OF FIGURES

LIST OF TABLES

This dissertation is dedicated to my mother and to the memory of my father.

Chapter 1

THE NATURE OF MASS

In our daily lives, we encounter many objects with different masses. We come to realize that it takes more effort to move a heavy object than a less heavy one. However, the origin of this mass is still a mystery. Physics in the broadest sense, long known as natural philosophy, attempts to develop a few comprehensive principles that bring together and explain physical phenomena; one of the most important of these is the existence and behavior of mass. In this dissertation, I will attempt to develop an approach to understand "the origin of mass". However, before getting to the state of the art of particle physics in the twenty-first century, I will first elaborate on the development of the relevant physical concepts.

1.1. Pre-scientific Thought and Matter

The question "What is our universe made of?" is an old question that preoccupied many previous civilizations. The proposed answer depends on time and location; for example, more than 3000 years ago the ancient Chinese used five components to describe the world. These components were metal, wood, water, fire and earth. Later on, the Greek philosophers Leucippus (first half of the fifth century) and Democritus (BC 460 $-BC$ 370) developed a theory of atomism[1] which states that all objects in the universe are composed of very small indivisible building blocks. The word "atom", an indivisible entity with fundamental properties, originates from the Greek word *atomos* which means indivisible. The idea of the atom comes from the observation that common properties of matter that are invariant in time and location. As an example, water is the same everywhere and will be the same at a later time.

[1]Such a model was also held by the Vaisesika philosophers in India.

Later the Greek philosopher Aristotle observed that the motion of material bodies requires a force. His idea was incorrect due to the lack of what is now known as "the scientific method" which consists of a set of techniques for investigating phenomena; all theoretical concepts should be tested experimentally. During the Middle Ages, Ibn Al-Haytham (AD 965 $-$ AD 1040), by his experimentation in optics, showed that rays emanate in straight lines towards the eye from every point of a visible object and hence ruled out wrong theories on how the eye interacts with light from the Greek era. This was an early version of the scientific method [1, 2].

Another important aspect of physics is its relationship with mathematics; many physical concepts can be expressed in a mathematical equation, and mathematical models in physics may also have a predictive power. In the ninth century, Al-Khwarizmi (AD 780 $-$ AD 850) introduced algebra [3] which was the seed for the more modern mathematics that followed in the Renaissance. Al-Khwarizmi was solving linear and quadratic equations to find an unknown parameter using the known ones. In modern theoretical physics, one solves more complicated equations for the unknown parameters, using the same principles.

1.2. Inertia and Mass in the Classical Age

During the Renaissance era, a new view of nature emerged. In the sixteenth and seventeenth centuries, Galileo combined observation and mathematics and introduced the new understanding of the concept of inertia, which is the tendency of an object to resist changes in its state of motion [4]. Based on that, Newton introduced the three universal laws of motion [5]. The second law of Newton, in its original format, states that the time rate of change of the momentum of an object is equal to the force imposed to it in both direction and magnitude. Momentum is the quantity of motion affecting an object; it is defined as the mass multiplied by the velocity of the object. From the same law, one can derive that the acceleration of an object is given by dividing the force acting upon it by its mass. A specific mass refers to the degree of acceleration a body acquires when it

is subjected to a force. A massive body accelerates less with a given force than another body with a lesser mass. Energy describes the amount of work that can be performed by a force.

In Newton's law of gravity, the force is proportional to a gravitational "charge", which just happens to equal the inertial mass, within a scale factor which is the universal constant of gravitation G; gravitation is a fundamental force in nature. It is a force of attraction between massive objects and it has an infinite range. Although the mass is a key ingredient of Newtonian mechanics, it is difficult to imagine what the "origin of mass" would be in the Newtonian framework. By the nineteenth century, the general consensus was that matter consists of solid indivisible particles arranged into molecules to give materials their different properties.

During the late nineteenth century, matter was thought to be composed of fundamental atoms interacting via the two fundamental forces known at that time: gravity and electromagnetism. Mendeleev classified several dozen of these naturally occurring elements into what is known as the periodic table. The classification was based on the properties of the atoms; more elements were found or produced later.

1.3. The Modern Conception of Mass and Energy

In early 1800's, experiment was in favor of the wave-like nature of light proposed by Huygens. It showed interference patterns similar to those of water waves. Later on, Maxwell placed this on a theoretical foundation when he demonstrated that electric and magnetic fields travel through space in the form of waves, and at the constant speed of light [6]. The electromagnetic force which affects electrically charged particles is another one of the fundamental forces. The electric charge is a fundamental conserved property of some subatomic particles, which determines their electromagnetic interaction. It has an infinite range and it is 10^{36} times stronger than gravity.

In 1905, Einstein introduced special relativity [7]. In that same year, Einstein introduced his famous equation $E = mc^2$ which states that energy can be expressed in terms

of mass [8]. Einstein also explained the photoelectric effect, a phenomenon in which electrons are emitted from the surface of a metal under electromagnetic radiation, by considering that light behaves as a collection of particles called "photons" or "quanta" from the quantization of energy due to Max Planck. The electron is ejected by a single photon with the photon transferring its energy to the electron. The compositeness of the atom was confirmed by Rutherford in 1911 via the gold foil experiment. The α particles, positive ions of Helium, were scattered at high angles from a gold atom which led to the conclusion of the existence of the positively charged atomic nucleus. Later, the nucleus was found to be composed of protons and neutrons bound by a strong force felt over nuclear distance scales.

The discovery of radioactivity by Henri Becquerel in 1896 opened a new era of physics with new ideas about mass, and energy. The force that is associated with radioactivity is known as the weak force. It is called the weak force as its strength is of the order of 10^{-3} the strength of the electromagnetic force.

In 1926, Erwin Schrödinger used the de Broglie wave concept, in which matter particles have a wave-like nature, to develop an equation that yields the properties of a Hydrogen atom. The Schrödinger equation describes the behavior of a quantum system via the means of waves and accommodates the wave-particle duality in a consistent manner. This is known as "wave mechanics" [9]. The interesting thing about quantum mechanics is that one cannot predict from the wave function exactly what an individual particle's behavior is, rather one gets probabilities of possible outcomes. Werner Heisenberg introduced a new mathematical approach known as "matrix mechanics" to explain quantum systems [10]. The major consequence of Heisenberg's theory is the "uncertainty principle" $\Delta x \Delta p \geq \frac{\hbar}{2}$ which is the realization that the more precisely the position of a particle is determined, the less precisely the momentum is known in this instant.

In 1927, P.A.M. Dirac combined the theories of relativity and electromagnetism with quantum mechanics to create "Quantum Electrodynamics (QED)". It describes all phenomena involving electrically charged particles interacting by means of the electromag-

netic force, whether the interaction is between light and matter or between two charged particles. The photon is the force carrier of the electromagnetic force as shown in Figure 1.1. The formulation of QED is entirely in terms of the quantum waves even though the word particle is used to describe both charged particles (electrons) and the photon. Although exact solutions of QED are very complicated, one can approximate the solution very accurately using a technique known as "perturbation theory". The coupling constant which measures the strength of the interaction, ($\alpha_e = \frac{1}{137}$), is much less than 1 which allows the perturbation theory to find solutions; one starts with the exact solution of a related problem and keeps adding the next most complicated situation. The higher terms in the expansion are progressively less important to the final numerical result. In fact, each term is smaller than its precedent by a factor of 137. Therefore, accurate results can be achieved by taking into account the first few terms only. QED is a cornerstone of particle physics and it is currently the most accurately tested physical theory. In the Hydrogen atom, α_e was measured to 12 decimal places. There is a very convenient pictorial representation of QED that is due to Richard Feynman. These representations, called Feynman diagrams, are associated with definite mathematical rules that specify how likely the process they depict is to occur. Figure 1.1 shows a space-time picture of two electrons (a solid line with arrow) that interact with each other via the exchange of a "virtual" photon (a wiggly line). A virtual photon is simply one that gets emitted and absorbed without having a significant lifetime to be observed which is a consequence of the uncertainty principle.

The protons and neutrons are made of "quarks" glued together by "gluons". The quarks are fundamental particles and gluons are elementary expressions of quark interaction. The quarks also come in different flavors and only two of these flavors are involved in ordinary matter, u(up) and d(down). Just as QED was devised to explain interactions between photons and electrons, the theory of quarks and gluons is called quantum chromodynamics (QCD). Unlike QED which has only one type of charge, the electric charge, QCD has three different types of charge which are called colors. QCD also has

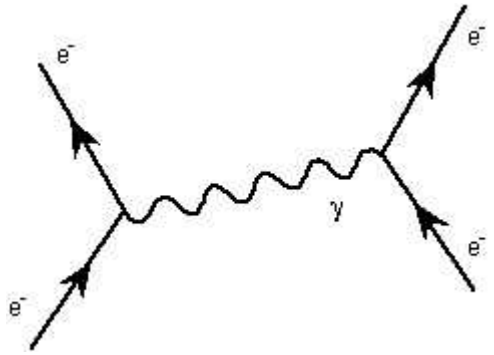

Figure 1.1. Feynman diagram showing a QED process: electron-electron scattering.

eight colored gluons with possible interactions between themselves. The force that is responsible for holding the nuclei of the atom together and binding quarks into nucleons is called the "strong force". It is very strong, but very short ranged because its messenger particle is the gluon which self-couples. The building blocks of matter are fermions, or 1/2 integer spin particles, respecting the Pauli exclusion principle which states that two identical fermions can not occupy the same quantum state simultaneously. However, the force carriers are bosons, or integer spin particles, which therefore are not constrained by Pauli's principle. The description of fundamental interactions is based on symmetry which became a key ingredient in theoretical physics. Symmetry means invariance under certain kinds of transformation. Salam and Weinberg combined the weak theory and electromagnetism into a partial unified theory called "electroweak theory". The particles (W and Z bosons), the weak force carriers, were observed at the CERN laboratory in 1983 with their predicted masses. One other final consequence of the electroweak theory is the prediction of another boson known as the Higgs boson.

Our current understanding of the matter particles and the force carriers is summarized in Figure 1.2.

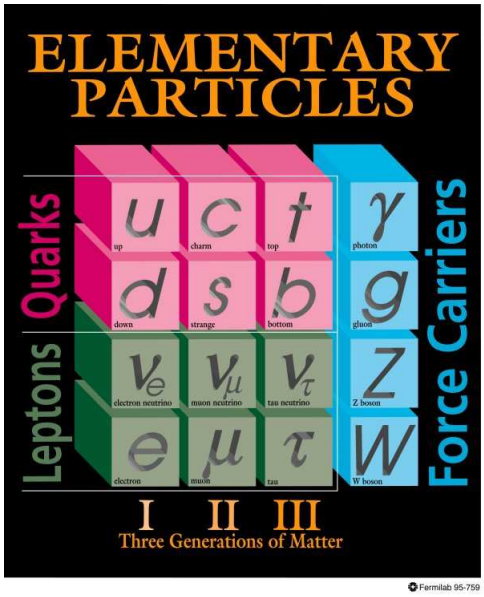

Figure 1.2. Matter particles (fermions) and force carriers (bosons).

1.4. Elementary Particle Physics Today

It is believed that particles acquire mass due to electroweak interactions with the Higgs boson, but the question is what is the mechanism. In the midst of this conundrum lies the notion of symmetry. In that case, symmetry has to do with the "vacuum" which is defined as the lowest possible energy state (not empty space). When the vacuum is at its lowest energy state, a collapse of symmetry will appear and "break" the symmetry. This breaking of symmetry is called "spontaneous symmetry breaking". This is the mechanism by which particles acquire mass. It is believed that at the Big Bang a field known as the "Higgs" field existed in a perfect symmetry. The Higgs field was not stable and with the universe cooling down, it moved to an asymmetrical lowest energy state [11, 12, 13, 14]. As the massless particles move through this "condensate" of the Higgs field, they experience a drag that manifests itself as a mass. Furthermore, the theory predicts the existence of a new particle that is the messenger of the Higgs field called the "Higgs boson". The mass of the new hypothetical particle is a free parameter in the theory. If this theory is right,

we would owe our existence to this broken symmetry without which we would not be here trying to understand it.

Particle physics is a branch of physics that endeavors to comprehend the elementary constituents of matter and their interactions. It is also known as high energy physics as many elementary particles do not occur in nature under normal circumstances, but they can be generated using energetic collisions via particle accelerators. At the Large Hadron collider (LHC), the equation $m = E/c^2$ comes to life again. Two beams of protons will be accelerated to energies comparable to the speed of light. The result of the collision between these two proton beams will be studied via the ATLAS detector.

1.5. Purpose of this Thesis

Because the existence of the Higgs boson is crucial for the electroweak model, the discovery of the Higgs boson is one of the primary goals of the LHC. The Higgs boson mass is a free parameter in the theory. However, it is expected to be in the range of $114 - 157$ GeV, at the 95% confidence level due to direct searches and electroweak precision measurements. The cleanest experimental signature for a Higgs boson discovery is its decay to four leptons (electrons and muons), $H \rightarrow ZZ \rightarrow 4l$. Moreover, this channel provides a potential discovery over a wide range of the expected Higgs boson mass. With excellent energy resolution and linearity of reconstructed leptons, one should expect a narrow 4-lepton invariant mass peak on top of a smooth background. The major component of the background is the Z pair production $pp \rightarrow ZZ \rightarrow 4l$. Furthermore, the triple-gauge couplings (ZZZ and $ZZ\gamma$) are absent and ZZ searches provide a test for any gauge-coupling anomalies. There are inefficiencies in electron reconstruction which reduce the acceptance of the four-lepton channel. Therefore, I conducted a search for the Z-boson pair as well as the Higgs boson in a three-lepton channel using Monte Carlo samples.

In this thesis, I will review the electroweak model and its aspects that favor the existence of the Higgs boson as well as Z pair production (Chapter 2). I will present

the current experimental limits for the Higgs search. I will conclude the chapter with expected production and decay mechanisms and their implications for the search as well as a motivation for the three-lepton searches.

In Chapter 3, I describe very briefly the LHC and give a detailed description of the subsystems of the ATLAS detector. Moreover, I will discuss my contributions in calibration of the electronics of the liquid argon calorimeter. I discuss in Chapter 4 the different event generators used to generate signal events as well as background events and some possible triggering aspects of the analysis. Chapter 5 provides explanations of particle reconstruction algorithms used in ATLAS and some aspects of my contributions in lepton identification and optimization.

In Chapter 6, I discuss my attempt of the three lepton selection analysis. I developed a set of techniques for partially reconstructed electrons which I discuss in Chapter 7 followed by results of the ZZ searches in Chapter 8. I present my results on the Higgs-boson search in Chapter 9 followed by a conclusion for these two searches in Chapter 10.

Chapter 2

FUNDAMENTAL INTERACTIONS

2.1. Gauge Interactions

The theory of group representation provides the ideal framework for a mathematical description of the symmetries in nature. A gauge theory is a field theory in which the Lagrangian is invariant under a certain continuous group of transformations. In such theories, the interaction is invariant under a phase or a "gauge" that changes from one space-time point to another. In general, a gauge invariance leads to conserved quantities such as charge in electromagnetism. A local gauge invariance dictates that the interactions be mediated via gauge bosons. Consequently, particular types of gauge invariance fix the form of possible interactions. For example, non-Abelian local gauge invariance results in self interactions of the mediating gauge boson.

2.2. Electroweak Interactions

2.2.1. Gauge Structure

Salam and Weinberg synthesized the experimental observations of the weak and the electromagnetic interactions into a local gauge theory based on the product $SU(2) \times U(1)$ [15]. The conserved property in the $SU(2)$ group is a quantum property of particles known as the weak isospin T. Furthermore, each one of the three generators of the $SU(2)$ group is associated with a gauge boson W^i, with $i = 1, 2, 3$ [16]. Likewise, the group $U(1)$ is associated with one gauge boson B_o. The group $U(1)$ is related to the conservation of a new quantum quantity known as the weak hypercharge Y. These four generators can be associated with four symmetries. However, we see the symmetry only in one particular combination of the four generators, $T^{1,2,3}$ and Y, which corresponds to a conservation of

the electromagnetic charge.

$$Q = T^3 + \frac{Y}{2} \tag{2.1}$$

where Q is the electromagnetic charge and T^3 is the third component of the weak isospin. The mathematical structure of the theory is such that all the gauge bosons are massless. Moreover, matter particles (fermions) should also be massless. However, the W and Z bosons are found to be massive. Only particular combinations of the massless gauge eigenstates $W^{1,2,3}$ and B_o lead to four physical states with well defined electromagnetic charges:

$$\begin{aligned} W^{\pm} &= \frac{1}{\sqrt{2}}(W^1 \pm iW^2) \\ Z &= W^3 \cos\theta_W - B_o \sin\theta_W \\ \gamma &= W^3 \sin\theta_W + B_o \cos\theta_W \end{aligned} \tag{2.2}$$

where θ_W is the weak mixing angle which is determined experimentally. There are two neutral gauge bosons and one of them should correspond to a photon γ as shown in Equation 2.2. The electroweak theory is based on two groups with independent coupling strengths, g for $SU(2)$ and g' for $U(1)$. The fact that the two couplings g and g' are still different makes the unification partial. The relation between these coupling constants and the electromagnetic charge e is expressed by

$$g \sin\theta_W = g' \cos\theta_W = e. \tag{2.3}$$

The weak force is a short range force. This is due to the enormous masses of the force carriers, W and Z bosons. However, gauge invariance requires massless bosons. To reconcile this impasse, one can make use of the Higgs mechanism. The mathematical structure of the gauge theory and the structure imposed by the Higgs mechanism leads

the gauge bosons $W^{\pm}$ and Z of the weak interaction to gain mass while the photon γ remains massless.

2.2.2. Higgs Mechanism

The mass is generated by the Higgs boson via a mechanism of spontaneously broken symmetry [17]. In the Lagrangian, massive particles will be represented by fields with terms quadratic in those fields. For the W boson, the quadratic term of the field will be $M_W^2 W_\mu W^\mu$. However, these quadratic terms in the fields are prohibited by the $SU(2)_L \times U(1)_Y$ gauge symmetry. The Higgs mechanism is a way of generating the mass terms while obeying the gauge symmetry. This is done by adding a complex scalar field with a corresponding Lagrangian [16]:

$$L = (D_\mu \phi)^\dagger D_\mu \phi - \mu^2 \phi^\dagger \phi - \lambda(\phi^\dagger \phi)^2 \tag{2.4}$$

where ϕ is the Higgs field, λ and μ^2 are constants. The covariant derivative is defined as $D_\mu = \partial_\mu + igW_\mu + ig'B_\mu$. The first term in the Lagrangian is the kinetic energy term and the last two terms are for potential energy. This Lagrangian obeys the electroweak gauge symmetry. However, the ground state of this system does not; it is through this loophole that mass terms can arise in the SM. We can see how this works by looking at the potential energy term of the Lagrangian. To illustrate the Higgs mechanism, one can begin with the "toy" example of a singlet complex scalar field. It is more convenient to write the Higgs field in terms of two real scalar fields, ϕ_1 and ϕ_2

$$\phi = \phi_1 + i\phi_2. \tag{2.5}$$

If $\mu^2 < 0$ and $\lambda > 0$, the potential will have the form in Figure 2.1 and the minimum of the potential can be expressed as:

$$\phi^\dagger \phi = (\phi_1^2 + \phi_2^2) = v^2 \tag{2.6}$$

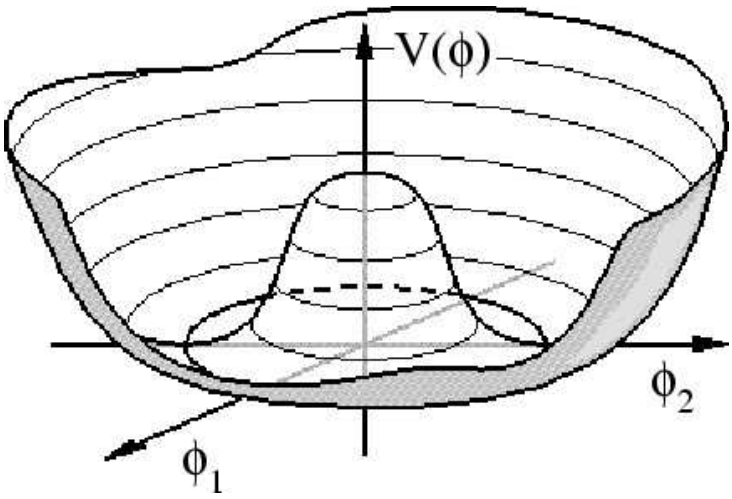

Figure 2.1. Higgs field potential "Mexican hat".

where v is the vacuum expectation value of the Higgs field which is equal to 246 GeV.

The crucial observation is that the minimum of the potential (the ground state) is not at the origin. The ground state is at any point on the circle of radius "v" as shown in Figure 2.1. Nature selects a unique ground state, one point on this circle and thus we say that the ground state breaks the symmetry. The symmetry remains in any point on the circle. This is known as the "spontaneous symmetry breaking".

Now, one can address the case of the SM $SU(2)_L \times U(1)_Y$ gauge symmetry. In this case, the Higgs mechanism is a complex doublet, and it breaks the gauge symmetry to a $U(1)_Q$. The electric charge operator Q is associated with this unbroken symmetry and thus charge is conserved and the photon remains massless. Therefore, the physical state of the Higgs field eigenstates must be charge conserved and only the neutral components of this Higgs field can develop a vacuum expectation value.

$$\phi = \begin{pmatrix} \phi^+ \\ \phi^0 \end{pmatrix}, \tag{2.7}$$

$$< \phi >_0 =< 0|\phi|0 >= \begin{pmatrix} 0 \\ \frac{v}{\sqrt{2}} \end{pmatrix}, \tag{2.8}$$

with $v = (\frac{\mu^2}{\lambda})^{\frac{1}{2}}$. Using gauge invariance, one can select the following form which contains only the real Higgs field while the charged Higgs field is gauged away. This is known as the unitary gauge.[18]. Finally, one expands the Higgs field ϕ about the vacuum expectation value.

$$\phi(x) = \begin{pmatrix} 0 \\ \frac{v+h(x)}{\sqrt{2}} \end{pmatrix}. \tag{2.9}$$

Once we substitute this field in (Eqn. 2.9) in the electroweak Lagrangian in Equation 2.4, one finds the quadratic terms in the field representing the mass term [16].

$$M_W = \frac{1}{2}vg \tag{2.10}$$

$$M_Z = \frac{1}{2}v\sqrt{g^2 + g'^2} \tag{2.11}$$

$$M_\gamma = 0 \tag{2.12}$$

Thus three weak bosons gain mass via the Higgs field and the photon remains massless. At the tree level, equations 2.10 and 2.11 can be combined via the Weinberg angle as follows:

$$\frac{M_W}{M_Z} = \cos\theta_W \tag{2.13}$$

The mass of the W and Z bosons can be expressed as shown in equation 2.14 [18], where G_F is the Fermi coupling constant.

$$M_W^2 = \frac{e^2 G_F}{\sqrt{32}\sin^2\theta_W} \quad GeV^2$$
$$M_Z^2 = \frac{e^2 G_F}{\sqrt{2}\sin^2 2\theta_W} \quad GeV^2 \tag{2.14}$$

The model was constructed in order that the photon would stay massless; therefore, $M_\gamma = 0$ in Equation 2.12 is not a prediction. However, the result of Equation 2.13 is a prediction of the theory.

The Higgs mechanism is a very efficient theory as it generates mass not only for the gauge bosons, but also for the matter particles, the fermions. In the case of fermions, the mass term of the form $-m\psi\overline{\psi}$ which mixes left-handed and right-handed fermions is excluded by gauge invariance. However, we can generate the mass for fermions by adding a term such as,

$$L_{He} = -g_e\overline{\psi}\phi\psi \tag{2.15}$$

This term is for the case of an electron where g_e is the electron Yukawa coupling which is not fixed by the theory, and $\psi = (\nu, e)$. The complex scalar field ϕ is an $SU(2)_L$ doublet, $\bar{e_L}$ is an $SU(2)$ doublet, and e_R is a right-handed singlet; particles with spin in the same direction as their momentum are called right-handed, otherwise they are called left-handed. The Lagrangian L_{He} is gauge invariant. When ϕ is replaced by the value of Eq. 2.9, the Lagrangian becomes:

$$L_{He} = -\frac{g_e}{\sqrt{2}}v(\bar{e_L}e_R) - \frac{g_e}{\sqrt{2}}h(\bar{e_L}e_R) \tag{2.16}$$

$$L_{He} = -m_e\bar{e}e - \frac{g_e}{\sqrt{2}}h(\bar{e}e). \tag{2.17}$$

The first term between parenthesis in the Lagrangian is just $\overline{\psi}\psi$ so it is the mass term $m_e\bar{e}e$. The second term is an interaction term that gives the amplitude for the fermion to interact with a physical Higgs particle. Note that the coupling of the Higgs field to fermions is proportional to the mass of fermions which makes it hard to discover the Higgs boson via its decay to lighter fermions. The mass of the electron can be expressed as:

$$m_e = \frac{g_e}{\sqrt{2}}v \tag{2.18}$$

The Yukawa coupling is not fixed by the theory; thus, the fermions masses are not predicted by the theory.

2.2.3. Three Gauge Couplings

The electroweak interaction predicts very precisely the couplings between gauge bosons due to the non-Abelian gauge symmetry $SU(2)_L \times U(1)_Y$. The self-interactions are described by the Triple-Gauge Couplings (TGC), WWV, $Z\gamma$V, and ZZV (V =γ,Z) . Vector-boson pair production provides sensitive ground for direct tests of the TGC. Any deviations of the couplings from the expected values would be a sign of new physics as the triple-neutral gauge couplings (ZZZ and $ZZ\gamma$) are absent in the theory (Figure 2.2) and ZZ searches provide a test for any gauge-coupling anomalies. The ZZ events are also an important background for the Higgs boson in its 4-lepton decay mode, particularly at high mass [19]. The existence of the Higgs boson will manifest itself by a peak in the invariant mass distribution of the Z boson pair. Therefore, it is important to evaluate precisely the production rate of the ZZ continuum in order to get a realistic estimate of the signal-to-background ratio.

In the massless fermion limit, the most general form of a vertex for an on-shell Z is shown in Figure 2.3. It respects the Lorentz invariance and electromagnetic gauge invariance and can be written as [20]:

$$g_{ZZV}\Gamma^{\alpha\beta\mu}_{ZZV} = e\frac{P^2 - M_V^2}{M_Z^2}[if_4^V(P^\alpha g^{\mu\beta} + P^\beta g^{\mu\alpha}) + if_5^V\epsilon^{\mu\alpha\beta\rho}(q_1 - q_2)_\rho] \tag{2.19}$$

where M_Z is the Z boson mass and e is the electron charge. The factor $(P^2 - M_V^2)$ is a consequence of the fact that identical bosons are not allowed in an odd partial wave, and is due to the electromagnetic gauge invariance for the $ZZ\gamma$ couplings. The effective Lagrangian is [21]:

$$L = -\frac{e}{M_Z^2}[f_4^V(\partial_\mu V^{\mu\beta})Z_\alpha(\partial^\alpha Z_\beta) + f_5^V(\partial^\sigma V_{\sigma\mu})\tilde{Z}^{\mu\beta}Z_\beta] \tag{2.20}$$

where $V_{\mu\nu} = \partial_\mu V_\nu - \partial_\nu V_\mu$ and $\tilde{Z}^{\mu\beta} = \frac{1}{2}\epsilon_{\mu\nu\rho\sigma}Z^{\rho\sigma}$. The couplings f_i^V (i=4,5) are dimensionless complex functions of q_1^2, q_2^2 and they are P^2 and C odd. The coupling f_4^V is forbidden by CP invariance and f_5^V is required to vanish by parity conservation. In the SM, $f_4^V = f_5^V = 0$ at the tree level. However, the terms f_5^V that are CP invariant have contributions at one-loop level. These contributions are of the order 10^{-4} [22].

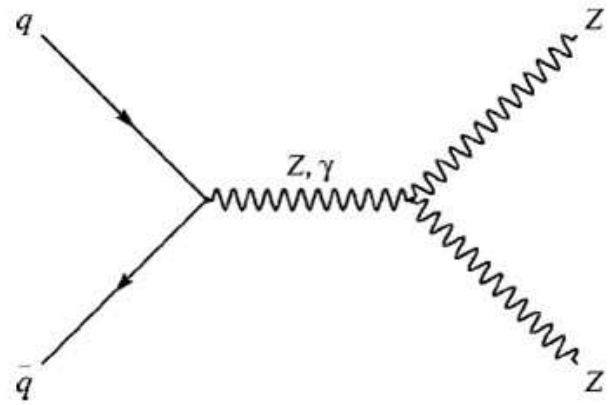

Figure 2.2. The (ZZZ and $ZZ\gamma$) diagrams of forbidden contributions to Z pair production

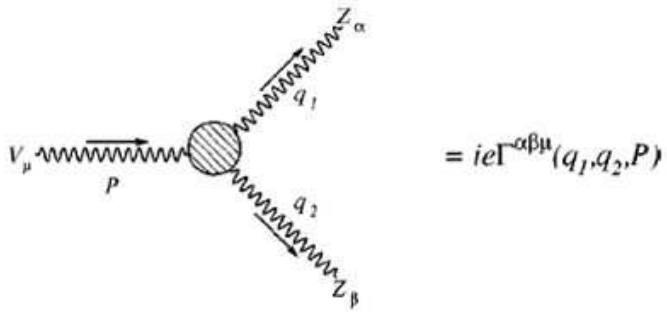

Figure 2.3. A general $ZZV(V = Z\gamma)$ vertex.

2.3. Strong Interactions

The strong interactions are described by a non-Abelian gauge group $SU(3)$ theory of color interaction known as quantum chromodynamics (QCD). The force carriers of QCD are eight gluons which are vector bosons. The gluons themselves carry color which makes interaction between gluons possible.

Isolated color-charged particles do not occur in nature because quarks are confined in colorless objects in groups of two (mesons) or three (baryons). The mesons are combinations of a quark and anti-quark with opposite color charge, such as $\pi^0(u, \overline{u})$, which makes the object colorless. Baryons such as protons and neutrons are composed of quarks with red, green, and blue color charges. The reason for quark confinement is due to the force-carrying gluons themselves having color charge. As two quarks separate, the strong force potential increases with the separation distance unlike the Coulomb force. Because of this behavior, the color force experienced by the quarks in the direction to hold them together remains constant regardless of their distance from each other. Therefore, there will be enough energy to create a quark-anti-quark pair out of the vacuum. This is known as hadronisation or fragmentation.

Perturbation theory is not applicable to QCD as the strength of the strong coupling is generally very large. However, at very high energies, quarks and gluons interact more

weakly, and the coupling constant becomes small enough to perform perturbative calculations. This is known as "asymptotic freedom". Moreover, asymptotic freedom and confinement are continuous; there is no phase-transition line that would clearly separate them.

The hadronisation process can not be calculated via perturbation theory. However, many phenomenological models are used for that purpose. The cluster fragmentation model relies on the phase space of the jets by ordering the color singlet clusters onto the continuum of high-mass mesonic resonances. These clusters decay to lighter well-known resonances and stable hadrons using pure 2 body phase-space decay and phase-space weight. In the string fragmentation model, the field lines are assumed to be compressed into a tube-like region or "string". The two colored partons can be connected via the string. The two particles oscillate on this string until a $q\overline{q}$ is created along the string as shown in Figure 2.4. The new string will also oscillate and can break as well. The process continues until the invariant mass is small enough to create a hadron.

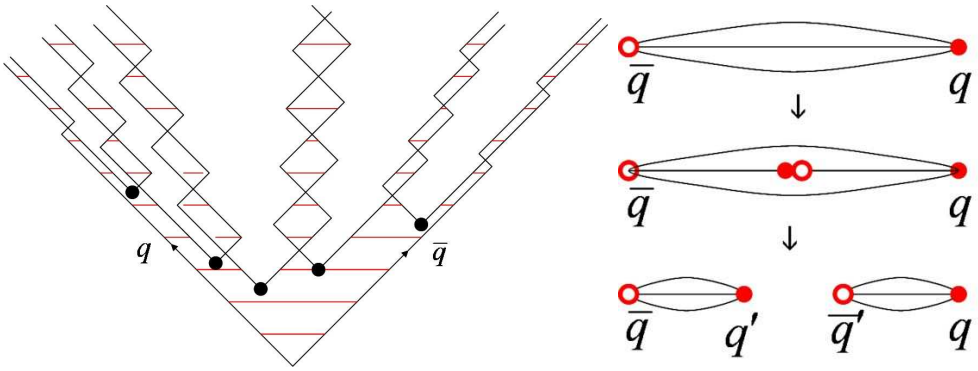

Figure 2.4. Lund String Model: quarks are held together by strings which break after a certain length and form mesons (left). Production of quark-anti-quark pairs form in the intense color field (right).

2.4. Additional Fundamental Fermions

Our current knowledge of particle physics incorporates the electroweak theory, QCD and further discoveries of the particle content in nature. This generalizes these models to

more fermion families than the original ones.

The set of experimentally verified theories in particle physics is known as the "Standard Model (SM)". The SM of particles physics consists of two parts. The first part is the particle content which comes in three generations. The generations replicate each other with heavier and unstable particles. Hence, matter is made of only the first generation as it is the only one which is stable. With accelerators, heavy and unstable particles of the second and third generation may be produced. The second part of the SM concerns the dynamics of these particles. The SM is a gauge theory of the electroweak and strong interactions with the gauge group $SU(3) \times SU(2) \times U(1)$. A summary of the SM particle content is shown on Tables 2.1 and 2.2.

2.4.1. Generations

The fermions can be grouped into quark and lepton weak isospin doublets. Only the first generation is composed of stable particles (lowest mass) due to conservation of the baryonic and leptonic numbers. Electroweak theory does not constrain the number of generations. However, experimental evidence of three generations of light non sterile fermions is extremely good. The quarks come in three generations as shown:

$$\begin{pmatrix} u \\ d \end{pmatrix}_{first} \begin{pmatrix} c \\ s \end{pmatrix}_{second} \begin{pmatrix} t \\ b \end{pmatrix}_{third} \tag{2.21}$$

The leptons are also organized in three generations:

$$\begin{pmatrix} e \\ \nu_e \end{pmatrix}_{first} \begin{pmatrix} \mu \\ \nu_\mu \end{pmatrix}_{second} \begin{pmatrix} \tau \\ \nu_\tau \end{pmatrix}_{third} \tag{2.22}$$

	Leptons			Quarks		
	flavor	mass	electric charge	flavor	mass	electric charge
The 1st generation	e	0.0005 GeV	-1	u	0.003 GeV	+2/3
	ν_e	$< 10^{-8}$ GeV	0	d	0.006 GeV	-1/3
The 2nd generation	μ	0.106 GeV	-1	c	1.3 GeV	+2/3
	ν_μ	$< 10^{-4}$ GeV	0	s	0.1 GeV	-1/3
The 3d generation	τ	1.777 GeV	-1	t	173.1 GeV	+2/3
	ν_τ	< 0.02 GeV	0	b	4.3 GeV	-1/3

Table 2.1. Standard Model fermions

Interaction	boson	mass	electric charge	spin	strength	range, m
strong	gluon	0	0	1	1	10^{-18}
electromagnetic	photon	0	0	1	10^{-2}	∞
weak	$W^{\pm}$	80.22 GeV	± 1	1	10^{-5}	10^{-14}
	Z^0	91.187 GeV	0	1		
gravity	graviton	0	0	2	10^{-38}	∞

Table 2.2. Standard Model bosons

2.5. Current Experimental Constraints on the Higgs Boson Mass

In theory, the SM Higgs mass is expected to be lower than 1 TeV to prevent the strong self-coupling of the Higgs. Many searches for the Higgs boson have been conducted, and there are constraints both via direct searches and electroweak precision measurements.

While the SM does not predict the Higgs boson mass, higher order corrections to the W boson and top masses can be used to set a limit on the Higgs boson mass. The W boson mass is related to the top mass as m_t^2, while its relation to the Higgs boson mass goes as $\log(m_H)$. This can be used to restrict the interval of allowed masses of the Higgs boson as shown in Figure 2.5.

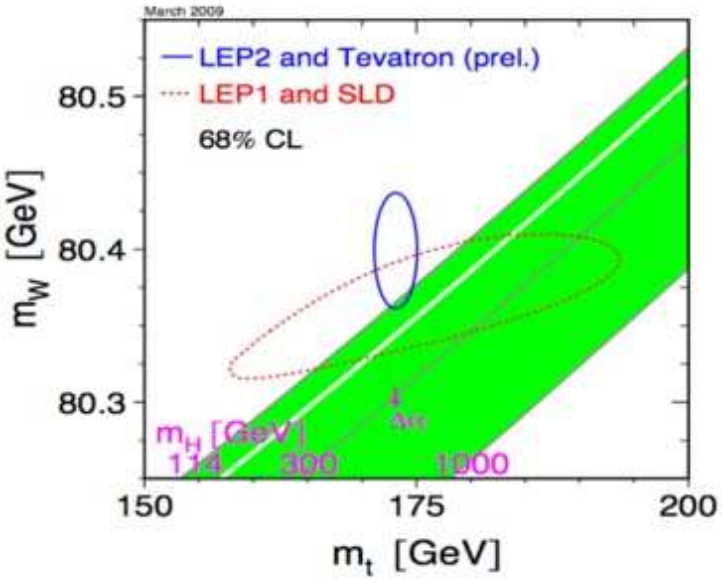

Figure 2.5. Using the precision measurement on the W and top masses to restrict the Higgs mass [24].

A direct search at LEP2 has excluded the Higgs boson with a mass lower than 114.4 GeV [23]. Recent searches at the Tevatron have excluded the region of 160-170 GeV [24]

as shown in Figure 2.6; the figure also shows a combination of the LEP2 direct search and the Tevatron electroweak results.

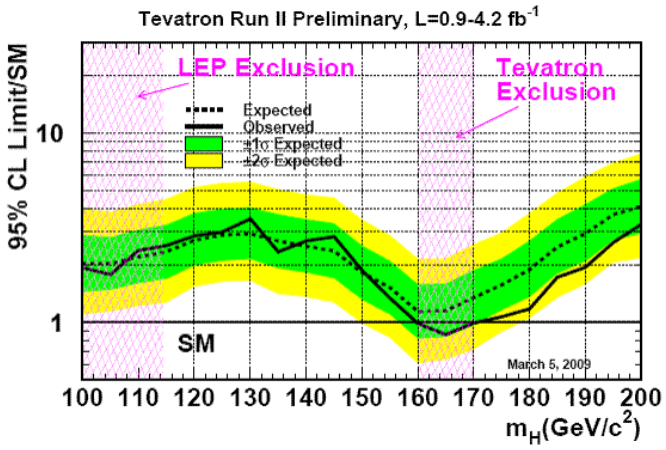

Figure 2.6. Combined searches of the Higgs from LEP and Tevatron [24].

The Figure 2.7 shows the $\Delta\chi^2$ for a global fit to the electroweak data as a function of the Higgs boson mass. In the fit, one can make use of the radiative corrections to the W boson mass which go as m_t^2 and $\log(m_H)$. The preferred value for its mass, the minimum of the curve, is 87^{+35}_{-26} GeV at 68% CL at $\chi^2 = 1$ for the black line. The theoretical uncertainty is shown as the blue band. Furthermore, the electroweak precision measurements indicate that the Higgs boson mass is lower than 157 GeV at 95% CL [25]. This includes the experimental uncertainty in m_W and m_t and the theoretical uncertainty.

2.6. Production and Decay

2.6.1. Production and Decay of Z Boson Pairs

In the SM, the main production of continuum Z pairs is $q\bar{q}$ annihilation as shown in Figure 2.8. The next to leading order (NLO) contributions are due to virtual processes (Figure 2.9a) where the gluon is emitted and absorbed by the interacting quark or the

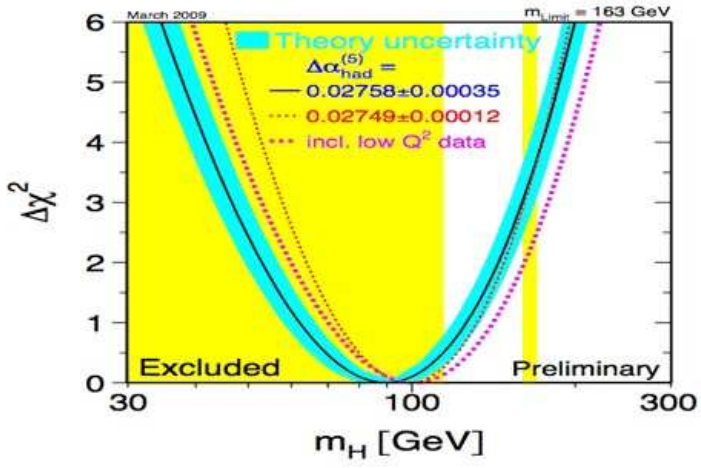

Figure 2.7. $\Delta\chi^2$ of a global fit to electroweak data as a function on the Higgs mass [24].

anti-quark. The other process is soft-gluon emission in which a gluon is emitted with the Z pair as shown in Figure 2.9b. The next to next to leading order (NNLO) contributions are due to gluon-gluon fusion [27, 26] especially at the LHC where the gluon flux is enhanced.

The total cross section of ZZ production at the LHC at 14 TeV center of mass at NLO is 16 pb [29, 27]. The NNLO contribution to the cross section is estimated to be 20%. Figure 2.10 shows Feynman diagram contributing to the process $gg \rightarrow ZZ$.

2.6.2. Production and Decay of the Higgs Boson

At the LHC, the dominant processes in Higgs production are gluon-gluon fusion, WW fusion and ZZ fusion. There are also contributions from $t\bar{t}$ fusion and Higgs bremsstrahlung from W or Z but they are less important overall. The Higgs production diagrams are shown in Figure 2.11. The cross section is expected to range between 0.1 pb and 100 pb depending on the Higgs mass. The cross section as a function of mass is shown in Figure 2.12. The coupling between the Higgs boson and the fermions is proportional to the fermion mass (Yukawa coupling), whereas the coupling between the

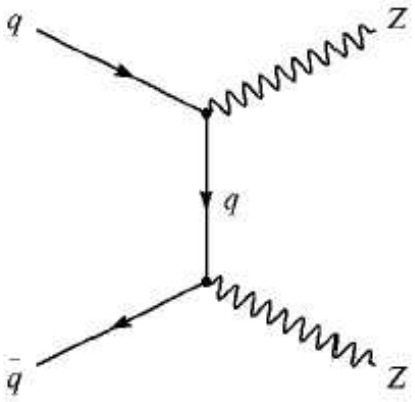

Figure 2.8. The Feynman diagram for the tree level process contributing to ZZ production in the SM

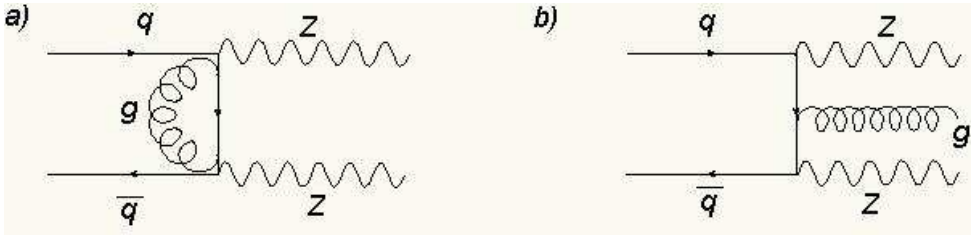

Figure 2.9. Next to Leading order contributions to ZZ production: a) Virtual subprocess $ZZ \rightarrow q\bar{q}$ b) Real emission subprocess $q\bar{q} \rightarrow ZZg$

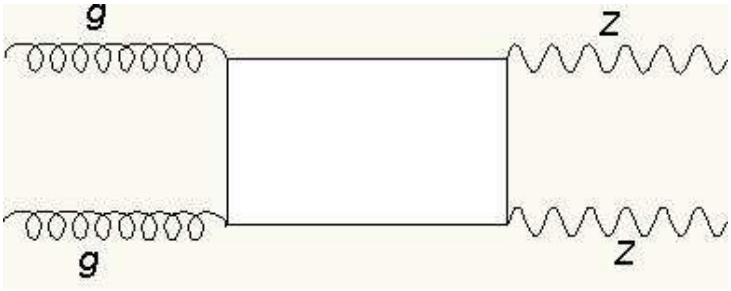

Figure 2.10. A Feynman diagram contributing to the process $gg \rightarrow ZZ$

Higgs boson and the gauge bosons is proportional to the square of the boson mass [30]. Thus, the Higgs boson will decay into heavy particles. The branching ratios for different decay channels of the Higgs boson as a function of its mass are shown in Figure 2.13.

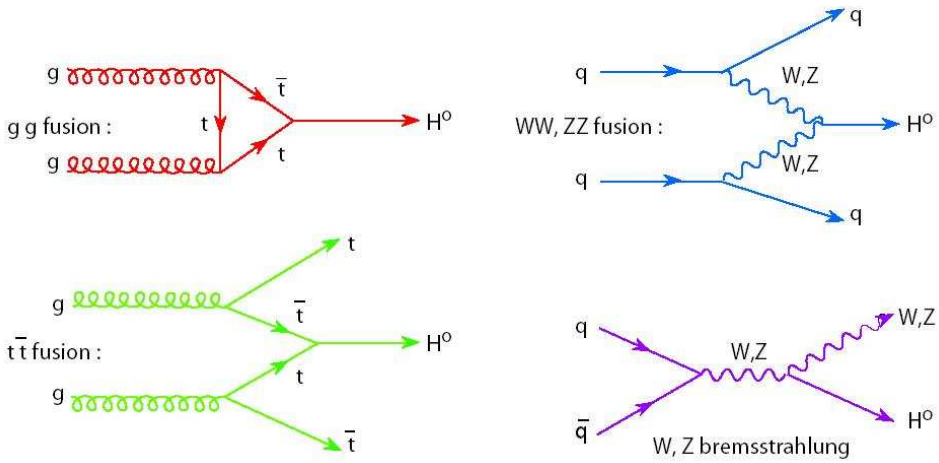

Figure 2.11. The most important processes for Higgs production at hadron colliders.

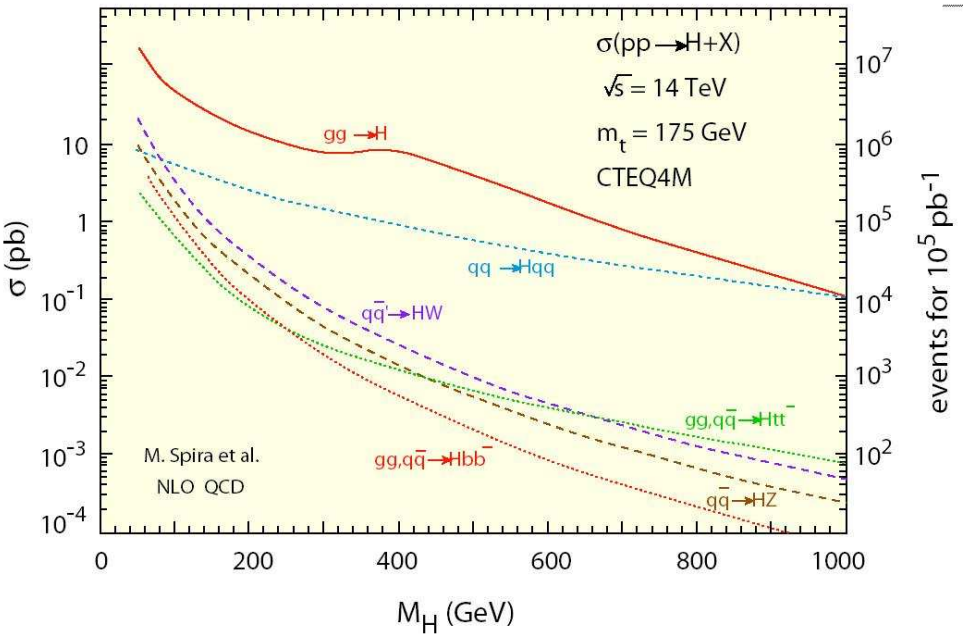

Figure 2.12. The production cross section of the SM Higgs boson for center of mass energy of 14 TeV.

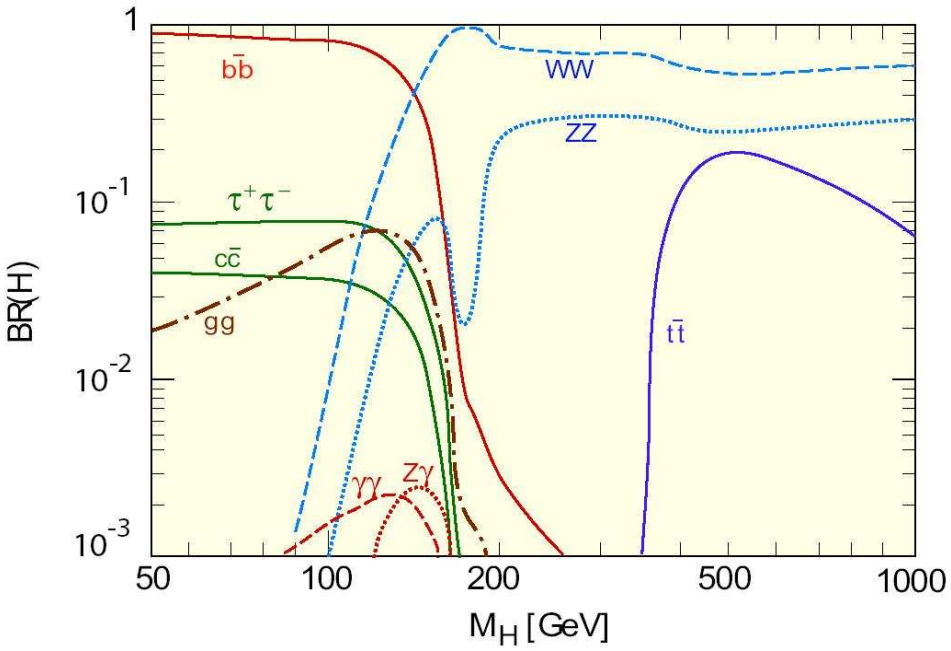

Figure 2.13. Branching ratios for different decay channels of the Higgs boson as a function of its mass.

2.7. Final States and Search Strategy

2.7.1. ZZ Final States

The branching ratio of the ZZ decay is shown in Figure 2.14. Although the decay into four leptons (e or μ) is only 0.5%, it is a very clean signature.

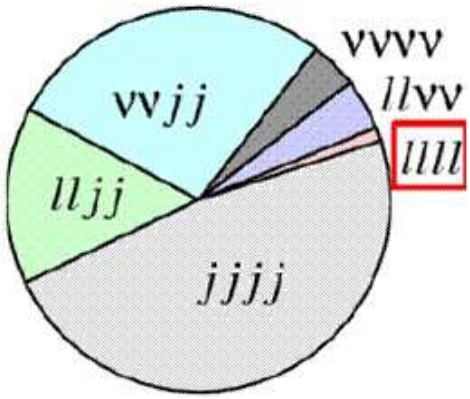

Figure 2.14. The fractions of each decay mode of ZZ. The ZZ decay to four jets dominates by approximately 50%. The decay mode into four leptons represents only a small fraction, but it is the cleanest.

2.7.2. Higgs Boson Final States

The Higgs boson has many different decay channels. Each process has a different discovery potential depending on the Higgs boson mass.

1. 80 GeV $< m_H <$120 GeV

   The heaviest particles into which the Higgs boson can decay in this mass range to a pair of b-quarks. The decay $H \longrightarrow b\bar{b}$ is dominant, but it suffers from a huge QCD background. The b-tagging technique can be used for b jet identification. If the Higgs is produced in association with W and Z, the background can be reduced by lepton triggering. In this mass range, $H \longrightarrow \gamma\gamma$ is another possible discovery channel. Despite the small branching ratio, this decay mode is promising as the signal is expected to be a resonance on the top of a background continuum. This requires an electromagnetic calorimeter with excellent momentum and mass resolution.

2. 120 GeV $< m_H < 2m_Z$=180 GeV

   The channel $H \longrightarrow ZZ^* \longrightarrow 4l^{\pm}$, where the Z^* is off-shell. This channel is very challenging as one of the Z bosons is off-shell giving low transverse momentum leptons. Moreover, The $Z + jets$ (b jets or light jets) background is very high in that region. The main background is from ZZ^* diboson production.

3. 150 GeV $< m_H < 2m_Z$ (= 182 GeV)

   In Figure 2.13, the dip on the $H \longrightarrow ZZ^*$ decay mode around the Higgs boson mass of $2m_W$ = 160 GeV is due to the decay mode $H \longrightarrow WW$ becoming dominant. This channel is characterized by missing energy due to a neutrino coming from the leptonic decay of the W.

4. $m_H >$ 180 GeV

   The mass of the Higgs boson also satisfies the threshold for a decay into two on-shell Z bosons, in which the branching ratio is high and the background is low. However, the cross section decreases with the increase of the Higgs boson mass. Therefore, the discovery potential depends on the available integrated luminosity. The $H \longrightarrow ZZ \longrightarrow 4l^{\pm}$ channel is characterized by a high branching ratio over a wide range of the Higgs mass with a low background. Furthermore, the four-lepton channel is a clean signature as the resulting leptons from the Z bosons are high p_T and isolated. Another promising channel with a higher branching ratio is

$$H \longrightarrow ZZ \longrightarrow l^+l^-\nu\nu.$$

2.7.3. The Three Lepton Strategy

The efficiency of electron reconstruction is not 100%. In fact, the efficiency of reconstructing one single electron is approximately 71% [31] depending on the cuts applied (see section 5.2.1). As a result, the reconstruction of four electrons will be the efficiency of reconstructing one electron to the power of four. Figure 2.15 shows the number of reconstructed electrons in a $ZZ \longrightarrow 4e$ event. One can see that the number of events with three reconstructed electrons (550) is twice the number of events with four reconstructed electrons (250). This observation was first made in the similar $H \longrightarrow ZZ^*$ case [32, 33], and this led to a strategy of a three-lepton analysis in that search. Based on that observation, I pursued a complementary analysis to search for ZZ and high mass $H \longrightarrow ZZ$ in the three-lepton channel. I focused on events with two on-shell Z bosons. However, the background is very high in that channel; it consists of $Zb\bar{b}, Zb, t\bar{t}$, and WZ in their decay to three leptons. To address the high background in the three-lepton channel, I developed a set of techniques to partially identify with calorimeter information alone the electron that failed reconstruction via the standard electron algorithm. The presence of the two Z resonances permits the omission of tracking requirements from the analysis. I explored particle identification requirements to the partially-identified electron to further reject fake background. Finally, I presented a full estimate of the sensitivity of a search for ZZ production and high mass Higgs production.

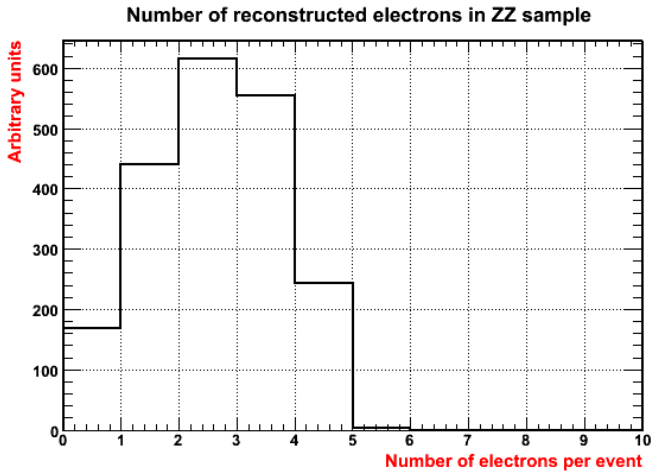

Figure 2.15. Number of electrons reconstructed in an event of $ZZ \longrightarrow 4e$.

Chapter 3

THE LHC AND THE ATLAS DETECTOR

3.1. Large Hadron Collider

The search for new particles with large masses requires very high energy particle accelerators. The first attempts to accelerate particles was based on their fall through a potential difference, acquiring an energy boost equal to the voltage across the gap multiplied by their charge. The cyclotron [34] uses the principle that charged particles are affected by a magnetic field as described by the Lorentz force law, $\overrightarrow{F} = q\overrightarrow{v} \times \overrightarrow{B}$. Thus, magnets are used to bend charged particles around in circles through high voltage electrodes. This way, an accelerating voltage could be used more than once. Resonant frequency (RF) cavities, a hollow pillbox of few tens of centimeters in length, are the preferred means of accelerating particles. The RF cavities use a standing wave whose frequency is set such that it gives particles an accelerating push as they pass through. For example, if a series of electron bunches are being accelerated then the sign of the wave will flip from positive to negative as the bunch passes through the cavity, returning to positive as the next bunch arrives. Currently, most accelerators are synchrotrons, in which two beams of particles are accelerated to a high energy to collide head on. The only way to see the particles from these collisions is via their interaction with matter. Therefore, a device called a detector is built at a point where beams are focused and made to collide.

One consequence of Maxwells's equations is that charged particles radiate electromagnetic energy when accelerated or bent by a magnet. The only way to minimize these losses for a collision energy of several TeV, is to use the most massive stable charged particles: protons. Although the synchrotron radiation is reduced by accelerating protons, protons have a complication due to their compositeness. The fundamental interactions in

a proton-proton collision are between the proton's partonic constituents. One difficulty in proton collisions comes from the lack of information about the momentum of these constituents. The constituents, quarks or gluons, carry only a fraction x_f from the proton's momentum.

The proton-proton colliders are characterized by a huge QCD background. Figure 3.1 shows the predicted cross sections of processes expected at the LHC as a function of the center of mass energy of the collision. The cross sections of physics processes at the LHC are much higher than they are at the Tevatron. This is especially true for the Higgs-boson cross section.

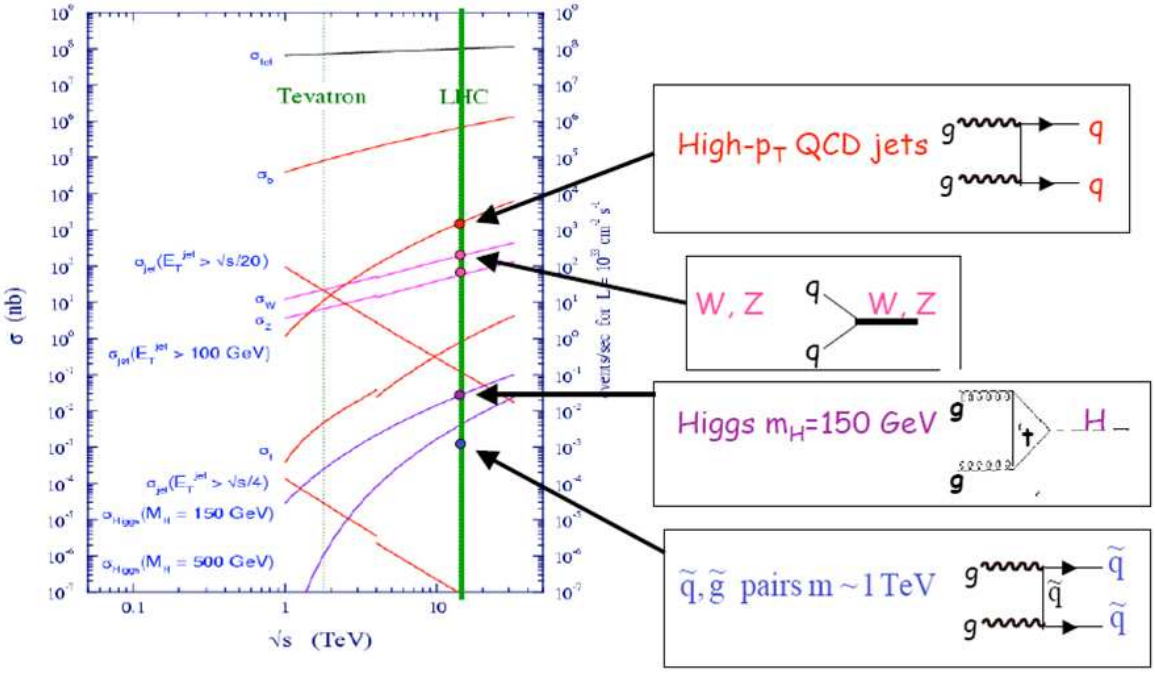

Figure 3.1. Expected proton-proton cross sections as a function of the center of mass energy.

The Large Hadron Collider (LHC) (Figure 3.2) at CERN will be at the energy frontier in high energy physics. It is located at the Franco-Swiss border with a circumference of 27 kilometers and at a depth of approximately 100 meters underground. At the LHC, protons

will be grouped in bunches of 10^{11} particles and accelerated. The bunches are spaced 25 ns apart at design operation which is equivalent to 7.5 m in distance. The collision rate is 40 MHz. The protons are accelerated in several steps before being injected in the main ring and travel 20 minutes before reaching a maximum energy of 7 TeV. If the two colliding proton bunches have both cross-sectional area A and contain N particles, each particle in one bunch will "see" a fraction of the cross-sectional area of the other bunch $N\sigma_{int}/A$. The interaction cross section σ_{int} is the total area of overlap of two colliding particles. Thus, the number of interactions per passage of two such bunches is $N^2\sigma_{int}/A$. The interaction rate R will be:

$$R = f\frac{N^2}{A}\sigma_{int} \tag{3.1}$$

where f is the frequency of bunch collisions. The notion of luminosity $\mathcal{L}$ is very critical for establishing the quantity of data taken; it is defined as the interaction rate per unit cross section:

$$\mathcal{L} = f\frac{N^2}{A} \tag{3.2}$$

The instantaneous designed luminosity of the LHC is expected to be $10^{-34}\ cm^{-2}\ s^{-1}$. Collider performance may also be characterized by the integrated luminosity over time.

The LHC is scheduled to run in 2010 with 7 TeV center of mass energy, but the physics processes studies in this dissertation correspond to 14 TeV running.

3.2. ATLAS Detector

The ATLAS experiment (Figure 3.3) consists of many detection layers arranged in a cylindrical geometry surrounding the interaction point. It has three major components: the inner detector, the calorimeters, and the muon spectrometer. There are also two magnet systems, one for the inner detector and one for the muon spectrometer to measure the momentum of charged particles. The description of the ATLAS detector relies on the

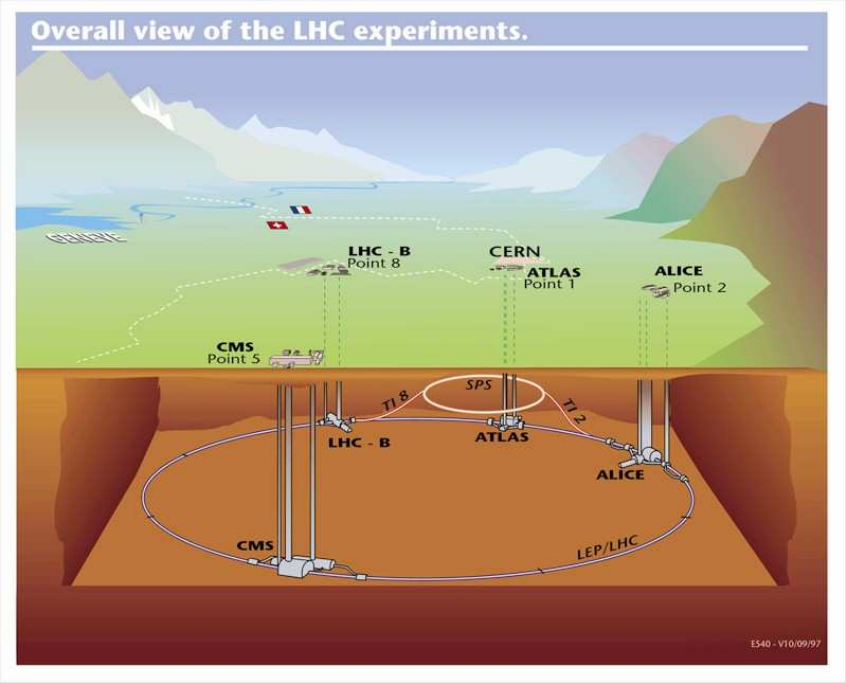

Figure 3.2. The main ring and position of the detectors at the Large Hadron Collider.

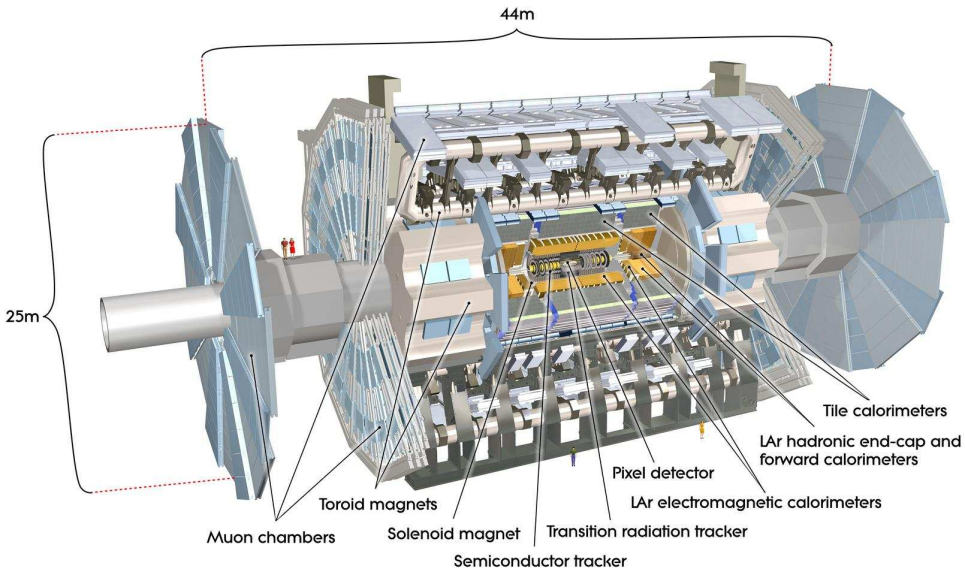

Figure 3.3. A cross section of the ATLAS detector.

technical design report [35] and the paper published by the ATLAS collaboration [36]. In the ATLAS coordinate system, the beam is along the z-axis while the x-y plane is transverse to the beam direction. The positive x-axis points to the center of the LHC while the positive y-axis points upward. θ is the polar angle of the particle direction as measured from the positive z-axis. The pseudorapidity of particles from the primary vertex is defined as $\eta = -\ln[\tan(\theta/2)]$. The azimuthal angle ϕ is measured around the beam axis. The distance ΔR in the pseudorapidity-azimuthal angle space is defined as $\Delta R = \sqrt{\Delta\eta^2 + \Delta\phi^2}$.

The ATLAS detector is designed to cover a wide range of searches for new physics. The detector is equipped with fast and radiation-hard electronics and sensor elements. It also has a large acceptance in pseudorapidity and almost full azimuthal angle coverage. The EM calorimeter offers very good energy resolution. The muon system in ATLAS has very good muon identification power as well as momentum resolution. The trigger is very efficient for low transverse-momentum objects with a good background rejection. Table 3.1 summarizes the main performance goals of the ATLAS detector.

Detector component	**Design resolution (momentum and energy)**	η **coverage**	
		Measurement	Trigger
Tracking	$\sigma_{p_T}/p_T = 0.05\%\ p_T \oplus 1\%$	± 2.5	—
EM calorimetry	$\sigma_E/E = 10\%/\sqrt{E} \oplus 0.7\%$	± 3.2	± 2.5
Hadronic calorimetry barrel,endcap,and FCAL	$\sigma_E/E = 50\%/\sqrt{E} \oplus 3\%$ $\sigma_E/E = 100\%/\sqrt{E} \oplus 10\%$	± 3.2 $3.1 < \lvert\eta\rvert < 4.9$	± 3.2 $3.1 < \lvert\eta\rvert < 4.9$
Muon spectrometer	$\sigma_{p_T}/p_T = 0.05\%\ p_T = 1\text{TeV}$	± 2.7	± 2.4

Table 3.1. General performance goals of the ATLAS detector. For high P_T muons, the muon spectrometer performance is independent of the inner-detector system [35].

3.2.1. Inner Detector

High momentum resolution and good vertex measurements are required by the benchmark physics processes in ATLAS. Therefore, one needs a fine detector resolution to achieve these high precisions. The inner detector (Figure 3.4) with its three components (Figure 3.5): silicon pixel, Semi Conductor Tracker (SCT), and the Transition Radiation Tracker (TRT) provides all the features required with radiation tolerant materials. The inner detector covers a pseudorapidity region within the range $|\eta| \leq 2.5$. The inner detector is immersed in a two-Tesla magnetic field provided by a central solenoid magnet. One can infer the charge and momentum of the particle by the direction and degree of track curvature, respectively.

The Pixel detector is composed of a 16.4×60.8 mm wafers of silicon with 46,080 pixels, of 50×400 μm^2 each. The barrel portion of the pixel detector consists of 3 cylindrical layers. These three barrel layers are made of identical staves inclined with an azimuthal angle of 20 degrees. There are 22, 38 and 52 staves in each of these layers respectively. The pixel detector has approximately 80.4 million readout channels.

The SCT system is designed to provide eight precision measurements per track in the intermediate radial range, contributing to the measurement of momentum, impact parameter and vertex position. In the barrel, the SCT has eight silicon microstrip layers. In that region, the detector uses small angle (40 mrad) stereo strips to measure coordinates. They consist of two 6.4 cm long chained sensors with a strip pitch of 80 μm. At the end-cap level, there are strips which run radially as well as stereo strips at an angle of 40 mrad. There are 6.3 million readout channels in the SCT.

The TRT is based on the straw-tube technique. The detector is composed of tubes which are filled with a gas mixture of mainly xenon (70%). The electron identification is augmented by the detection of the transition radiation photons that ionize the gas mixture in the straws. The barrel part of the TRT contains 52544 axial straws of about 150 cm length at radii between 56 cm and 107 cm. The end-caps contain a total of 319488 radial straws at radii between 64 cm and 103 cm (inner end-caps), and 48 cm and 103 cm

(outer end-caps). The combination of the TRT hits at larger radius with precision trackers at small radii allows for very good pattern recognition and high precision in both R$-\phi$ and z coordinates. The total number of TRT readout channels is approximately 351000. The TRT provides on average 36 two-dimensional measurement points with 0.170 mm resolution for charged particle tracks with $\eta < 2.5$ and $p_T > 0.5$ GeV.

3.2.2. ATLAS Magnet System

The ATLAS super-conducting magnetic system consists of one solenoid and one toroid. The overall dimensions of the magnets are 26 m in length and 20 m in diameter. The central solenoid is placed inside the EM calorimeter to provide a magnetic field for the inner detector. This is surrounded by a system of three barrel toroid magnets generating magnetic fields for the muon spectrometer and two endcap toroids that are inserted in the barrel toroids at each end and lined up with the solenoid magnet [35].

The central solenoid provides a field of 2 T, while the toroid magnets provide a non-uniform magnetic field that has an average value of 0.5 T in the barrel region and varies from 0.2 to 3.5 T in the endcap region. The momentum resolution depends on the integral $\int Bdl$ known as the bending power, where B is the azimuthal field component and the integral is taken on a straight line trajectory between the inner and outer radius of the toroids. The barrel and endcap toroids provide 2-6 Tm and 4-8 Tm, respectively in $0 \leq |\eta| < 1.3$ and $1.6 \leq |\eta| < 2.7$. The two magnets overlap in the region $1.3 \leq |\eta| < 1.6$ which results in a lower bending.

3.2.3. Calorimeters

Calorimeters are used for energy measurement purposes via the absorption and conversion of the particle's energy into a shower of particles that are detected by the sensing elements. The calorimeter measures the energies of charged and neutral particles. The liquid argon (LAr) calorimeter is designed to measure energy and identify particles that interact through the electromagnetic interaction such as electrons and photons detec-

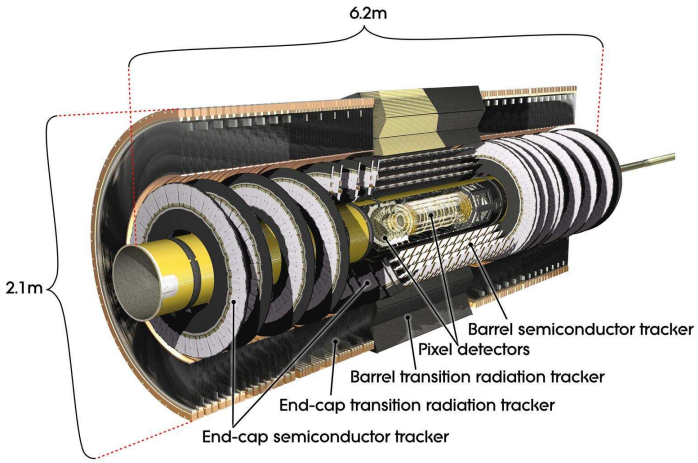

Figure 3.4. The ATLAS Inner Detector.

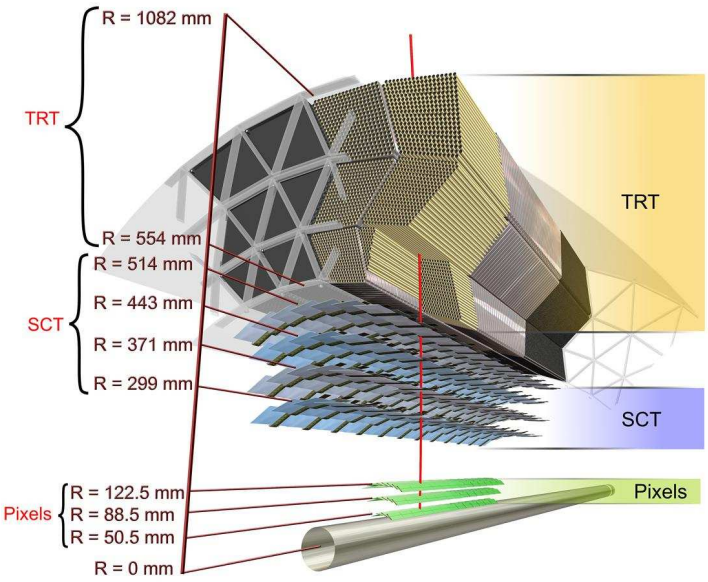

Figure 3.5. The sensors and structural elements traversed by a charged track of $p_T = 10$ GeV in the barrel inner detector ($\eta = 0.3$).

tion. The hadronic calorimeter is designed for energy measurement and identification of strongly interacting particles such as pions. It uses a sampling calorimetry approach.

Sampling calorimeters generally use sheets of heavy-material absorber alternating with layers of active material (e.g. liquid argon). The ATLAS calorimeters consist of various sampling detectors and the ones closest to the beam line are inside three cryostats, one barrel and two endcaps. The barrel cryostat contains the electromagnetic barrel calorimeter. Each of the end-cap cryostats contains an Electromagnetic End-Cap Calorimeter (EMEC), a Hadronic End-Cap calorimeter (HEC), and a Forward Calorimeter (FCAL). Liquid argon is used as the active detector medium due to its stability of response over time, and its intrinsic radiation hardness. The cryostat has the role of keeping the liquid argon at a temperature of 90K. Figure 3.6 shows the main components of the ATLAS calorimeter. The Tile calorimeter is a large hadronic sampling calorimeter which makes use of steel as the absorber material and scintillating plates as the active material. The dominant source of radiation in the ATLAS detector comes from the *pp* interaction rate, which is of the order of 109 interaction per second per collision point. Most of the particles centrally produced will be absorbed in the calorimeters, and in particular in the hadron Tile Calorimeter. This helps in controlling the amount of radiation reaching the muon system.

3.2.3.1. Electromagnetic calorimeter

The detection of particles is based on their interaction properties with matter. When a high energy electron or photon hits the lead layers of the EM calorimeter, an EM shower is produced as shown in Figure 3.7. As a consequence, the initial energy of the electron/photon is transferred into numerous low-energy particles. The gaps (4 mm) between the lead plates are filled with liquid argon and subjected to a large electric field. The electrons of the showers ionize the liquid argon. The electric field causes the ionization electrons to drift to the cathode and produces an electric signal.

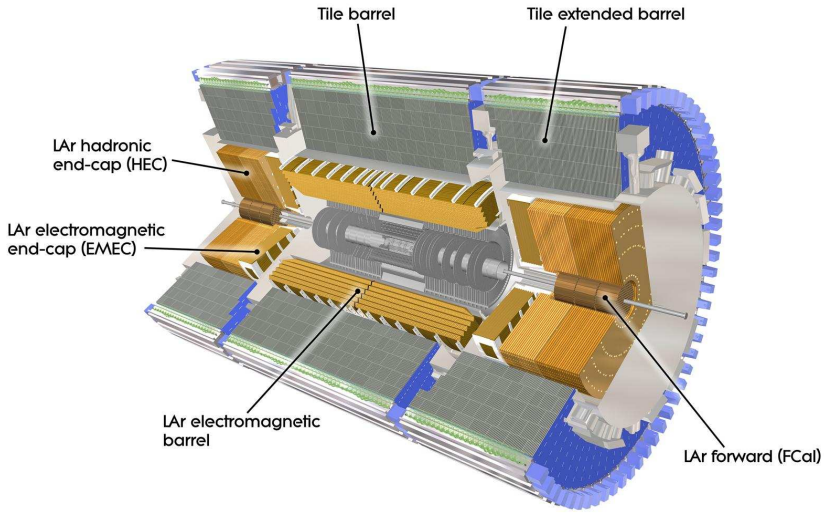

Figure 3.6. The ATLAS Calorimeters.

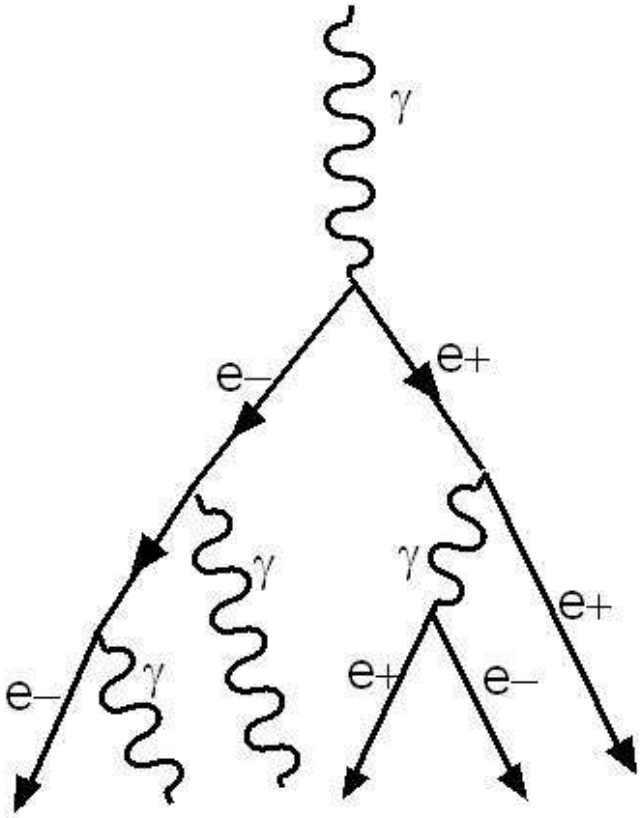

Figure 3.7. EM shower.

The radiation length (X_o) is a property of a material describing the energy loss of high-energy electromagnetically-interacting particles within the given material. It is defined as the distance over which a high-energy electron loses a fraction ($1/e$) of its energy via bremsstrahlung and 7/9 of the mean free path for conversion of high energy photons.

The ATLAS EM Calorimeter is divided into several components: an electromagnetic sampling calorimeter with "accordion-shaped" lead electrodes in the barrel ($|\eta| < 1.475$) and endcaps ($1.375 < |\eta| < 3.2$), and a forward calorimeter close to the beam pipe made from copper and tungsten to ensure the coverage of forward particles ($3.1 < |\eta| < 4.9$). The EM barrel calorimeter consists of two half-barrels (3.2 m length) around the beam axis z. The first half covers the positive z ($0 < \eta < 1.475$) while the other half covers the negative side. The accordion geometry provides full coverage in ϕ and reduces the angular dependence of the signal. Thus, a uniform performance in terms of linearity and resolution as a function of ϕ is achieved. The absorber thickness depends on η. In the barrel region, it is 1.53 mm for $|\eta| < 0.8$ and for $|\eta| > 0.8$ it is 1.13 mm. In the endcap, the plate thickness is 1.7 mm for $|\eta| < 2.5$ and 2.2 mm for $|\eta| > 2.5$. In terms of the radiation length, the total thickness ranges from 22 X_o from $|\eta| = 0$ to $|\eta| = 0.8$ to (24-33) X_o between $|\eta| = 0.8$ and $|\eta| = 1.3$.

In addition, the presampler is made of a thin layer of liquid argon (11 mm in depth) in front of the electromagnetic calorimeter. It consists of 64 identical azimuthal sectors. A single sector is 3.1 m long and 0.28 m wide with a coverage in $\Delta\eta \times \Delta\phi$ of 1.52×0.2. The presampler helps correct for the energy loss in front of the calorimeter.

The EM endcap calorimeter consists of one wheel in each side of the barrel and covers the region $1.375 < |\eta| < 3.2$. A single wheel is 63 cm thick and weighs 27000 kilograms. The total active thickness in the outer wheel ($1.475 < |\eta| < 2.5$) increases from 24 X_o to 38 X_o. In the inner wheel ($2.5 < |\eta| < 3.2$), it increases from 26 X_o to 36 X_o.

In the region $|\eta| < 2.5$, The EM calorimeter is divided into three longitudinal sections called layers. Layer 3 has a granularity of $\Delta\phi \times \Delta\eta = 0.0245 \times 0.05$ as shown in Figure 3.8. The study of the longitudinal profile of the shower is a key ingredient in particle

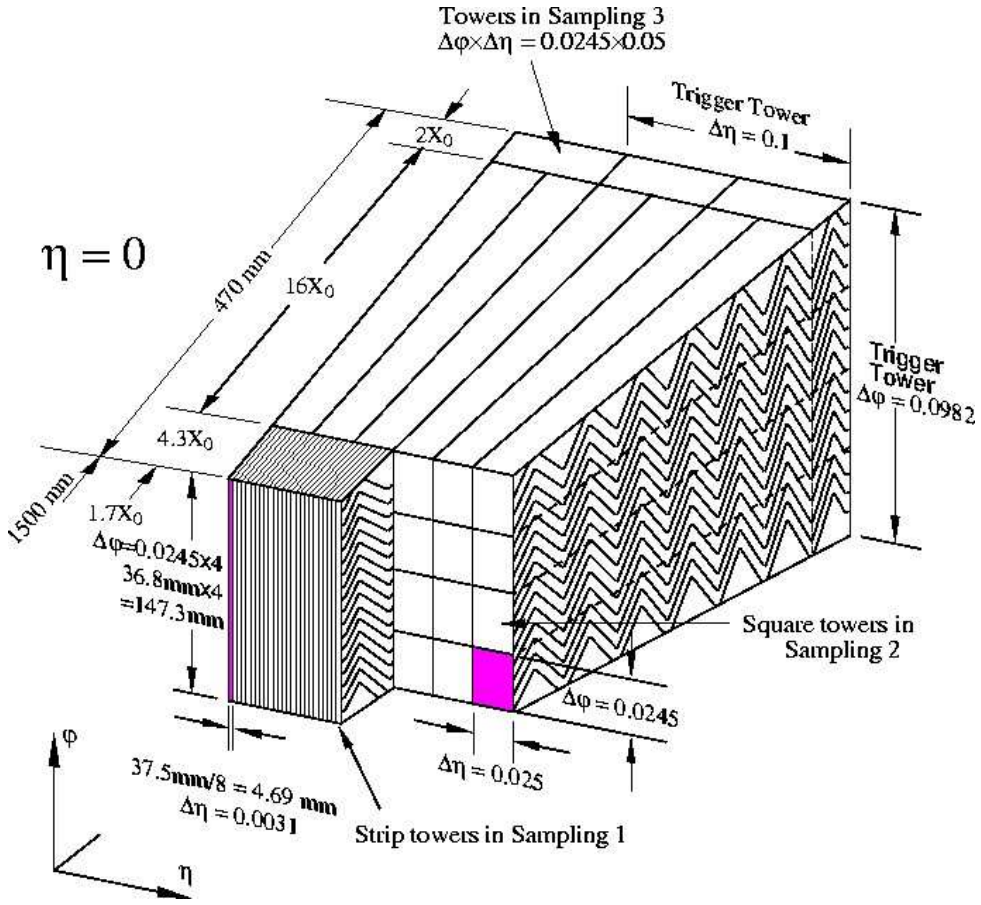

Figure 3.8. "EM Accordion shape" calorimeter cell. Four layers in depth with different cell sizes can be seen.

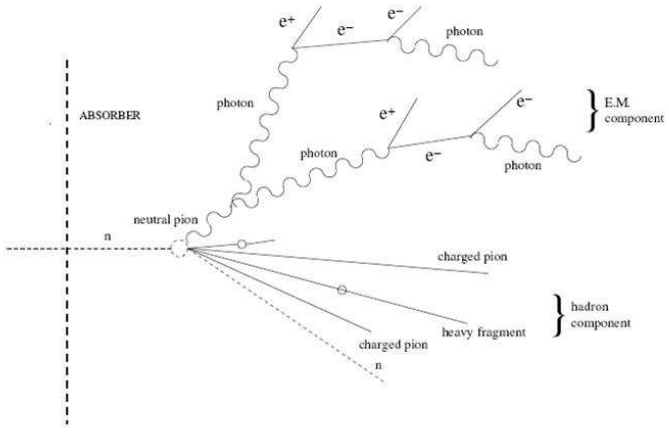

Figure 3.9. Hadronic shower.

identification.

The forward calorimeters (FCAL) are located in the same cryostats as the endcap calorimeters and provide coverage over the range ($3.1 < |\eta| < 4.9$). The location of the FCAL modules at high $|\eta|$, at a distance of 4.7 m from the interaction point, makes them exposed to high particle fluxes. The FCAL consists of three modules of 45 cm in depth each. The first one (FCAL1) is made of copper and optimized for electromagnetic measurement while the other two are made of tungsten for hadronic measurements. Table 3.2 shows the parameters for the three FCAL modules. The FCAL1 compartment is made of copper plates; each plate has 12260 holes drilled in them through which the electrode structures are inserted. An electrode consists of a co-axial copper rod and copper tube separated a radiation-hard plastic fibre wound around the rod.

3.2.3.2. Hadronic calorimeter

In order to detect hadrons, one needs to understand their interactions with matter. A hadronic shower is produced by a high-energy hadron such as a pion interacting with an atomic nucleus. Some of such particles have an electric charge, and so produce showers that are partially electromagnetic, but also interact with nuclei via the strong force. Although the details are more complex for this force, such an interaction involves one hadron interacting with a nucleus and producing several lower-energy hadrons. This continues, as with the electromagnetic shower, until all particles are stopped or absorbed in the material. The interaction length λ_o is used to describe the longitudinal shower development; it is the mean free path between two inelastic nuclear interactions. The hadronic shower is stopped in the hadronic calorimeter that surrounds the electromagnetic calorimeter. Figure 3.9 shows a schematic illustration of a hadronic shower. The ATLAS hadronic calorimeter covers a large pseudorapidity range ($|\eta| < 4.9$) and consists of three sub-detectors: the Tile calorimeter, the liquid argon hadronic endcap calorimeter (HEC) and the LAr forward calorimeter (FCAL) [35].

The Tile calorimeter is a hadronic calorimeter and consists of barrel and extended barrel components covering the range $|\eta| < 1.7$. The central barrel has a length of 5.8 m while the extended barrel has a length of 2.6 m. The inner radius of each barrel is 2.28 m and the outer radius is 4.25 m. It is segmented longitudinally into three layers with granularity of $\Delta\eta \times \Delta\phi = 0.1 \times 0.1$ and $\Delta\eta \times \Delta\phi = 0.2 \times 0.1$ for the last layer. The Tile calorimeter has 7.4 λ_o. The Tile calorimeter relies on the photomultipliers which are sensitive to light generated in the scintillator. In these detectors, the electrons released by radiation striking a photocathode are accelerated and greatly amplified. The combination of high gain, low noise, high frequency response, and large area of collection made the photomultiplier a desirable technology.

The HEC consists of two independent wheels per endcap. It is located right behind the electromagnetic calorimeter and covers the region $1.5 < |\eta| < 3.2$. Each wheel is divided into two longitudinal sections that have four layers per endcap and are made of 32 identical wedge-shaped modules. The copper plates have an outer radius of 2.03 m and an inner radius of 0.475 m except in the region of the overlap with the FCAL where the inner radius becomes 0.372 m. Between these copper plates, there is a gap of 8.5 m which is filled with LAr to provide the active medium.

The FCAL contains two hadronic modules which are optimized for high absorption length. This is achieved by maximizing the amount of tungsten in the modules. These modules consist of two copper end-plates, each 2.35 cm thick, which are spanned by electrode structures. Table 3.2 shows the parameters for the three FCAL modules. Signals are read out from the sides of the two hadronic modules of the FCAL further from the interaction point. This arrangement keeps the cables and connectors away from the region of maximum radiation damage. The FCAL has a total depth of 9.94 λ_o.

	FCAL1	FCAL2	FCAL3
Function	Electromagnetic	Hadronic	Hadronic
Mass of module (kg)	2119	3826	3695
Main absorber material	Copper	Tungsten	Tungsten
LAr gap width (mm)	0.269	0.376	0.508
Radiation length (X_o)	27.6	91.3	89.2
Absorption length (λ_o)	2.66	3.68	3.60
Number of electrodes	12260	10200	8224
Number of readout channels	1080	500	254

Table 3.2. Table of parameters for the three FCAL modules [35].

3.2.3.3. Electronics Calibration

As a particle passes through the detector, a charge is generated and is translated into a voltage "pulse" after passing through a set of electronic devices at a preamplification stage. A scheme of the calorimeter is shown in Figure 3.10 (left). The calibration of electronics is crucial to take into consideration the modification that the signal goes through prior to digitization. The ramp runs allow calibration of this chain by injecting a known charge prior to the preamps by Digital-to-analog converter (DAC) [37].

The ratio of the Analog to Digital Conversion (ADC) counts to (DAC) values of the readout and the input signals can be exploited for calibration purposes. They are measured regularly by the electronic calibration system. The ADC to DAC ratio is expected to be linear for a wide range of input DAC values, but to be more consistent with real data it is approximated by a second-order polynomial. Each of the electronic channels in the endcap has its own value that varies from run to run. This variation is sometimes only a minor fluctuation, but in other cases the value can change significantly. Channels that exhibit the latter behavior are referred to as unstable for the purposes of this study. The energy for a particle deposited in the LAr Calorimeter is described by the following equation [37]:

$$E = F_{DAC\rightarrow\mu A}\, F_{\mu A\rightarrow MeV}\, \frac{M_{phys}}{M_{cali}} \sum_{j=1,2} R_j [ADC_{peak}]^j \tag{3.3}$$

where the factors $F_{DAC\rightarrow\mu A}$ and $F_{\mu A\rightarrow MeV}$ are used in converting the DAC into MeV, and the factor $\frac{M_{phys}}{M_{cali}}$ corrects the ramp factors for the difference between the calibration and physics signal heights. The physics signal is triangular in shape as a function of time as shown in Figure 3.10. The integral of the signal is proportional to the energy deposition. The LHC will have a bunch crossing every 25 ns, but LAr calorimeters have an electron drift time of 400 ns for the electromagnetic calorimeter and 60 ns for FCAL (smaller gap size). The drift time is too long and leads to overlap of several signals, so the height of the signal changes as mentioned above. The factor ADC_{peak} is the peak of the shaped ionization signal computed by optimal filtering, and the factors R_j are the second order electronic ramps converting the ADC to DAC.

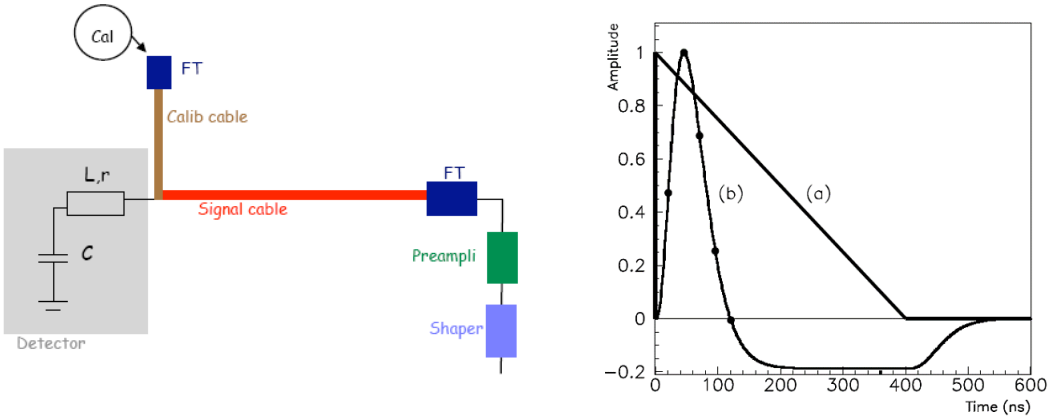

Figure 3.10. Electrical scheme of the calorimeter. a) Form of the ionization signal b) Form of the shaped ionization signal (left).

The correlation of ADC count to DAC value allows evaluation of slopes which are used directly in calculating the energy. The knowledge of how these slopes change between runs is essential for more accurate physics results. A comparison between these slopes for each

channel within a run to that of a reference run is desired. Therefore, each channel has had assigned a diagnostic ratio defined to be $\frac{Slope_{run\ channel}}{Slope_{reference\ channel}}$ [37].

I worked with two other students to analyze these parameters for each channel for barrel and endcap in many runs during the commissioning period in summer of 2007 [38]. There are two histograms for each Feed-Through (FT), a conductor connecting two circuits on opposite sides of a circuit board, and slot; these can be used to visually identify unstable channels as shown in Figure 3.11, and show how widely slopes vary within a run. One example problem is the fast shapers which can be a source of ramp instability. The problem appears in a group of four consecutive channels with a higher slope as shown in Figure 3.12 with decreasing readout wave parameters (amplitude and time of peak), which affects slope values. This is caused by changes of electronic parameters of a shaper on the electronic readout motherboard. One of the features of the fast-shaper problem is that it appears in new channels that have previously not shown unusual behavior. We reported the problems seen to the LAr Commissioning group. In general, the ramp coefficients show good stability from run to run on the level of 2-3 per mil. The slopes for all the channels in a given run are shown in Figure 3.13; they are fitted to a Gaussian distribution.

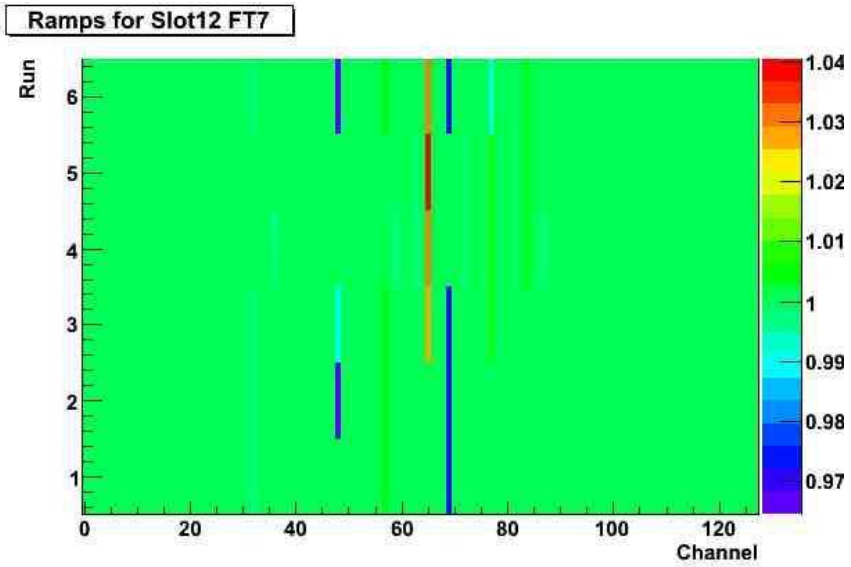

Figure 3.11. Some of unstable channels in slot 12 Feed-Through 7.

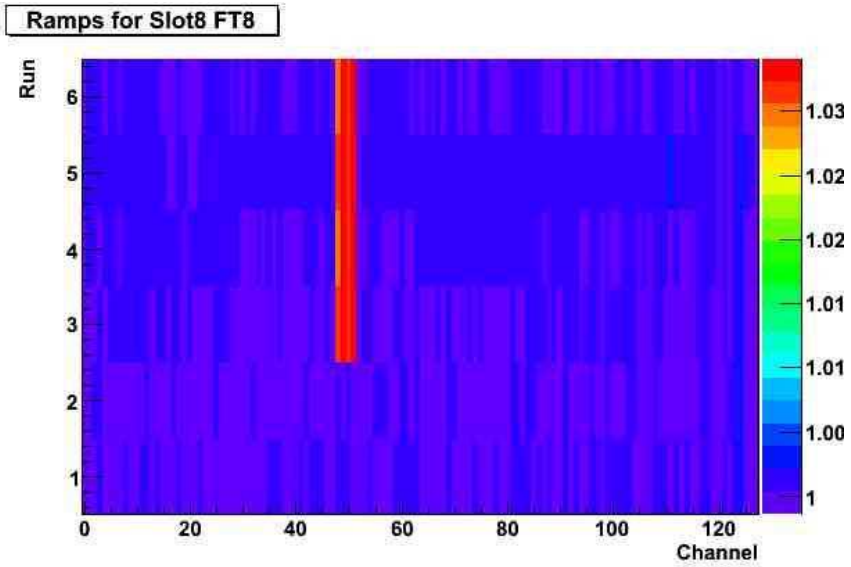

Figure 3.12. Fast shaper that is unstable in a given run. A fast shaper is a group of four consecutive channels that exhibit a ramp value that is lower than expected.

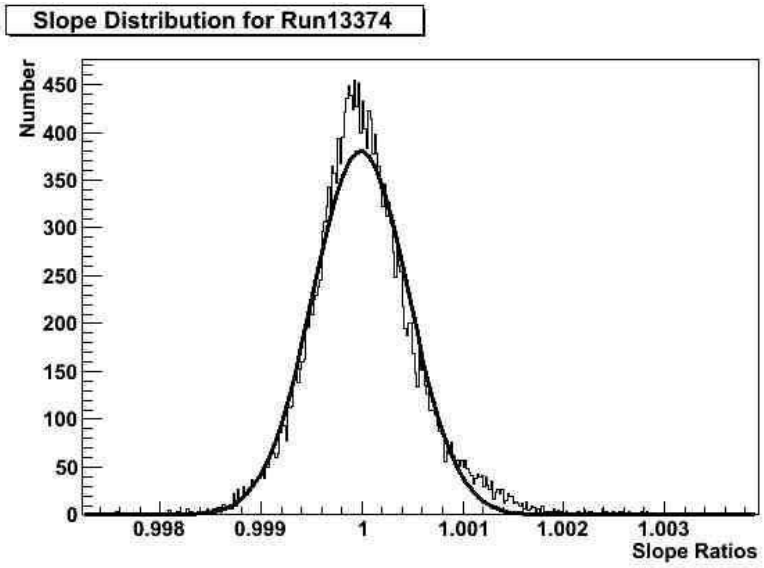

Figure 3.13. A histogram of slopes for all channels in run 13374. A Gaussian has been fit to the histogram.

3.2.4. Muon Spectrometer

The outer part of the ATLAS detector is the muon spectrometer. The general layout of the ATLAS muon spectrometer is shown in Figure 3.14. The momentum measurement is based on the magnetic deflection of the muon tracks in toroid magnets. In the η range of $|\eta| < 1.4$ the magnetic bending is provided by the large barrel toroid while in the region $1.6 < |\eta| < 2.7$, the bending is provided by two smaller endcap magnets inserted into both ends of the barrel toroid. Over the transition range, $1.4 < |\eta| < 1.6$, the magnetic bending is provided by a combination of barrel and endcap fields.

The muon chambers consist of three layers in the barrel region, called "stations", and stations in the endcap wheels. Muons are required to leave hits in all three muon stations. In the barrel, three layers at radii 5, 7.5 and 10 m cover the pseudorapidity range $|\eta| < 1$. The endcap chambers ($1 < |\eta| < 2.7$) are arranged in four disks at 7, 10, 14, and 23 m from the interaction point. There is a crack at $|\eta| = 0$ for cables and services. The track measurements are provided by the Monitored Drift Tubes (MDT). The

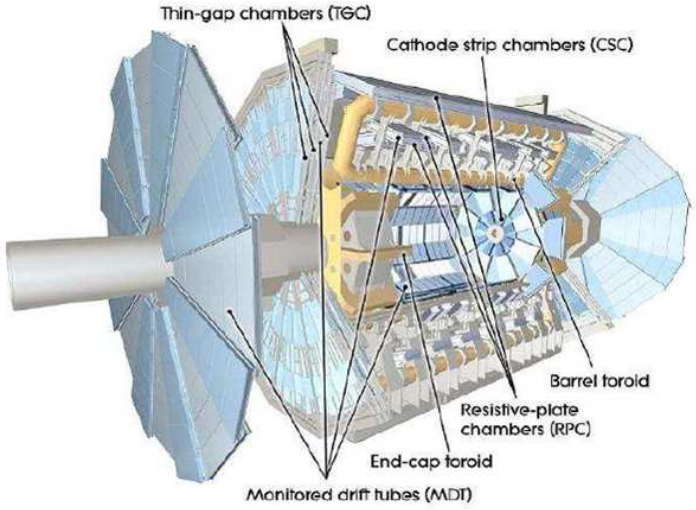

Figure 3.14. The ATLAS Muon System.

MDT covers a region $|\eta| < 2.7$ except in the innermost endcap layer where its coverage is limited to $|\eta| < 2$. The MDT consists of three to eight layers of drift tubes filled with a gas mixture (93% Ar and 7% CO_2) operating at an absolute pressure of 3 bar. The Cathode Strip Chambers (CSC) are used in the forward region ($2 < |\eta| < 2.7$) in the innermost tracking layer due to their higher rate capability and time resolution. The CSC is a multi-wire proportional chamber with both cathodes segmented. An important criterion of the muon system is the ability to trigger on the muon tracks. In the pseudorapidity range of $|\eta| < 1.05$, the triggering is made possible by Resistive Plate Chambers (RPC). In the endcap $1.05 < |\eta| < 2.4$, Thin Gap Chambers (TGC) provide the triggering. The interpolation between the charges induced on the neighboring cathode strips provide the position of the track.

3.2.5. Triggering

The designed bunch crossing rate at the LHC is 40 MHz with a bunch spacing of 25 ns. The huge amount of data is a challenge for processing and storage. Therefore,

a need for an efficient trigger system is crucial. The ATLAS trigger must reduce the data-taking to 200 Hz which is a rate that can be stored. While the background rejection is important, a high and unbiased efficiency for signals is a necessity. The ATLAS trigger and data acquisition system has three levels of event selections [35] [36]. The ATLAS trigger system is shown in Figure 3.15, and the expected event rates for several physics processes at the LHC design luminosity with trigger information are shown in Figure 3.16.

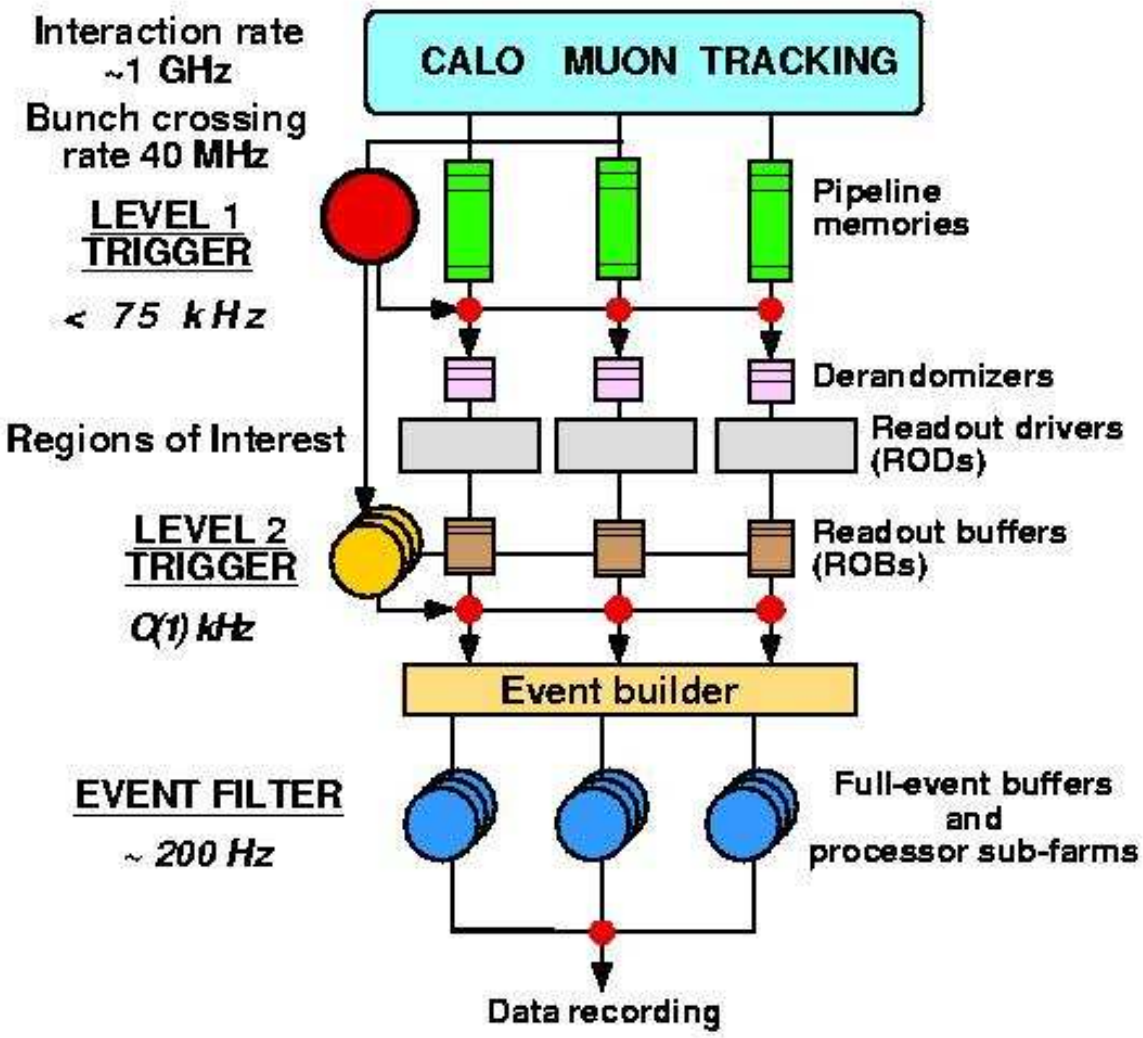

Figure 3.15. The ATLAS trigger system.

3.2.5.1. Level 1 trigger

The Level 1 (L1) is a hardware based trigger. The event selection is based on information from the calorimeters and the muon detector. The L1 trigger decision is based on energy thresholds of electrons/photons, muons, jets, hadronic τ-decays and large missing energy [39].

The L1 receives data at the full LHC bunch crossing rate of 40 MHz and is required to make a decision within 25 μs to reduce the output rate to 100 kHz. The information from different object types is gathered via the Central Trigger Processor (CTP)[40]. The L1 Calorimeter Trigger (L1Calo) makes use of the Tower Builder Board (TBB) for the EM calorimeter. It collects the analog signals, sums them and builds a trigger tower. The L1Calo's purpose is to identify events with high transverse energy, large missing energy, and high transverse-momentum jets. Similarly, the boards at the HEC and FCAL build the towers without the summation.

The L1Calo algorithms use transverse-energy values measured in trigger towers of granularity 0.1×0.1 in $\eta \times \phi$ from the EM and hadronic calorimeters. The analog signal is digitized by a pre-processor and the events from different bunch crossings are separated via a digital filter. These digitized data get transferred in parallel to the Cluster Processor (CP) and Jet/Energy-sum Processor (JEP). The role of the CP is to identify electron, photon and τ candidates with an E_T beyond a certain threshold that is specified in the trigger. A certain isolation criterion may be required. The JEP identifies jets and missing transverse energy using 0.2×0.2 sums in $\eta \times \phi$.

In the case that the event gets accepted by the L1Calo, the stored data are read out to the Data Acquisition (DAQ) system. It takes approximately 1.5 μs after the bunch crossing for the L1Calo information to reach the CTP. All the event information that passes the L1Calo trigger will be sent to the L2 trigger.

The L1 muon trigger consists of two trigger chambers [41]. In the barrel, the muon trigger is based on the Resistive Plate Chambers (RPC) [42]. The Thin Gap Chambers (TGCs) [41] provide the triggering on the endcap.

The RPC and TGC are gaseous ionization chambers with an electric field of 4.5 kV/mm. In the barrel, three layers of RPC's are located on both sides of the middle MDT layer and inside the outer MDT station. Similarly, three TGP layers are positioned near the middle of MDT station. The L1 muon trigger relies on information from the layers of the muon trigger chambers to identify muon candidates. The decision should be made in 2.1 μs.

The CTP makes the final decision after it gets the information from both calorimeters and muon triggers. This information will be compared with a table of trigger conditions (up to 256) and decides if a particular trigger passes.

3.2.5.2. Level 2 Trigger

An event passing the L1 trigger is an input to Level 2 (L2). The events selected by the L1 trigger system are stored in 1574 Readout Buffers (ROB's). The L2 is a software based algorithm. The selection is based on regions-of-interest (ROI) identified at L1. The ROI is an $\eta \times \phi$ region near an interesting object identified by L1, such as a high p_T electron. An L2 supervisor (L2SV) selects which ROB should be read and which L2 trigger processing unit should be used to analyze it. The selected ROB gets unpacked and the particles in it are fully reconstructed. The L2 trigger applies normal reconstruction procedures to part of the event only. The L2 trigger reduces the event rate from 100 kHz to 2.5 kHz with a decision time of 40 ms.

3.2.5.3. Event Filter

The final step in the online event selection is the Event Filter (EF) which is also a software trigger. If the event passes the L2 trigger, it gets transferred to an event-building node known as Sub-Farm Input (SFI). Otherwise, L2 clears all ROB's. Based on information collected from the ROB's, the SFI reconstructs the event completely. The selected event is sent to the (EF) for further analysis. It makes use of a farm of processors that consists of 1800 dual quad-core CPUs. The EF receives the events accepted by the L2 trigger at a rate of 2.5 kHz and must provide more rejection to reduce the rate to 200 Hz. The EF has a decision time of 1 s. Each L2 triggered object is used as a seed for EF algorithms which are the same algorithms as the off-line reconstruction. If the event passes the EF, it is classified to a predetermined set of data streams and gets sent to the output nodes and is stored. Moreover, L2 and EF also run monitoring algorithms to help ensure good quality data is taken.

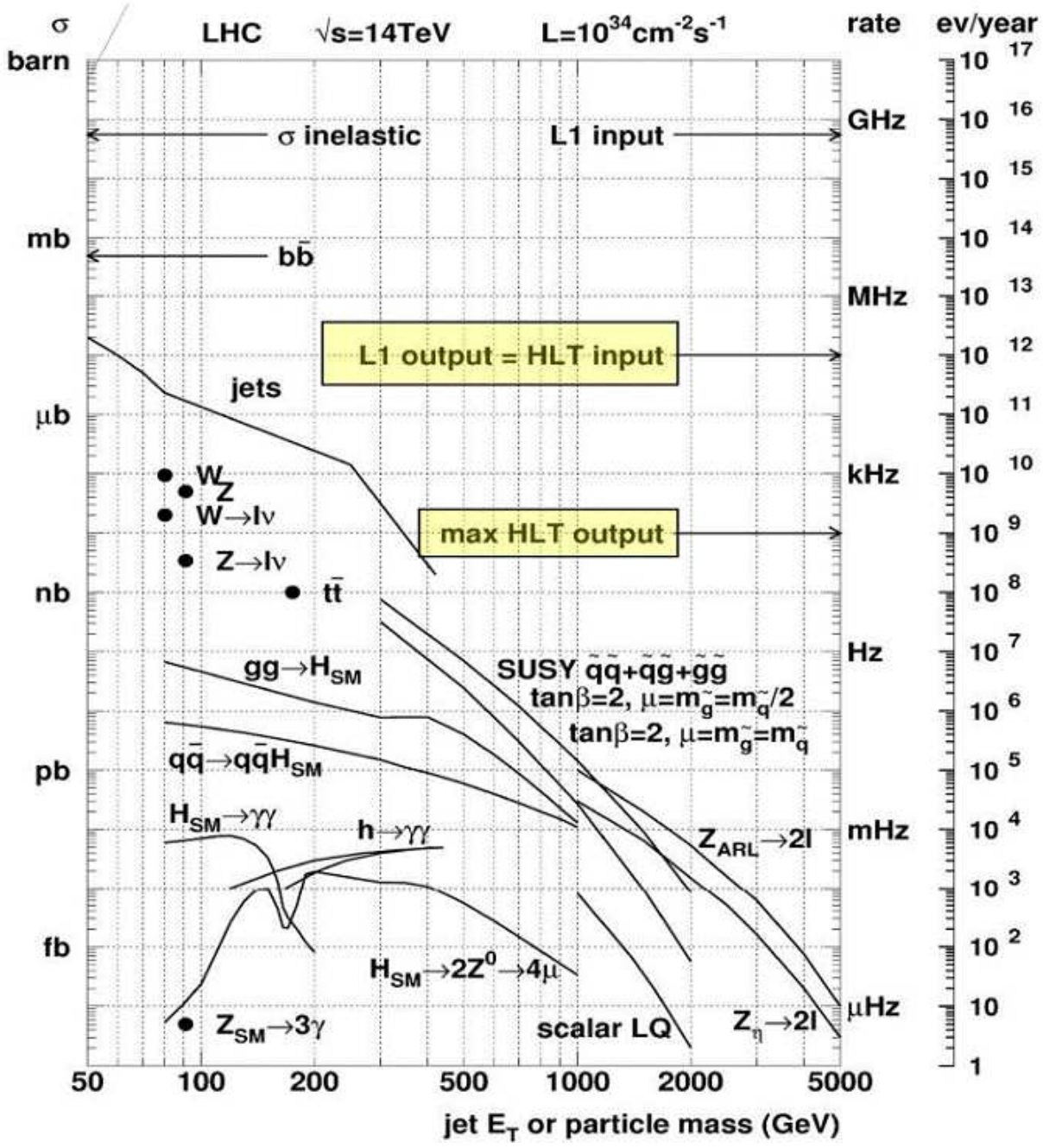

Figure 3.16. Expected event rates for several physics processes at the LHC design luminosity with trigger information.

Chapter 4

SAMPLES AND MODELING

Having described the detector, we now describe the underlying modeling of the data. This chapter describes the event generators used to create Monte Carlo events for this analysis, the detector simulation, and some aspects of triggering. I finish with my estimate of the efficiency for selected trigger schemes for the ZZ and Higgs boson signal events of this thesis.

4.1. Monte Carlo Simulation

The theoretical modeling of the outcome of high-energy particle collisions is crucial to interpreting the measurement of fundamental properties of particles, or to infer the existence of new physics. A variety of complex signals will be produced via the pp collisions at the LHC. Monte Carlo methods are a class of computational algorithms that make use of random numbers to mimic the properties of random processes. These are appropriate to modeling particle physics processes because of their quantum mechanical nature. Event generators are Monte Carlo methods which use theoretical models to describe the behavior of interactions between fundamental particles. The particle generators randomly generate event kinematic parameters weighted by known or expected distributions. This is done for a given center of mass energy of a particle collision of a given type, a pp collision for example.

4.1.1. Event Generators

In high-energy collisions, the perturbation method is applicable only to the fundamental constituents of the theory such as quarks or leptons. Therefore, the first step in the simulation of a pp collision is the generation of a parton-level event. The event-generator

programs are based on a fundamental physical concept, factorization, which is the ability to isolate separate independent phases of the overall collision. As a result, a pp-collision process can be factorized into a parton collision weighted by parton-distribution functions $F_i(x)$. These functions give the momentum fraction x carried by parton i relative to the parent hadron. At this level, the interaction is limited to the proton constituents, quarks and gluons. However, the parton-level event will evolve to a final state after a series of fragmentation showers and decays. The particles that will be observed at the detector level are known as "final-state particles".

The LHC events will contain huge numbers of hadrons, and a large fraction of these events will have many hard jets. Given the complexity of LHC events, two types of generators are used. The first type is the matrix element (ME) generator; examples of these ME generators are JIMMY [43] and MC@NLO [44]. Unfortunately, these generators are not suitable for describing the conversion of hard partons into jets. Thus, one uses a second type of generator, showering Monte Carlo generators. PYTHIA [45] and HERWIG [46] are classified as showering generators. PYTHIA is a program that can simulate two incoming colliding particles at a given center of mass energy collision. It is able to simulate the multi-particle production which is a characteristic result of such a collision. Colored objects produced in these collisions undergo hadronization and produce colorless objects. The fragmentation in PYTHIA is modeled via the Lund string model discussed in Chapter 2. The Higgs events in this dissertation have been generated by PYTHIA for both parton level and showering.

To include the NLO corrections, the MC@NLO generator is used to incorporate the NLO QCD [47] matrix elements. HERWIG is used to perform soft QCD modeling. It uses a cluster model, discussed in Chapter 2, for jet fragmentation based on non-perturbative gluon splitting. Moreover, it uses a cluster model for soft and underlying hadronic events. The ZZ signal events in this thesis have been produced via MC@NLO and HERWIG.

The JIMMY generator is designed to generate multiple-parton scattering events in hadron-hadron, photon-photon or photon-hadron events. It is an ME generator and the

showering is usually provided via HERWIG.

Finally, the AcerMC [48] event generator is dedicated to generation of the SM background processes at the LHC, such as the $Zb\bar{b}$ and Zb. The hard process events can be completed by the initial and final state radiation, fragmentation and decays, simulated with either PYTHIA or HERWIG. The matrix elements have been coded by the MadGraph [49] and HELAS [50] packages.

4.1.2. Detector Simulation

The produced particles in their final states interact with the detector. This interaction leads to the deposition of particle energy which is converted to an analog signal which finally is converted to a digital signal. The program that simulates the passage of a particle through matter is known as GEANT (GEometry ANd Tracking) [53]. For a given layout of a detector, the program can simulate how this layout will affect the progression of particles in an experiment. This can be in terms of the signal generated in sub-detectors, energy loss in different parts of the detector including the dead channels and the support structure. Therefore, one can obtain the detector response to a particle passing through it and can approximate how a real detector would respond. The produced data is formatted to that of an event in the real experiment. As with the event generator, the program relies on Monte Carlo methods.

4.2. Signal and Background Samples

In the four lepton channels that we consider for this analysis, we face a substantial amount of background. The physics background consists of all the SM processes with a three-lepton signature: $Zb\bar{b}$, Zb, $t\bar{t}$ and WZ. In the case of the Higgs analysis, Z boson pair are the main background. In this analysis, we used simulated data for these processes using Athena release 13.0.30. We summarize the samples that we used in this analysis in Table 4.1. The samples used in this thesis were generated via different generators depending on the properties of each process.

1. Higgs: The Higgs samples ($m_H = 150$ GeV, $m_H = 180$ GeV, $m_H = 200$ GeV, and $m_H = 300$ GeV) were generated exclusively via PYTHIA. The parton distribution function used is CTEQ6M. The cross sections were calculated at (LO) taking into account both gluon-gluon and weak boson fusion (WBF) diagrams. The (NLO) effects were considered by scaling the PYTHIA cross section [51]. During generation, a four lepton filter was applied with $p_T > 5$ GeV within $|\eta| < 2.7$ on the four leptons.

2. $ZZ \rightarrow 4l$: The ZZ's are modeled by the MC@NLO generator which incorporates the NLO QCD matrix elements into the parton shower by interfacing to the HERWIG program. We used the CTEQ6M parton distribution function. A branching ratio of 0.0336 for $Z \rightarrow \ell^+\ell^-$ was used. The next to next to leading order (NNLO) contributions were due to the gluon-gluon fusion [26, 27]. Their contributions were estimated to be 20%.

3. $Zb\bar{b} \rightarrow 3\ell$ and $Zb \rightarrow 3\ell$ were generated by AcerMC. The parton distribution function used is CTEQ6L and the QCD scales ($\mu_R = \mu_F = m_Z$, massive b-quark). The showering was done via PYTHIA. The $Z \rightarrow \ell^+\ell^-$, ($l = e,\ \mu$) decay was forced at the generator level as well as $|\eta| < 2.7$ on leptons. The full Z/γ^* interference was taken into consideration. Moreover, a resonance cut of $M_Z > 30$ GeV was applied. To account for higher order corrections, a k-factor of 1.42 was used.

4. $WZ \rightarrow 3\ell + \nu$ generated by JIMMY, and the parton distribution function used is CTEQ6M. The requirements imposed at the generation level were $p_T > 5$ GeV and $|\eta| < 2.8$ on the three leptons.

5. $t\bar{t} \rightarrow 4\ell$ generated by MC@NLO, and the parton distribution function used is CTEQ6M. The requirements imposed at the generation level were $p_T > 5$ GeV, $|\eta| < 2.7$ for the leptons, and the b quarks were forced to decay semi-leptonically.

Signature	Number of events	Cross section fb
Higgs ($M_H = 180GeV$)	17000	5.38
Higgs ($M_H = 200GeV$)	48000	20.53
Higgs ($M_H = 300GeV$)	10000	13.32
ZZ	20000	66.8
$Zb\bar{b}$	36500	12663
Zb	20000	14000
$t\bar{t}$	400000	6064
WZ	15000	807

Table 4.1. Monte carlo samples that were used in the analyses presented in this thesis. The cross sections are shown combined with the branching ratios, at 14 TeV center of mass energy, are evaluated at next to leading order [51, 52].

4.3. Trigger and Data Acquisition

The data-taking process requires that only events that have passed at least one of the triggers are stored. Therefore, it is crucial for a signal event to pass at least one of the triggers for analysis. Since the final states of the signal include electrons and muons, I will discuss briefly the electron and muon triggers.

The full-granularity information from the EM and hadronic calorimeters is used to select electromagnetic clusters and thus identify electron trigger objects. The L2 electron selection uses information from the TRT and precision tracker, SCT and pixel system. The first step of the selection criteria is based on the cluster shower shapes and the E_T deposition in the calorimeters. The second step is consists of selecting clusters likely to be due to an isolated electron. The electron hypothesis is accepted if a matching track is confirmed in the TRT and precision tracker within the ROI.

The muon trigger (L2) runs on full granularity data within the ROI defined by L1. After pattern recognition driven by the trigger hits which selects MDT regions crossed by the muon track, a trajectory fit is performed using MDT drift time precision measurements. Moreover, isolation is applied by examining the energy depositions in the EM and

hadronic calorimeters. The possibility of using the Tile calorimeter can provide robustness to the muon trigger and enhance the low p_T region. The search starts with the outermost calorimeter layer, contains the cleanest signals, and once the deposited energy is compatible with a muon, the energy deposition in the neighboring cells for the internal layers are checked. If the muon compatible cells are found following an η-projective pattern in all three Tile calorimeter layers, the object is tagged as a muon. The EF processing starts by reconstructing tracks in the muon spectrometer around the muon found by L2 and it is done in three steps. The first step reconstructs tracks in the muon spectrometer starting with a search for regions of activity within the detector, and subsequently performing pattern recognition and full track fitting. The second step extrapolates muon tracks to their production point. Finally, the information from the first two steps is combined with the reconstructed tracks from the inner detector.

We used triggers from the trigger menu available in release 13 [52].

1. **EF_e10**: A single electron trigger at L1, L2, and EF. The requirements are: an electromagnetic cluster with $p_T > 5$ GeV at L1, an electron with $p_T > 10$ GeV at L2, and EF. No isolation is required.

2. **EF_mu6**: Single muon trigger. The requirements are single muon with $p_T > 6$ GeV at L1, L2, and EF. No isolation is required.

4.4. Estimation of Trigger Efficiencies for Signal

The relative trigger efficiencies were evaluated as the ratio of the number of events for which a given trigger passes, $N^{trigger}$, to the number of events with three reconstructed leptons $N^{3leptons}$ with $p_T > 10$ GeV as shown in Equation 4.1.

$$\epsilon_{trigger} = \frac{N^{trigger}}{N^{3leptons}} \tag{4.1}$$

The final trigger efficiencies are summarized in Tables 4.2 and 4.3. In the case of an efficiency from a single trigger less than 100%, we can use two in such a way that either

one of them should be triggered.

Trigger item	ZZ	H (180)	H (200)	H (300)
EF_e10	0.997 ± 0.001	0.998 ± 0.001	0.998± 0.001	0.997± 0.001

Table 4.2. Trigger efficiencies for the $3e$ channel. The errors on the trigger efficiencies are binomial.

Trigger item	ZZ	H (180)	H (200)	H (300)
EF_e10	0.963 ± 0.002	0.977 ± 0.002	0.975± 0.002	0.978± 0.002
EF_mu6	0.954 ± 0.003	0.967 ± 0.003	0.971± 0.002	0.963± 0.003

Table 4.3. Trigger efficiencies for the $2\mu 1e$ channel. The errors on the trigger efficiencies are binomial.

Chapter 5

PARTICLE DETECTION AND IDENTIFICATION

After each pp collision, many particles will be created and their interaction with the detector will be converted to a signal. The process by which these detector signals are converted into particle energy, momenta, or missing energy for data analysis is known as reconstruction.

5.1. Track Reconstruction

5.1.1. Single Track Reconstruction

The track reconstruction is very important for electron and muon identification, especially at low p_T. The inner detector provides tracking information for charged particle tracks with $p_T > 0.5$ GeV and $|\eta| < 2.5$ [54]. The track leaves hits in the pixel and the SCT detectors; a track reconstruction algorithm then uses track extrapolation [55] and track fitting. In the inner detector, the track reconstruction can be summarized into three steps.

1. The raw data from pixel and SCT detectors are converted into clusters. These clusters are transformed into space-points, which are points where a track crosses the detector. This process uses a combination of a hit in a pixel detector or two hits from opposite sides of the SCT layer for a space point.

2. The second step is track finding. The combination of space-points in the three pixel layers and the first SCT layer form a track seed. These seeds are extrapolated throughout the SCT to make a track candidate. To ensure the quality of the tracks and reject the fake ones, many quality cuts are required. These cuts are the total numbers of space-points and the number of holes per track. A hole occurs when a track does not leave a cluster when it crosses the detector.

3. Finally, an algorithm which is dedicated to reconstructing primary vertices is used.

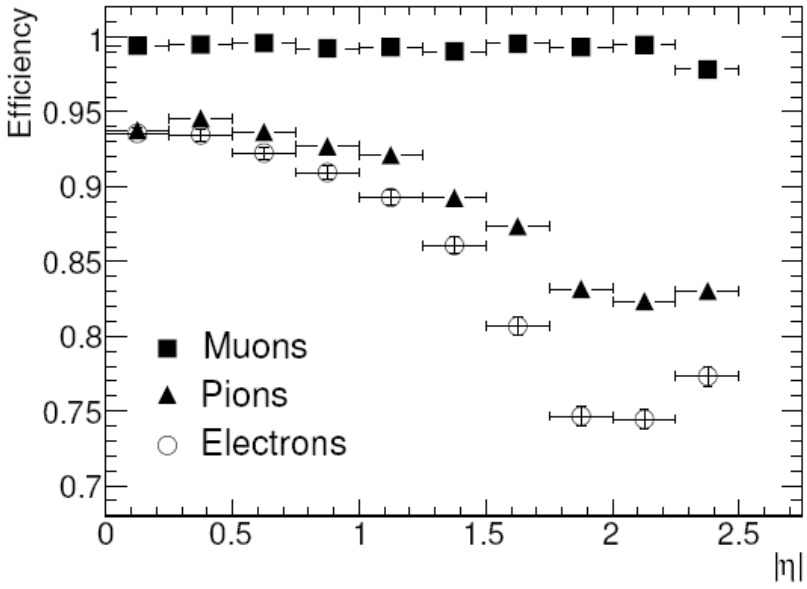

Figure 5.1. Track reconstruction efficiencies as a function of $|\eta|$ for muons, pions and electrons with $p_T = 5$ GeV. The inefficiencies for pions and electrons reflect the increase in the amount of material in the inner detector with increasing $|\eta|$.

The standard quality cuts on reconstructed tracks require that they have at least seven precision hits in either pixels or SCT. The transverse and longitudinal impact parameters at the perigee must fulfill $|d_o| < 2$ mm and $|z_o - z_{pv}| \sin\theta < 10$ mm respectively, where z_{pv} is the longitudinal location of the primary vertex and d_o is the transverse impact parameter. Furthermore, only tracks with $p_T > 1$ GeV are considered. The track reconstruction efficiencies for electrons, muons, and pions are shown in Figure 5.1. The efficiency of finding the primary vertices is very high at high p_T. The resolution in position of the primary vertex is around 12 μm in each transverse direction and 50 μm along the beam

direction z. However, the presence of additional vertices makes the track finding less trivial. In that case, the probability that a wrong vertex can be picked up as a primary vertex is about 10 % [57].

Leptons from $t\bar{t}$, $Zb\bar{b}$, and Zb are most likely to originate from displaced vertices. This is due to the relatively long lifetime of the b quark. The tracks from b-hadron decay products are likely to have large impact parameters which can be distinguished from tracks stemming from the primary vertex. In order to select only prompt electrons originating from the Z's, I used the transverse-impact parameter significance [51]. It is defined as the ratio d_o/σ_{d_o} of the transverse-impact parameter, also know as distance of closest approach (DCA), to its measured error. Bremsstrahlung is greater for electrons and smears the impact-parameter distribution. This reduces the discriminating power of this cut with respect to muons as shown in Figure 5.2. The impact parameter is evaluated with respect to the event vertex fitted using a set of tracks reconstructed in the inner detector. Therefore, one can remove the effect of the spread of the vertex position which is $\sigma_{xy} = 15$ μm in the transverse axes x and y, and $\sigma_z = 5.6$ cm along the beam axis.

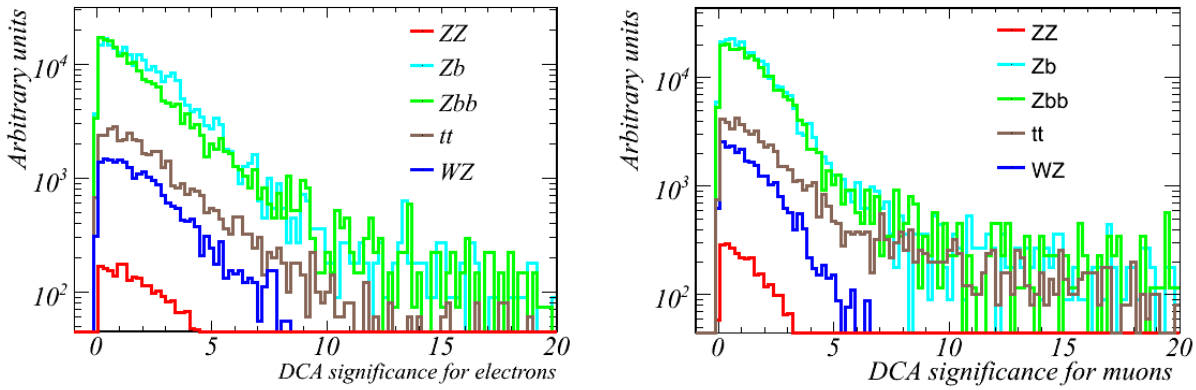

Figure 5.2. Transverse-impact parameter significance for electrons in signal and background events (left). Transverse-impact parameter significance for muons in signal and background events (right).

5.1.2. Secondary Vertex Reconstruction

To further increase the discrimination against the b-jets, one can reconstruct the secondary b-hadron decay vertices inside the jet. The b-tagging algorithm is based on variables which show significant differences in behavior between a b jet and a light-quark jet. The search starts with building all two-track pairs that form a good vertex with tracks far away from the primary vertex. All the remaining two-track vertices are combined into a single inclusive vertex using an iterative procedure to remove the worst combination until the χ^2 of the vertex fit is good. Three properties of the vertex are used: the invariant mass of all tracks associated with the vertex, the ratio of the sum of the energies of the tracks of the vertex to the sum of all energies of all tracks in the jet, and the number of two track vertices. These properties are shown in Figure 5.3. The secondary vertex tagging SV relies on these three properties in many different forms. SV2 uses a 3D-histogram of the three properties [56]. Moreover, a likelihood ratio method is used in the secondary vertex tagging. The measured values S_i of a discriminating variable are compared to pre-defined smoothed and normalized distributions for both the b- and light-quark jet hypotheses, $b(S_i)$ and $u(S_i)$. The ratio of the probabilities $b(S_i)/u(S_i)$ defines the track or vertex weight which can be combined into a jet weight W_{Jet} as the sum of the logarithms of the N_T individual track weight W_i as shown in Equation 5.1:

$$W_{Jet} = \sum_{i=1}^{N_T} \ln W_i = \sum_{i=1}^{N_T} \ln \frac{b(S_i)}{u(S_i)} \tag{5.1}$$

5.2. Calorimeter Reconstruction

The energy deposited in the calorimeter undergoes a calibration process [59]. The first step of the calibration is the "electronic calibration", as discussed in Chapter 3, where the raw signal data extracted from each cell (ADC counts) is converted to a deposited energy [60]. In the second step, the energies deposited in the cells of each layer of a cluster are summed. The EM calorimeter consists of four layers as described in Chapter 3. Therefore, the total energy of the cluster is the sum of the energies of the four layers as shown in the

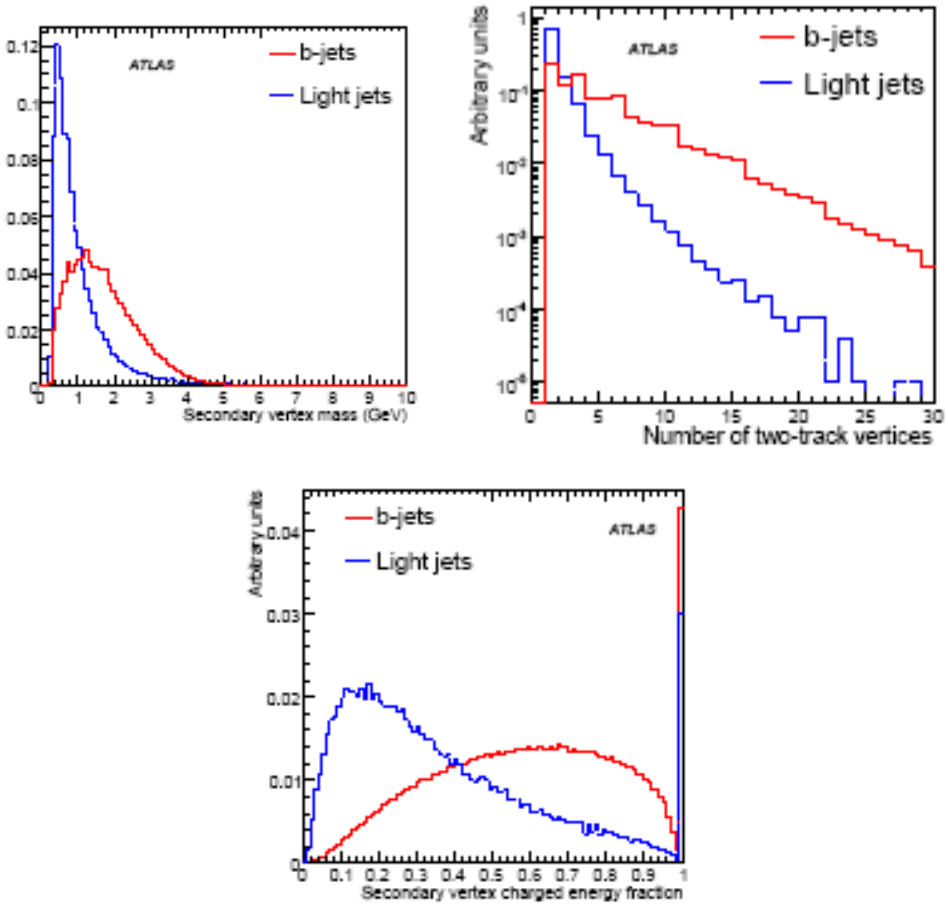

Figure 5.3. Secondary vertex variables: invariant mass of all the tracks in the vertex (upper left), number of two-track vertices (upper right) for b-jets and light-quark jets, and energy fraction vertex/jet (bottom).

following equation.

$$E_{reco} = A(B + W_{ps}E_{ps} + E_1 + E_2 + W_3E_3), \tag{5.2}$$

where E_{ps} is the energy in the presampler while $E_{1,2,3}$ are the energies in the three layers of the calorimeter. A is an overall scale factor, the term W_{ps} is for correction of the energy losses upstream of the presampler, W_3 corresponds to the longitudinal leakage corrections, and the parameters, A, B, W_{ps}, and W_3, are η dependent. They are calculated by a χ^2 minimization of $\frac{(E_{true}-E_{reco})^2}{\sigma(E_{true})^2}$ using Monte Carlo single particle samples. $\sigma(E_{true})$ is a parametrization of the expected energy resolution.

5.2.1. Electron Reconstruction

The standard electron reconstruction algorithm is based on a sliding window algorithm. The first step in electron identification is a search for an electromagnetic tower seed with a certain energy threshold. The window size is 5×5 calorimeter cells in the middle layer in η and ϕ. A pre-cluster is formed for this window if the threshold energy in that window is greater than 3 GeV. The position of the pre-cluster is computed using a window around the current position that has a smaller size (3×3) than the initial sliding-window. Using a smaller window size for position computation is less sensitive to noise. The EM cluster filling consists of all cells that are located inside a rectangle centered on the seed position. The rectangular size is given in tower units $\Delta\eta \times \Delta\phi$. EM-cluster filling of different sizes such as 3×5, 3×7 or 5×5 are available. An extrapolated track to the EM calorimeter is required to match the cluster within a $\Delta\eta \times \Delta\phi$ window of 0.05×0.10. Moreover, the ratio of the energy of the cluster to the momentum of the track, E/p, is required to be lower than 10. Also, $|\eta| < 2.5$ is required. Improvements to electron identification using tracking information from the TRT were implemented into the electron reconstruction [32] which benefit all $ZZ \to 3e$ or $H \to ZZ^* \to 3e$ analyses.

Electron identification is based on many sets of cuts that can be applied independently. These cuts are optimized in up to seven bins in η and up to six in p_T. We define here

three reference sets of cuts: loose, medium, and tight. This improves the signal efficiency in a given analysis as well as lower potential background.

1. Loose cuts

   This set of cuts is based on calorimeter information only. Cuts are applied on hadronic leakage and on shower-shape variables, derived from the middle layer of the EM calorimeter only. The set of loose cuts provide an excellent electron identification efficiency, but a very low background rejection.

2. Medium cuts

   Cuts on the strips in the first layer of the EM calorimeter and on the tracking variables are added. The strip-based cuts are efficient in rejecting the $\pi^o \rightarrow \gamma\gamma$ decays as the energy deposits of the π^o residuals are often found to have two maxima. The showers are studied in a window $\Delta\eta \times \Delta\phi = 0.125 \times 0.2$ around the cell with the highest E_T to search for a second maximum. The variables used include the difference between the energy associated with the second maximum and the energy reconstructed in the strip with the minimal value, found between first and second maxima. It also includes other variables such as: the shower width over the strips covering 2.5 cells of the second layer (20 strips in the barrel), the shower width over three strips around the one with maximal energy deposit, and the fraction of energy deposited outside the shower cone of three central strips. The tracking variables consist of the number of hits in the pixel, the number of silicon hits, pixels and SCT, and the transverse impact parameter. The medium cuts increase the jet rejection by a factor of 3-4 with respect to the loose cuts, while reducing the identification efficiency by 10%.

3. Tight cuts

   All available electron identification tools are used in the tight cuts. It includes the cuts used in the medium set and extends to the number of vertexing-layer hits to reject electrons from γ conversion, the number of hits in the TRT, and the ratio of high threshold hits to the number of hits in the TRT to reject background from charged hadrons. Two different final selection cuts are available in the tight set, the

tight ($isol$) and tight (TRT) which are optimized differently for isolated and non isolated electrons. The tight ($isol$) cut requires an isolation cut on the cluster using ΔR cone of 0.2 to suppress fakes from jets. The tight (TRT) requires tighter cuts on the TRT information to suppress charged hadrons.

The electron identification efficiency for tight, medium, and loose electrons versus η and E_T is shown in Figure 5.4. In our analysis, we used a set of cuts between the medium and the tight electrons as we required transverse impact parameter and calorimeter isolation as explained in the next sections.

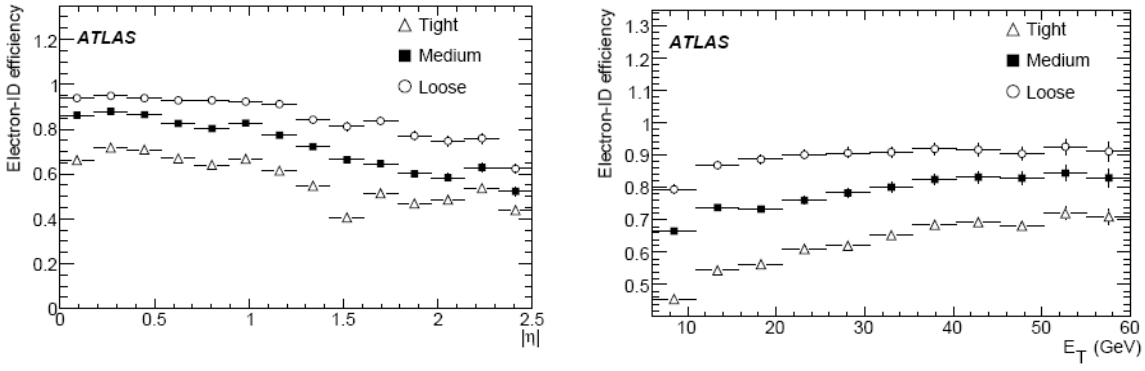

Figure 5.4. Electron identification efficiencies as a function of $|\eta|$ (left) and E_T (right) for electrons with $E_T > 5$ GeV from $H \rightarrow 4e$ decays.

The medium electron reconstruction efficiency is shown in Table 5.1 for three samples, ZZ and two Higgs mass points 150 GeV and 200 GeV. The $3e$ channel has around 50% efficiency.

Selection Efficiencies	ZZ	H (200 GeV)	H (150 GeV)
$3e$ (%)	48±0.7	54±0.4	52±0.6

Table 5.1. Reconstruction efficiencies for and $3e$ events in $ZZ \rightarrow 4e$ samples and $H \rightarrow 4e$ decays ($m_H = 150$ GeV) and ($m_H = 200$ GeV). The electrons are required to pass the medium cuts requirement with a $p_T > 5$ GeV. The shown errors are binomial.

5.2.2. Topological Clusters

The topological clusters are based on three dimensional reconstruction of the energy deposition in the calorimeters. The seed cell is required to have an energy $|E_{cell}| > 4\sigma_{cell}$, where σ_{cell} is the total noise which includes both electronic and noise pile up. The nearest neighbors around the seed are also collected independently of their own signal. The neighbor cell is considered a secondary seed if $|E_{cell} > 2\sigma_{cell}|$; its neighbors are also added to the cluster. Finally, all the cells contiguous to the seed with a threshold above 0 σ are added if no more secondary seed is found among the direct neighbors. This algorithm provides noise suppression.

5.2.3. Jet Reconstruction

Jet reconstruction is a clustering algorithm that can use calorimeter towers or topological clusters as input. It covers the region of $|\eta| < 4.9$. The towers are built from collecting cells into a regular grid of $\Delta\eta \times \Delta\phi = 0.1 \times 0.1$. The tower signal consists of a sum of all the cells of the tower or a corresponding fraction of the cell in the overlap area between the tower and the cell in $\Delta\eta$ and $\Delta\phi$. The jet finder does not use towers with negative signals which are due to the noise. The negative-signal towers are combined with nearby positive signals until the net signal is positive. Hence, the resulting towers get a valid physics four vector and will be used by the jet finder.

The jet clustering algorithm is a seeded fixed cone algorithm. The transverse energy of the seed should be higher than the threshold $E_T = 1$ GeV for all cone jets. The cone

size is $\Delta R = \sqrt{\Delta\eta^2 + \Delta\phi^2}$, with $\Delta R = 0.4$ for narrow jets and $\Delta R = 0.7$ for wide jets. The axis of the cone should correspond to the jet direction. Overlap between the cones is possible and they should be either merged or split via a "split-and-merge" step. In the case of overlap, the decision is based on the fraction f_{sm} in the shared towers for the p_T of the less energetic jet. If $f_{sm} > 0.5$, the two jets are considered as one jet and merged. Otherwise, they are considered as two separate jets and will be subjected to a splitting procedure.

The jet calibration is required as the jet algorithm provides jets at the electromagnetic scale. For that purpose, a cell-signal weighting function for each calorimeter cell that depends on the energy density is used in ATLAS. The calorimeter cells with four momentum $(E_i, \overrightarrow{p}_i)$ are re-summed with weighting functions w, and the new jet four momentum reads [57]

$$(E_{rec}, \overrightarrow{p}^{jet}_{rec}) = (\sum_{i}^{N_{cells}} w(\rho_i, \overrightarrow{X}_i)E_i, \sum_{i}^{N_{cells}} w(\rho_i, \overrightarrow{X}_i)\overrightarrow{p}_i) \tag{5.3}$$

The weighting functions w depend on the cell signal density, $\rho_i = E_i/V_i$, where V_i is the volume of the cell, and $\overrightarrow{X}_i$ is the cell location in the calorimeter. The detector effects are taken into consideration in the weighting functions. Moreover, the missing signals of low p_T particles are included. The energy loss due to inactive material is also implicitly included. Simulated QCD di-jet samples in the p_T range expected at the LHC are used in calculating these weighting functions. Figure 5.5 shows the final jet energy resolution for two cone sizes of the jet algorithms.

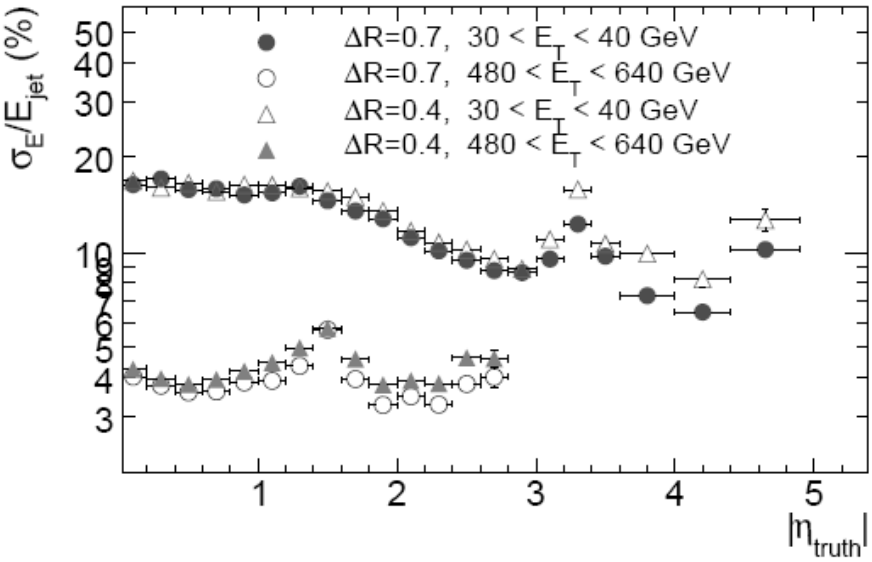

Figure 5.5. Jet energy resolution for QCD di-jets in two different E_T ranges, as a function of $|\eta|$ for the matched truth-particle jet. The results are shown for cone-tower jets with $\Delta R = 0.7$ and $\Delta R = 0.4$.

5.3. Muon Reconstruction

ATLAS can detect muons with momenta ranging from 3 GeV to 3 TeV. The muon reconstruction is based on three strategies. The first one is called "stand-alone" where the muon track reconstruction is based on the muon spectrometer only. The second one is a combination of a muon spectrometer track with the inner detector track. It is known as the "combined" strategy and it has the inner detector acceptance range $|\eta| < 2.5$. The third strategy is based on a combination of an inner detector track with a muon spectrometer segment.

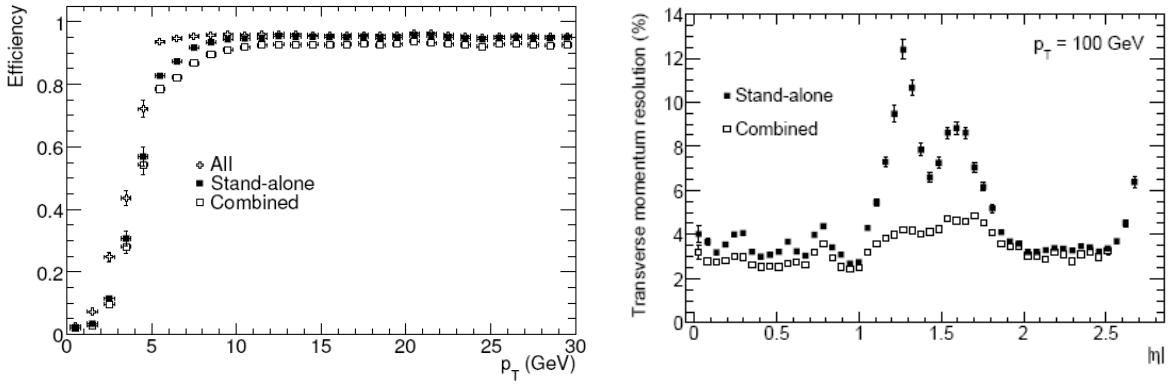

Figure 5.6. Efficiency of muon reconstruction as a function of p_T (left). The results are shown for "combined" reconstruction, and for the combination of these with the segment tags (left). Expected momentum resolution for a muon of $p_T = 100$ GeV.

A degradation in stand-alone momentum resolution in $(1.1 < |\eta| < 1.7)$ is due to the absence of the middle stations in the barrel/end-cap transition region (see Figure 5.6 (right)). The combined method is characterized by a flat p_T resolution with respect to $|\eta|$.

The muon reconstruction starts from processing the raw data from the MDT's and SCT's. If the signal is similar to what is expected from a muon, the corresponding line in the chamber is designated as a track segment. An extrapolation from segments in the middle stations to other regions is performed to build the full muon track.

The combined method improves the momentum resolution for tracks with momentum below 100 GeV. Furthermore, it will also suppress background from pion or kaon decays. The method used to combine the tracks from the muon spectrometer with tracks from the inner detector used in the analysis is known as "STACO". It is based on the statistical combination of two independent measurements; the track in the inner tracker and the track from the muon system. The pair of tracks corresponding to the full muon path is retained for the best combined χ^2.

The inner detector tracks are extrapolated to the inner muon stations. This method provides an improvement to the stand-alone muon reconstruction for three main reasons. The first reason is the fact that muons at low momenta < 6 GeV do not reach the middle and outer muon stations. The second reason has to do with the transition in the barrel end-cap region ($1.1 < |\eta| < 1.7$) where the middle stations are missing which leads to a drop in the efficiency in that region for the stand-alone reconstruction. In the regions of $\eta = 0$, the geometrical acceptance is reduced.

5.4. Lepton Isolation

A distinctive feature of the signal event from the background event is lepton isolation. The leptons in a signal event are isolated while in the background events at least one lepton is non-isolated. In the $t\bar{t}$, $Zb\bar{b}$, and Zb backgrounds, one lepton originates from a jet, generally from a semi-leptonic of b decay. In that case, the lepton can be produced some distance from the jet axis. Moreover, a jet can fake an electron in the calorimeter.

The environment of a lepton originating from a jet should contain some hadronic signature unlike a lepton from a signal event which is isolated. The transverse energy in a cone of a certain size around the direction of a given particle with the subtraction of the the transverse energy of the particle itself can be used to quantify isolation of leptons. For this analysis we used a cone size of ΔR =0.2, and calculate the E_T in the cone ("etcone"). I defined the isolation as the ratio of this energy to the transverse energy of the particle $\frac{etcone(\Delta R=0.2)}{E_T^{lepton}}$. The isolated lepton is characterized by a small value of the

isolation parameter as shown in Figure 5.7 which shows the isolation information for signal and background for electrons. In this analysis, I require this ratio to be less than 0.14 [58] for both electrons and muons.

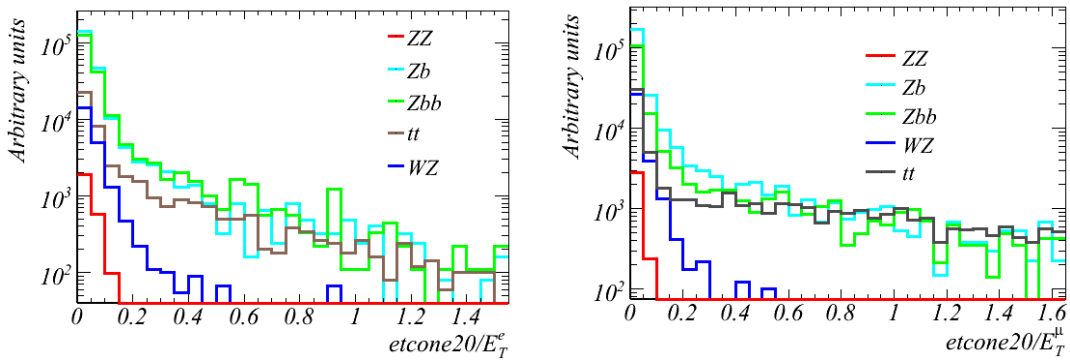

Figure 5.7. Isolation information for electrons (left) and for muons (right). where isolation is defined as $\frac{etcone(\Delta R{=}0.2)}{E_T^{lepton}}$

5.5. Missing Transverse Energy Reconstruction

The missing transverse energy, $\not\!\!E_T$, is a characteristic feature of the neutrino signature. The neutrino interacts only very weakly with matter, therefore, it escapes detection. One can find the $\not\!\!E_T$ in an event by using the momentum conservation principle in any physics process. Therefore, the net transverse momentum of outgoing particles should remain equal to the transverse momentum of incoming particles, which is equal to 0. However, the initial momentum of the colliding partons along the beam axis is not known so the amount of total missing energy cannot be determined in the longitudinal direction. One can deduce the $\not\!\!E_T$ carried by unobserved particles by knowing the p_T of the observed ones.

The $t\bar{t}$ and WZ backgrounds are characterized by a large $\not\!\!E_T$ due to the presence of one or two neutrinos in those events. This type of $\not\!\!E_T$ is known as the "real" $\not\!\!E_T$ as it is due to a real neutrino. However, in the ZZ events as well as $Zb\bar{b}$ and Zb a small $\not\!\!E_T$ is seen. This

is due to poor measurement of jets, etc. This is known as "fake" $\not\!\!E_T$. The measured $\not\!\!E_T$ for simulated signal and backgrounds are shown in Figure 5.8. In this analysis, I require the event to have a $\not\!\!E_T < 24$ GeV as the simulated signal event is characterized by a low instrumental $\not\!\!E_T$ shown in Figure 5.8.

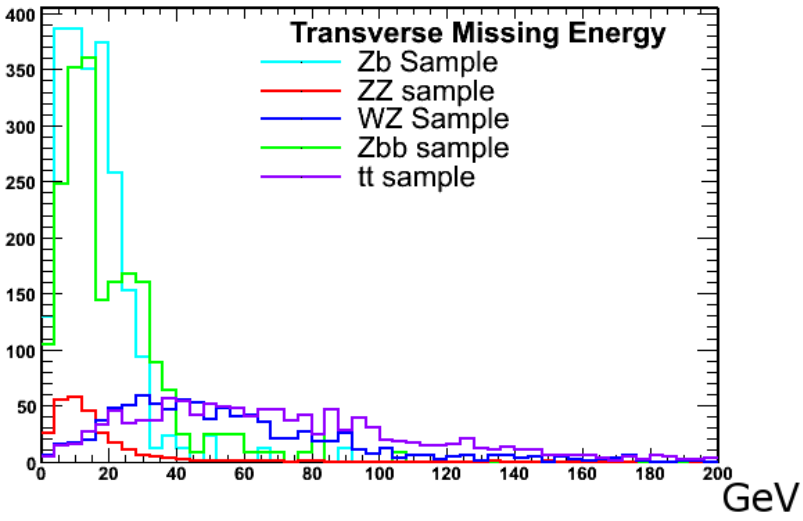

Figure 5.8. Transverse missing energy in signal and background in reconstructed 3 medium electron events normalized for luminosity of 1 fb^{-1}. The ZZ is scaled by a factor of 10, $t\bar{t}$ by a factor of 2, and WZ by a factor of 3.

In ATLAS, the $\not\!\!E_T$ reconstruction procedure starts with calibrated calorimeter cell energies and the reconstructed muons. The muon term is calculated from the momenta of the muons measured using the stand-alone spectrometer. The energy loss of the muons in the calorimeter is taken into consideration in the calorimeter term. To reduce the impact of fake muons, only muons with a matching track in the inner detector are considered; one has to consider the energy lost in the cryostat and between the barrel and the electromagnetic and tile calorimeters. Hence, a cryostat term should be added for energy correction; it is found to be non negligible for high p_T jets with 5% contribution for each jet with p_T above 500 GeV.

Finally, the association of each high p_T object in the event to a global calibrated cell is performed to refine the calibration of $\not{E}_T$. It is done by a carefully chosen order of reconstructed objects, electrons, photons, hadronically decayed τ's, b jets, light-quark jets and muons. Therefore, the energy of the calorimeter clusters is replaced by the energy of corresponding particles and jets. The cells that passes the noise cuts are also included if they are not associated with any high p_T object. Thus, a final $\not{E}_T$ is evaluated.

Chapter 6

THREE LEPTON SELECTION

In the previous chapters, we motivated the search for Z pair production in three lepton final states. We described the algorithms used in particle identification that we can use in our analysis, as well as Monte Carlo data production. As discussed in previous chapters, the sliding window algorithm, which is designed for electron identification, has limitations in η coverage and in crack regions. Therefore, I pursued a ZZ search first in a three lepton channel as it has a much higher acceptance than the four lepton channel. Although the three lepton channel has a higher acceptance, it suffers from a higher background which consists mainly of leptons from $Zb\bar{b}$, Zb, WZ, and $t\bar{t}$. I estimate the relative signal and background yields after my event selection.

6.1. Electron Multiplicity

As mentioned before, electron identification in ATLAS is based on a sliding window algorithm which covers only the central region of the detector. Figure 6.1 shows the number of reconstructed electrons in a $ZZ \rightarrow 4e$ event (left) and similarly for $Zb\bar{b} \rightarrow 3l$ (right). Because the number of events with three reconstructed electrons is twice the number of events with four reconstructed electrons, I pursued a ZZ search in the three leptons channel.

The signal and background have distinctive final state signatures. The ZZ event is characterized by four high p_T, isolated, and prompt leptons. Two isolated and prompt leptons are produced by the Z decay in the $Zb\bar{b}$, Zb and WZ backgrounds. The third lepton comes from the b-jet in $Zb\bar{b}$ and Zb. The lepton produced in the semi-leptonic decay of a b quark has lower p_T. In the case of the WZ background, the cross section is higher and the leptons are isolated with high p_T. However, the decay of the $W \rightarrow e\nu$ or

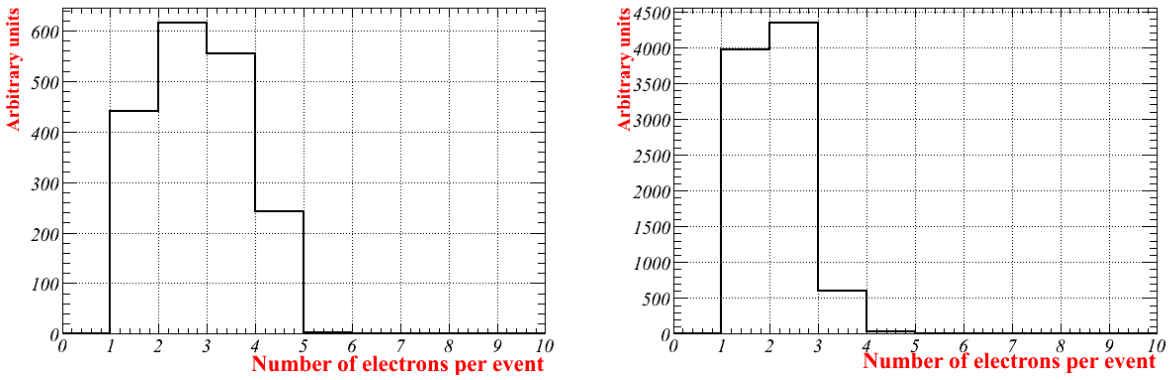

Figure 6.1. Number of electrons reconstructed in an event of $ZZ \longrightarrow 4e$ (left) and in the $Zb\bar{b} \longrightarrow 3e$ background (right).

$\mu\nu$ results in a large $\not\!\!E_T$. Similarly, the $t\bar{t}$ has a large $\not\!\!E_T$ and the leptons are of lower p_T and less isolated. However, in the signal events as well as in the $Zb\bar{b}$ and Zb backgrounds, the $\not\!\!E_T$ is instrumental and smaller than 20 GeV. Therefore, I set a pre-selection cut which provides a way of selecting events with the main characteristic of the signal events while giving a reasonable background rejection.

6.2. Kinematic Distributions

The difference in kinematic distributions between signal and background can be used to distinguish between them. The p_T distributions of the three reconstructed electrons when p_T ordered are shown in Figures 6.2 and 6.3 for both signal and main backgrounds. The first leading electron is the one with the highest p_T in the event and so on for the second and third leading electrons. While the first and second leading electrons in the background are most likely to both originate from Z decay, the third leading electron is most likely from a b quark. As shown in Figures 6.2 and 6.3, the third leading leptons in $Zb\bar{b}$ and Zb events are generally very low p_T. In ZZ events, all the three electrons are originating from the two Z bosons and they have a high p_T.

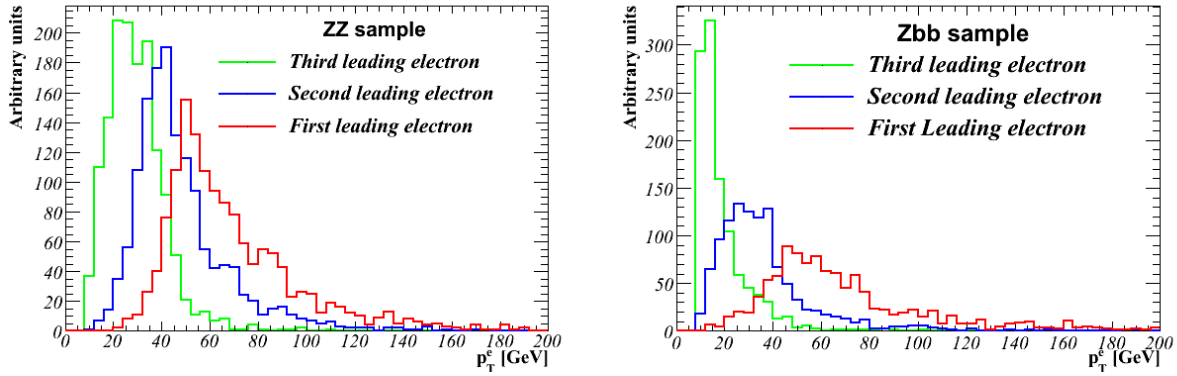

Figure 6.2. The p_T spectra of the three reconstructed electrons, in the ZZ events (left) and $Zb\bar{b}$ background (right). The third leading lepton in $Zb\bar{b}$ is generally very low p_T.

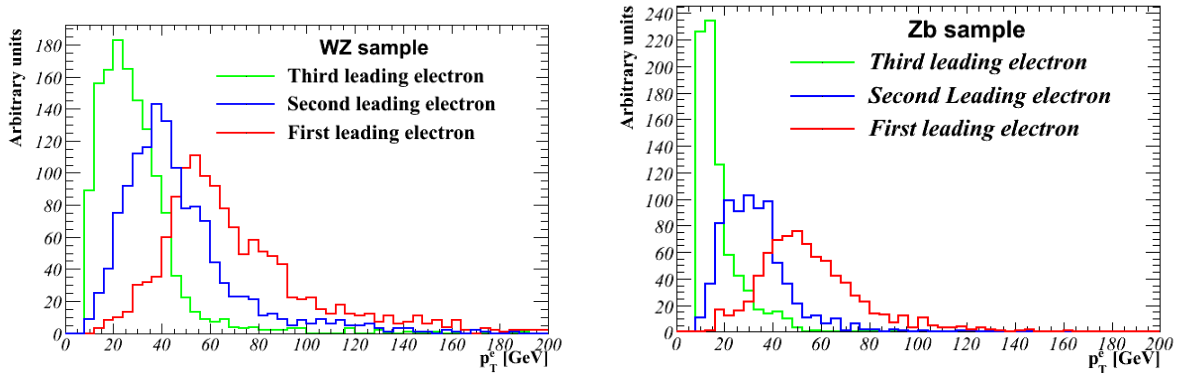

Figure 6.3. The p_T spectra of the three reconstructed electrons, in the WZ background (left) and Zb background (right). The third leading lepton in Zb is generally very low p_T.

6.3. Pre-selection

There are two sets of decay channels in this study which can give rise to an unidentified electron. The first one is based on events with three reconstructed "medium" electrons and the second one is based on two STACO muons and one medium electron which are reconstructed in the pseudorapidity range of $|\eta| < 2.5$. Leptons from $t\bar{t}$, $Zb\bar{b}$ and Zb are most likely to originate from displaced vertices. This is due to the relatively long lifetime of the b quark. To reduce theses backgrounds, we used the distance of closest approach (DCA) significance as described in Chapter 5. The leptons originating from ZZ events are isolated while those originating from $t\bar{t}$, $Zb\bar{b}$, and Zb are not isolated. Thus, we require isolation on reconstructed leptons. For more information about the medium cuts applied on electrons, STACO muons, DCA significance parameter, and isolation variable, the reader may refer to Chapter 5.

We require the p_T of the three leptons in the event to be higher than 10 GeV as the third-leading lepton in the background is generally low p_T. Moreover, we require events to have a small $\not{E}_T$ as $t\bar{t}$ and WZ events are characterized by large $\not{E}_T$. We consider only events with on-shell Z bosons.

We summarize the pre-selection cuts of the three lepton events in Table 6.1. The efficiency of these cuts are shown in Table 6.2. The efficiency is calculated for the $3e$ channel and the cuts shown in Table 6.2 are applied on all three electrons. The pre-selection cuts were chosen by inspection of the distribution of each variable. The p_T cut on leptons was chosen to be higher than 10 GeV as the third leading lepton on the main background event has a low p_T. The impact parameter significance cuts are chosen in such a way that the loss in signal efficiency is tolerable (-3%) while the background rejection improves, and similarly with the isolation cuts and the transverse missing energy.

p_T of the lepton	$p_T^e > 10GeV$ *and* $p_T^\mu > 10\ GeV$
DCA significance	DCA < 5 for electrons , DCA < 3 for muons
Isolation	< 0.14 for all the three selected leptons
Missing Energy	$\not{E}_T < 24\ GeV$

Table 6.1. Initial selection of the three leptons.

Process	$\epsilon(p_T^{3e} > 10\ GeV)(\%)$	$+\ \epsilon$(DCA)(%)	$+\ \epsilon$(Isolation)(%)	$+\ \epsilon(\not{E}_T)(\%)$
ZZ	36±0.3	33.2±0.31	32.4±0.34	28.2±0.31
$Zb\bar{b}$	16±0.2	9.1±0.1	3.1±0.1	2.5±0.1
Zb	16±0.3	8.4±0.2	4.2±0.1	3.23±0.12
WZ	39±0.4	28.3±0.36	24.6±0.35	4.2±0.1
$t\bar{t}$	8±0.1	2.86±0.08	0.54±0.01	0.05±0.01

Table 6.2. Efficiency of signal and background selection with different cuts applied in the $3e$ channel. The uncertainties are statistical.

6.4. Identifying One Z Boson

In a background event such as $Zb\bar{b}$ or Zb, the first leading electron and the second leading electron come from the Z decay. Thus a combination of the first leading electron and the second leading electron will give an invariant mass near the Z mass as shown in Figure 6.4. The third leading electron comes from the b quark. If we consider a configuration of first-leading and third-leading electron, a mainly flat distribution will be seen. However, in the case of the ZZ events the electron in the direction of the Z will get a boost and hence a higher p_T. As shown in Figure 6.4, the first leading electron in that case will be from one Z while the second leading electron will be from the other Z. This is true only in the case of the $3e$ channel. This combinatorics issue does not appear in the $2\mu 1e$ channel as the two reconstructed muons should originate from the same Z boson. As a consequence, the $2\mu 1e$ channel has a built in suppression of $Z \rightarrow e^+e^-$ and $b\bar{b} \rightarrow \mu\mu$.

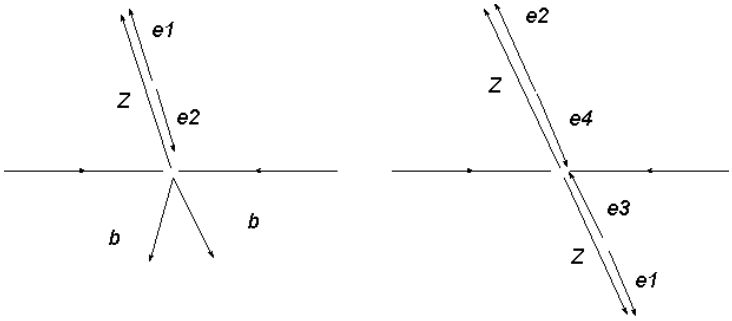

Figure 6.4. The expected p_T of electrons in ZZ events and $Zb\bar{b}$ background events. $e1$ is for the first leading electron in p_T, $e2$ for the second leading electron p_T and so on in the $3e$ case.

We defined a new variable M_{Zbest} by using the invariant mass of two combinations with verified opposite electric charges. We evaluate the invariant mass of the first-leading electron and third-leading electron or second-leading electron and third-leading electron. The variable M_{Zbest} is chosen as the combination that gives the closest invariant mass

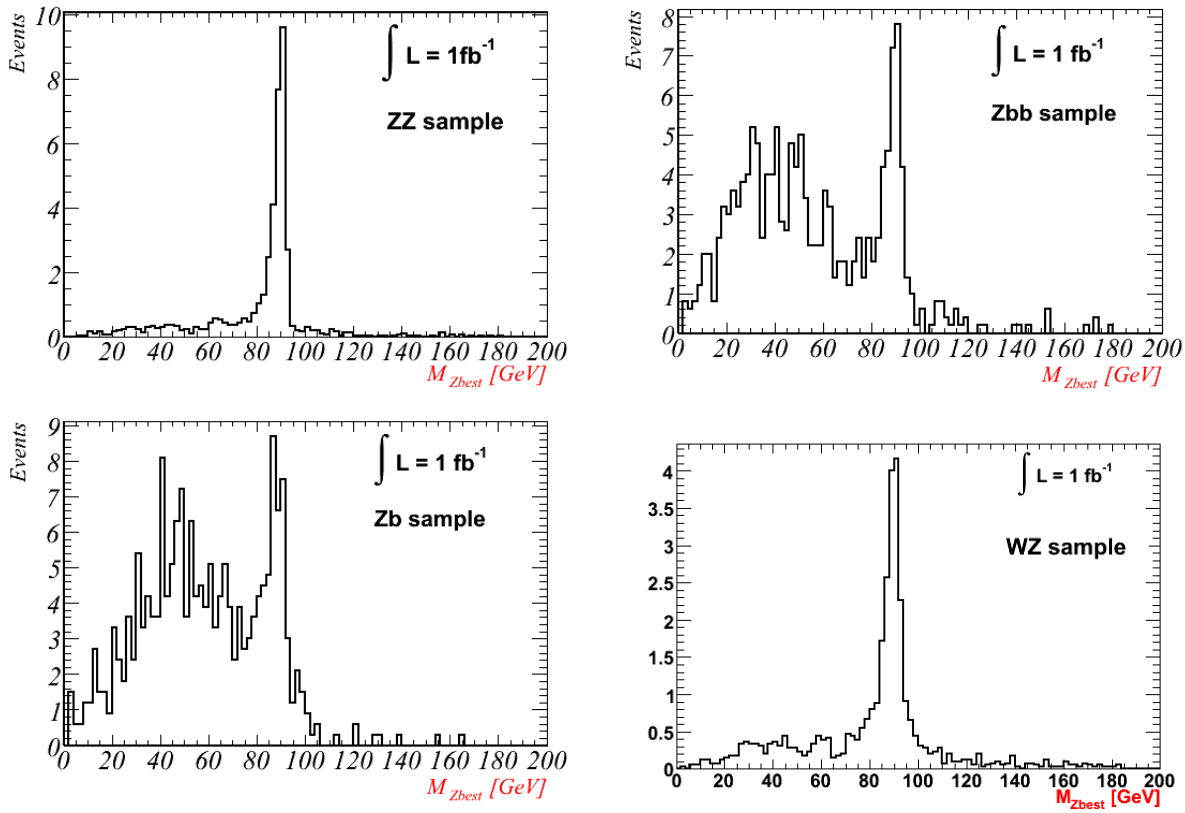

Figure 6.5. The M_{Zbest} variable in ZZ, $Zb\bar{b}$, WZ, and Zb samples in the $3e$ channel scaled for 1 fb^{-1}.

to the nominal Z mass as shown in Figure 6.5. In the case of the signal, one can see a peak within a certain window around the nominal Z mass. However, a mainly flat distribution can be seen in the case of the main background. In the case of the $2\mu 1e$ channel, the Z peak originates from the two muons reconstructed in the event. M_{Zbest} is shown in Figure 6.5 in the $3e$ channel for signal and main backgrounds normalized to 1 fb^{-1}. To reject a higher amount of background, we will require M_{Zbest} to be within a certain window of the Z mass. A window of 75 GeV $< M_{Zbest} <$ 100 GeV was used, but the main backgrounds $Zb\bar{b}$ and Zb remain high due to their high cross sections. The event yields for both channels are shown in Table 6.3. The final background yield is too high and requires more rejection. For that purpose, I will attempt to partially reconstruct the unidentified electron. I developed a set of techniques to partially identify electrons which I describe in detail in the following chapter.

Process	N^{3e}_{events}	$N^{2\mu 1e}_{events}$
ZZ	3.46±0.11	4.87±0.12
$Zb\bar{b}$	40.6±4.29	45.4±4.63
Zb	55.3±6.2	71.4±7.05
WZ	4.3±0.5	7.42±0.62
$t\bar{t}$	2.1±0.8	4.96±1.21
Total BG's	102.3±7.598	129.2± 8.543

Table 6.3. Number of events after cuts for 1 fb^{-1} in both channels with a cut on the Z boson mass ($75 < M_{Zbest} <$ 100 GeV). The errors are binomial.

Chapter 7

PARTIALLY RECONSTRUCTED ELECTRONS

Further background rejection requires partial reconstruction of the unidentified electron. The inefficiencies in track, cluster reconstruction, and crack regions have an impact in the central region in terms of electron reconstruction efficiency. Moreover, the standard electron identification algorithm has a restriction in $|\eta|$ coverage. At the time when I started this analysis, electron reconstruction in the forward region was not available. Based on observed inefficiencies in electron reconstruction, I identified an algorithm which does not assume or require a track and does not have a restriction in $|\eta|$. Moreover, it should not have shower shape requirements and should retain a whole cluster across the detector cracks. Clusters found via such an algorithm could correspond to the potential unidentified electron. It will be necessary to pass some basic particle identification. Therefore, I developed a set of techniques for particle identification applied to this algorithm. In the more recent ATHENA releases, a separate study from mine but similar in its use of topological clusters has led them to be adopted for electron identification in the forward region [60].

7.1. The Unidentified Electron

The ATLAS detector has several crack regions which affect particle identification in $\eta = 0$ and $|\eta| = 1.4$, as well as the forward region $|\eta| > 2.5$ where tracking information ceases to exist. The unidentified electron would most likely be found in these uncovered regions as shown in Figure 7.3. The unidentified electron originating from a ZZ should have a p_T distribution of an electron coming from a Z boson. Thus, this partially reconstructed electron will form an invariant mass with the electron that did not participate in forming M_{Zbest} such that it also peaks at the Z boson mass. In the case of $2\mu 1e$, the

partially reconstructed electron will form an invariant mass with the one electron in the event. However, the background will be non-resonant and will form mainly a flat distribution with the electron that did not participate in M_{Zbest}. A crude particle identification with a requirement of two Z bosons in the event can be applied to reduce the background.

7.2. Reconstructing Unidentified Electrons as Calorimeter Clusters

Further background rejection requires that we partially reconstruct the unidentified electron. I define the efficiency of the algorithm in finding the unidentified electron as follows:

$$\epsilon = \frac{N^{cluster}(\Delta R < 0.2)}{N^{ue}} \tag{7.1}$$

where $N^{cluster}$ is the number of reconstructed clusters matching unidentified electrons N^{ue} within a cone of radius ΔR. Truth information from the Monte-Carlo signal was used to check the efficiency of a clustering algorithm in finding the unidentified electron. I defined the p_T resolution as follows:

$$p_T^{resolution} = \frac{p_T^{reconstructed} - p_T^{truth}}{p_T^{truth}} \tag{7.2}$$

I tested all clustering algorithms available in the ATHENA releases that I used. This included the sliding window, jets, topological cluster, tau jets and EM topological cluster algorithms. The summary of different algorithms' performance for the ZZ signal is shown in Table 7.2. The jet and topological cluster algorithms are the most efficient as the $|\eta|$ coverage is high $|\eta| < 4.9$. The EM topological cluster, sliding window, and tau jet algorithms are restricted to the more central region with $|\eta|$ limits of 2.5, 2.5, and 3.2, respectively. This explains their lower efficiency than the topological cluster and the jet cone of $\Delta R = 0.4$. The efficiency of the algorithms tried are summarized in Table 7.1. Given that the jet cone of $\Delta R = 0.4$ and the topological cluster algorithms are the most efficient, I will consider only these two algorithms in further analysis.

Algorithm	Efficiency %	p_T resolution	$\Delta\phi$ resolution	$\Delta\eta$ resolution
sliding window	60 ± 1.1	0.19	0.009	0.018
Jets C4	92 ± 0.4	0.25	0.02	0.028
Topological Cluster	96 ± 0.3	0.22	0.02	0.023
Tau	54 ± 1.1	0.29	0.028	0.028
EM Topological Cluster	75 ± 0.6	0.33	0.03	0.030

Table 7.1. Efficiencies of finding the unidentified electron, p_T resolution, and η and ϕ resolutions of different algorithm performances for the ZZ sample.

7.2.1. Jet Cone Algorithm

I used the jet algorithm to find the unidentified electron as it has the advantages of good behavior near cracks and in the forward region. It was also the only option in the data when I began this study. The reconstructed electrons were also reconstructed by the jet algorithm. Before searching for the unidentified electron, I removed jets corresponding to medium electrons by requiring a $\Delta R = \sqrt{(\Delta\phi)^2 + (\Delta\eta)^2} > 0.2$ between the reconstructed electrons and the jets. A collection of "jet candidates" was created in which potential electrons were reconstructed via the cone jet algorithm of $\Delta R = 0.4$.

The efficiency of the jet algorithm in finding the unidentified electron is $(92 \pm 0.4)\%$ as calculated by Equation 7.1. The p_T spectra are shown in Figure 7.1 (left), where the p_T of the truth electron (red) and the p_T of the jet matched to truth (blue) are seen to be similar. The p_T of the jet candidate is slightly higher than the p_T of the matching truth electron. This is due to the fact that a cone of $\Delta R = 0.4$ is quite large for an electron and non-electron objects are included in the cone, which results in larger p_T. The jet algorithm covers the forward region as shown in Figure 7.1 (right) which shows the η distribution of partially reconstructed electrons which extends beyond $|\eta| > 2.5$. Moreover, many electrons that were not reconstructed by the sliding window in the central region are recovered by the jet algorithm.

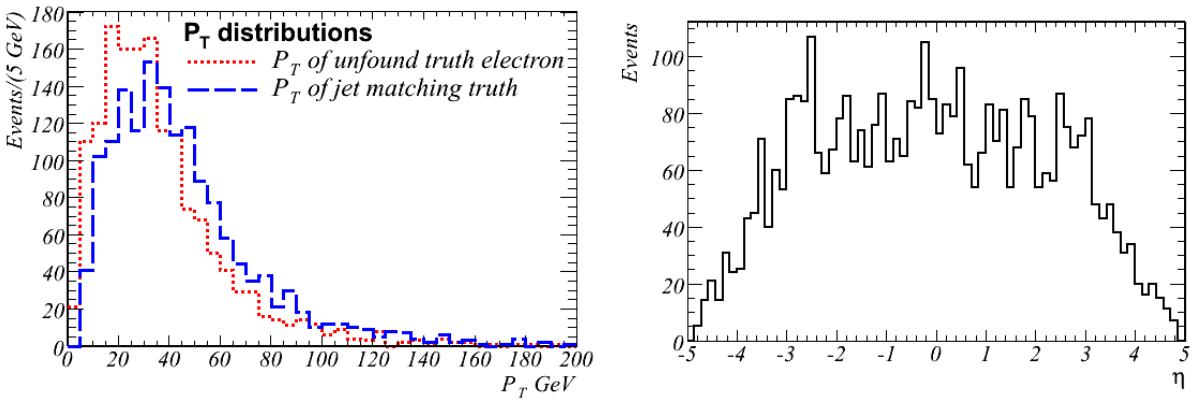

Figure 7.1. p_T distributions of the truth electron and the jet matching the truth electron (left) in ZZ sample. The η distribution of the jet candidate in ZZ sample (right).

The p_T resolution is comparable to the sliding window if the transverse momentum of the partially reconstructed electron is higher than 20 GeV, as shown in Figure 7.2 (right). However, the p_T resolution worsens in the case of low p_T for the unidentified electron. This is a particular difficulty for the jet algorithm at low p_T.

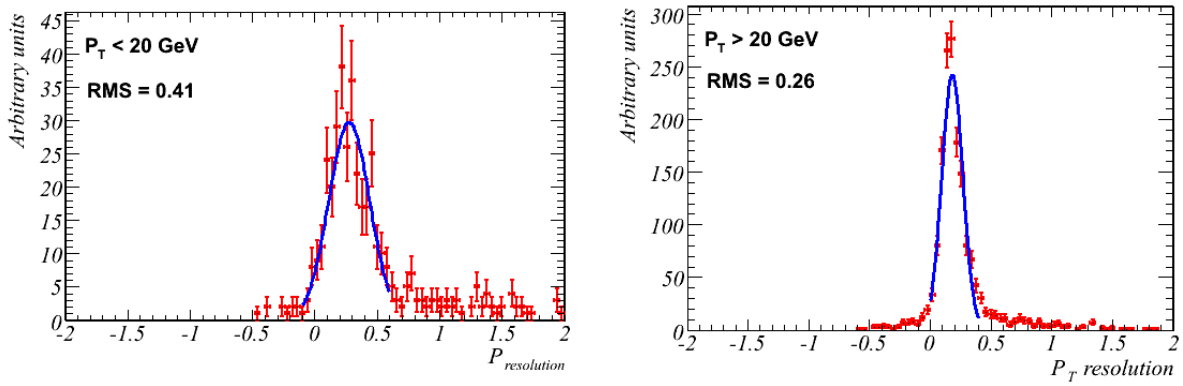

Figure 7.2. p_T resolution of the unidentified electron in ZZ events in two p_T ranges: lower than 20 GeV (left) and higher than 20 GeV (right), in the case of the jet algorithm ($3e$+"e"). There an offset in the p_T resolution.

7.2.2. Topological Cluster

In the same fashion, I used the topological cluster algorithm to find the unidentified electron; its efficiency in finding the unidentified electron was found to be $96 \pm 0.2\%$. The p_T distributions of the topological cluster (blue) matching the truth and the truth electron (red) seem to be in good agreement as shown in Figure 7.3 (left). However, a small disagreement can be seen at lower p_T which is due to the cluster splitting in the crack region. The η coverage beyond the $|\eta| > 2.5$ is covered as seen from the η distribution shown in Figure 7.3 (right).

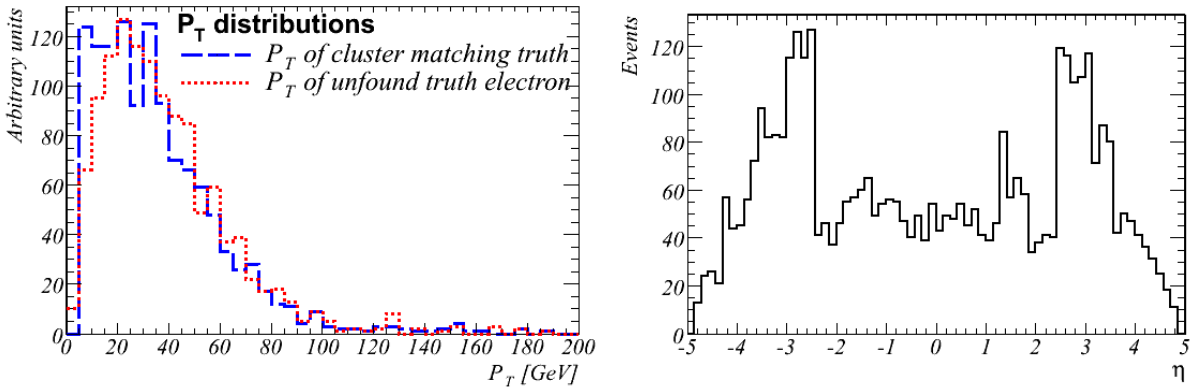

Figure 7.3. p_T distributions of the truth electron and the cluster matching the truth electron in the ZZ sample (left). The η distribution of the cluster candidate in the ZZ sample (right).

The p_T resolution is comparable to the sliding window algorithm, especially at high p_T. The p_T resolution at lower transverse momentum tends to be somewhat worse but still comparable to sliding window algorithm. The p_T resolution is shown in Figure 7.4 for $p_T < 20$ GeV (left) and $p_T > 20$ GeV (right).

The requirement of a fourth cluster in the event with p_T threshold would not provide a decent improvement in S/B. Further distinguishing the unidentified electron from the fakes requires some degree of particle identification.

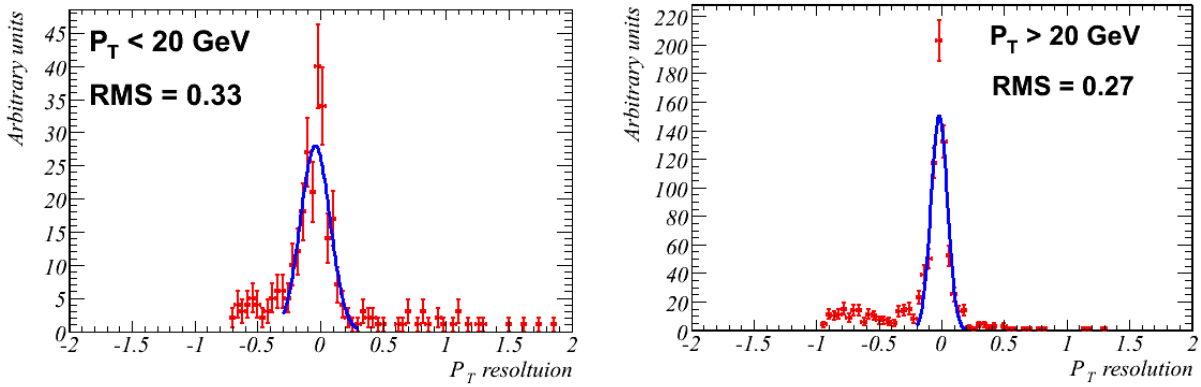

Figure 7.4. p_T resolution of the unidentified electron in two p_T ranges: lower than 20 GeV(left) and higher than 20 GeV (right), in the case of the cluster algorithm.

7.3. Particle Identification

The object that was identified as the partially reconstructed electron by either the jet algorithm or the topological cluster should then pass some degree of particle identification. I used a set of variables that were available in the current release of the analysis (release 13) in each algorithm to discriminate real electrons from fake ones. In the case of the jets, I have chosen a cut-based approach, while I built a likelihood method in the case of the topological cluster.

7.3.1. Jet Cone Algorithm

The $Zb\bar{b}$ and Zb channels are the main backgrounds that remain high due to the high cross section and to the presence of a real Z boson in the event. In order to reject the background from b jets, I have chosen the jet candidate in order to exclude those jets which originated from the b quarks. This was done by using the secondary-vertex finding in the ATLAS b-tagging algorithm. Figure 7.5 shows the SV2 variable for both signal and background. The jet is tagged as a b-jet if SV2 > 0. A summary of the b-veto efficiencies is shown in Table 7.2. There is only a 5% chance that partially reconstructed electrons in ZZ events will be tagged as a b-jet. I select events with SV2 < 0 which provides a background rejection by a factor of 2 in $Zb\bar{b}$ and Zb.

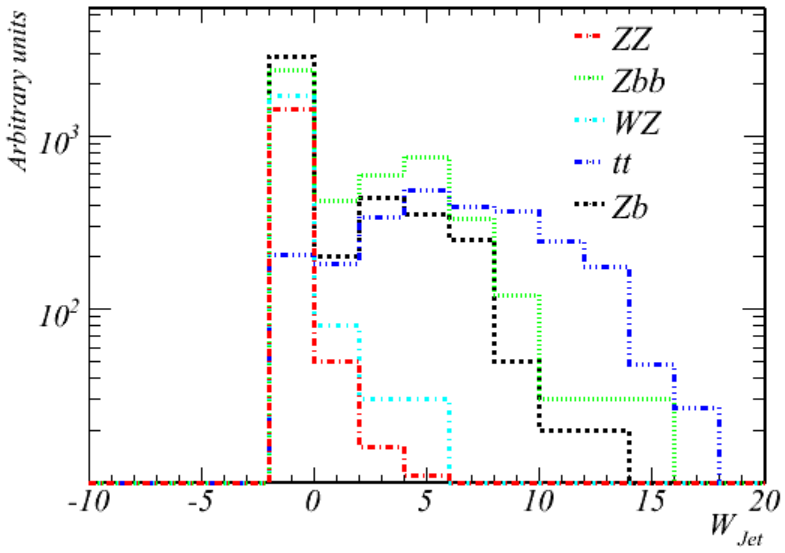

Figure 7.5. Secondary vertex.

Process	b-tagging veto efficiency (%)
ZZ	95±0.1
$Zb\bar{b}$	49±0.3
Zb	56±0.4
$t\bar{t}$	20±0.06
WZ	92±0.2

Table 7.2. b-veto efficiencies for signal and background.

Unlike an electron, which will deposit all its energy in the EM calorimeter, a jet will leave most of its energy in the hadronic calorimeter during the showering. However, a fraction of that energy will be deposited in the EM calorimeter, mainly due to the existence of neutral pions ($\pi^o \rightarrow 2\gamma$) or soft electrons from b and c quark decay in the jet. Therefore, the fraction of energy deposited in the EM calorimeter can be useful to distinguish between a real electron and a fake one.

The EM fraction (EMF) is defined as the ratio of the sum of energies of the partially reconstructed electron deposited in each layer of the EM calorimeter to the total energy of the jet as shown in the following equation.

$$EMF = \frac{\sum_i E_i^{EM-layers}}{\sum_i E_i^{All-layers}} \tag{7.3}$$

where $\sum_i E_i^{EM-layers}$ are the energies of all constituent cells in the EM layers of the calorimeter and $\sum_i E_i^{All-layers}$ are the energies of all constituent cells in all layers of the calorimeters.

An electron will leave most of its energy in the EM calorimeter, while a jet will leave a smaller fraction. Figure 7.6 shows the EMF for ZZ and background samples in the barrel (left) and endcap (right). In the ZZ sample, the partially reconstructed electron (in red) is matched to the truth electron. It is evident that all of these partially reconstructed electrons have deposited more than 80% of their energy in the EM calorimeter. In the case of the background, the bulk EM fraction ranges from 20% to 80% with some events with higher EMF. I obtain a sufficient background rejection and signal efficiency by selecting the partially reconstructed electron with an EMF higher than 80% in the barrel (85% in endcap).

After the partially reconstructed electrons have passed the EMF cut, the first-leading jet in the event was taken to be the potential unidentified electron for the ZZ analysis. The EM fraction applied on the jet candidate provided a background rejection factor of four.

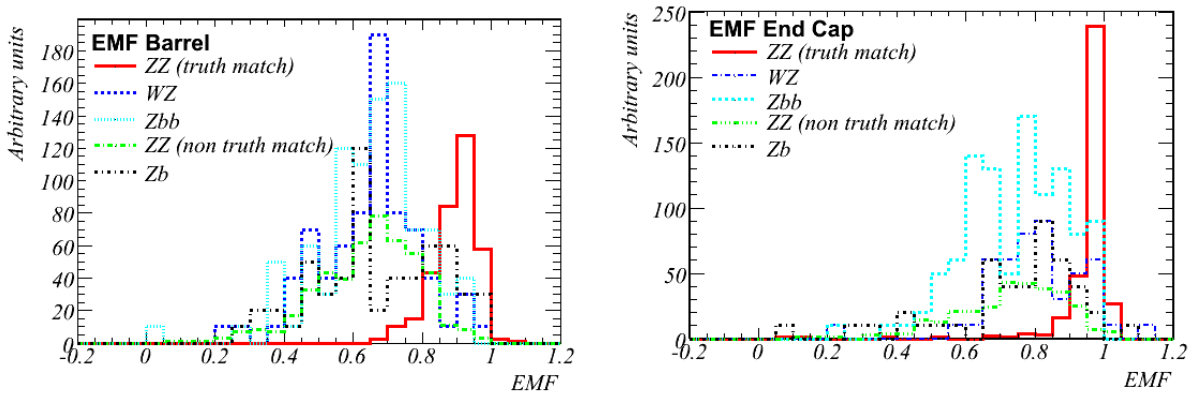

Figure 7.6. The EM fraction for both signal and background in barrel (left) and endcap (right).

$\|\eta\|$ regions	Signal efficiency (%)	$f_b^{Zb\bar{b}}$ (%)	f_q^{WZ} (%)
Barrel	78±1.9	12±1.3	14±1.6
End Cap	81±1.5	15±1.4	18±1.9
FCAL	75±1.2	1±0.7	1±0.4

Table 7.3. Identification selection efficiency for the partially reconstructed electron in the ZZ sample and fake rate for two backgrounds ($Zb\bar{b}$ and WZ) in different regions of the detector: barrel, endcap, and $FCAL$ using the jet cone algorithm. The low fake rate in the high $|\eta|$ region is due to the $|\eta|$ cut at the generation level. The efficiency is calculated as the ratio of the number of events passing the cuts to the number of original events.

7.3.2. Topological Cluster Parameters

Some of the properties of the shower shape, called moments, may be calculated to classify clusters and to help in particle identification and calorimeter calibration. The cluster moment of degree n for variable x is defined as:

$$< x^n >= \frac{1}{E_{norm}} \times \sum_i E_i x_i^n, \tag{7.4}$$

where $E_{norm} = \sum_i E_i$, E_i is the cell energy and i is the index of the cell in the cluster. The shower axis is needed as a reference for many of these moments. Once the shower axis $\overrightarrow{s}$ and the shower center $\overrightarrow{c}$ are defined, one can calculate two useful quantities. The first one is the distance of the cell i from the shower axis which can be defined as:

$$r_i = |(\overrightarrow{x}_i - \overrightarrow{c}) \times \overrightarrow{s}| \tag{7.5}$$

The second quantity, λ_i, is the distance of the cell i from the shower center along the shower axis. It is defined as:

$$\lambda_i = (\overrightarrow{x}_i - \overrightarrow{c}) \cdot \overrightarrow{s} \tag{7.6}$$

Two moments and two other parameters are calculated for each cluster and I used them to build a likelihood method.

- **The normalized second longitudinal moment**

  The longitudinal moment is defined as:

$$Longitudinal\ moment = \frac{long_2}{(long_2 + long_{max})} \tag{7.7}$$

  where $long_2$ is the second moment in λ_i, i.e. $long_2 = < \lambda_i^2 >$, where the two most energetic cells have their λ_i set to 0. We also defined, $long_{max} = < \lambda_i^2 >$, with $\lambda_i = 10$ cm for the two most energetic cells and $\lambda_i = 0$ for all other cells. This

moment gives normalized distributions between 0 and 1; 0 means that the shower is shorter, while 1 means the shower is longer. For example, the $\pi^{\pm}$ depositions are known to be deep, while the $\pi^o \rightarrow 2\gamma$ depositions are not. Figure 7.7 (left) shows the normalized second longitudinal moment in the cases of signal and background.

- **The normalized second lateral moment**

  The lateral moment is defined as:

$$Lateral\ moment = \frac{lat_2}{(lat_2 + lat_{max})} \tag{7.8}$$

  where lat_2 is the second moment in r_i, i.e. $lat_2 = < r_i^2 >$, where the two most energetic cells have their r_i set to 0. Similarly, $lat_{max} = < r_i^2 >$, with $r_i = 4$ cm for the two most energetic cells and $r_i = 0$ for all other cells. Again, this gives normalized distributions between 0 and 1. Thus, the value 1 means wide showers, and 0 means narrow showers. For example, the $\pi^{\pm}$ gives broad showers, while $\pi^o \rightarrow 2\gamma$ results in small concentrated ones. Figure 7.7 (right) shows the normalized second lateral moment in the cases of signal and background.

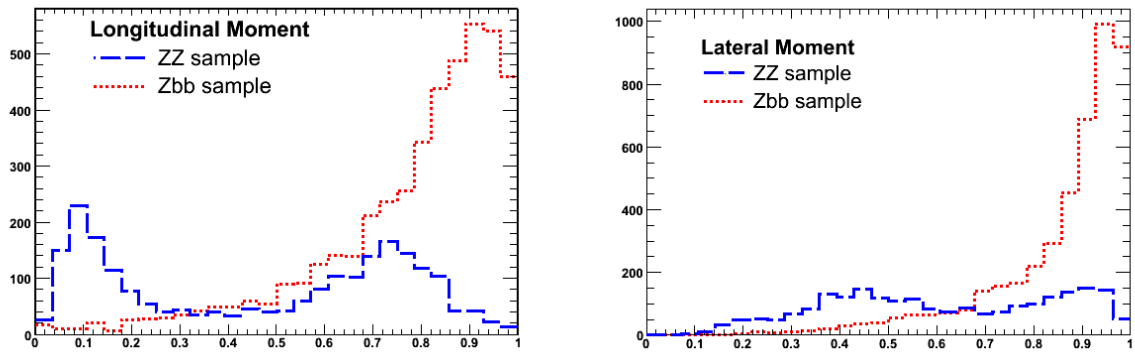

Figure 7.7. The second longitudinal moment in signal and background (left). The second lateral moment in signal and background (right).

- **Isolation**

  The isolation of each cluster is evaluated by the fraction of cells on its outer perimeter that are not included in other clusters. The isolation is calculated for each layer separately due to the variety of granularities. The overall isolation of a cluster is the layer-energy weighted average of the individual isolation ratios. An isolation of 0 means that all cells on its outer perimeter are included in neighboring clusters. A value of 1 means that the cluster is totally isolated. Figure 7.8 shows the isolation variable for both signal and background.

- **Maximum energy fraction**

  The measurement of the energy fractions deposited in the cells of a segmented calorimeter helps in distinguishing between hadrons and electrons. Figure 7.8 shows the Maximum energy fraction for both signal and background.

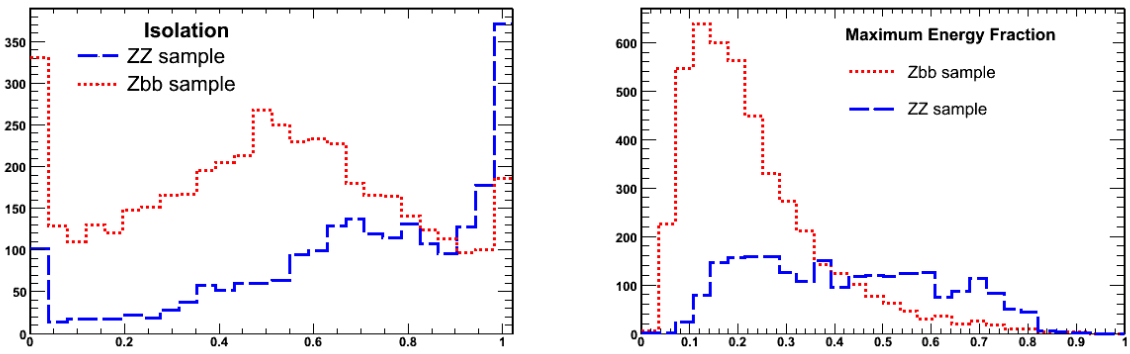

Figure 7.8. Isolation variable in signal and background (left). Maximum fraction energy of a cell in signal and background (right).

Because of the overlap between the signal and background distributions, the use of these variables as a rectilinear cut will not provide optimal signal efficiency and background rejection. In order to combine information from various variables into a single quantity that provides an optimal discrimination power, I rely on a multivariate technique, the likelihood method. This requires probability distributions for signal and background. The method uses knowledge of the probability of signal and background to have

a parameter x with specific values and calculates an overall likelihood to the signal. To differentiate between signal-like and fake-like electron candidates, I defined a likelihood discriminant as following:

$$L(x) = \frac{P_s(x)}{P_s(x) + P_b(x)} \tag{7.9}$$

The closer $L(x)$ tends toward 1, the more signal-like the candidate is, the closer $L(x)$ tends toward 0, the more background-like the candidate is. I used four variables with good discriminating power between real (signal) and fake (background) electrons to build the likelihood. Figure 7.9 shows the longitudinal moment versus the isolation variable for signal and background. The real electrons populate different areas than the fake ones. It is difficult to design an efficient 2D cut with these two variables; it is better to combine information from various variables into a single quantity that provides an optimal discrimination power. This can be done via the likelihood method.

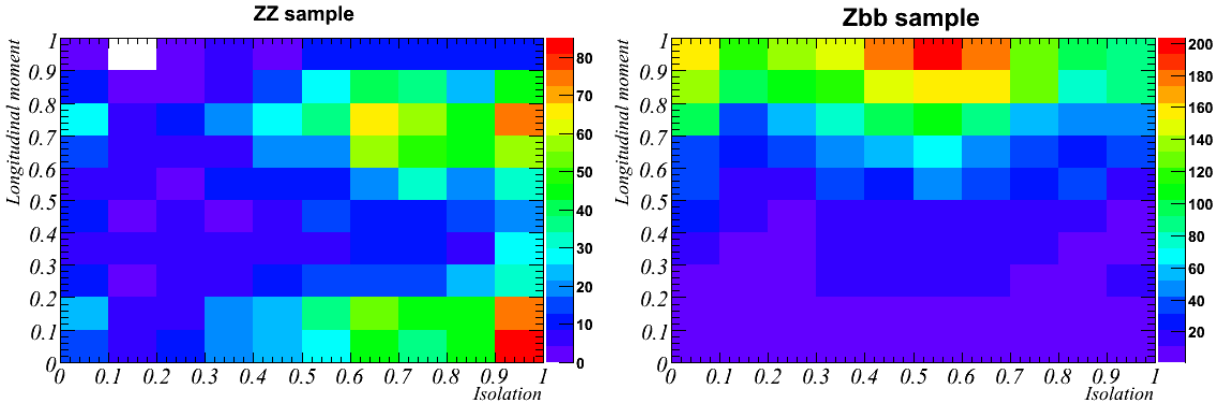

Figure 7.9. Longitudinal moment versus isolation in signal events (left). Longitudinal moment versus isolation in background events (right). The signal and background are found in different areas.

7.3.3. Topological Cluster Likelihood

There are various steps involved in the formulation of the likelihood function. First, the distributions in Figures 7.7 and 7.8 are normalized to a unit area to produce probability

distributions for each variable as shown in Figures 7.10 and 7.11. These distributions can be used to determine a probability for a given topological cluster to be signal, $P_s(x)$, or background, $P_b(x)$, where $\overrightarrow{x}$ is a vector of the likelihood variables. I used $Z \rightarrow e^+e^-$ for the signal probabilities and $t\bar{t} \rightarrow 4l$ to get the background probabilities as these two processes should be straightforward to isolate in early LHC data.

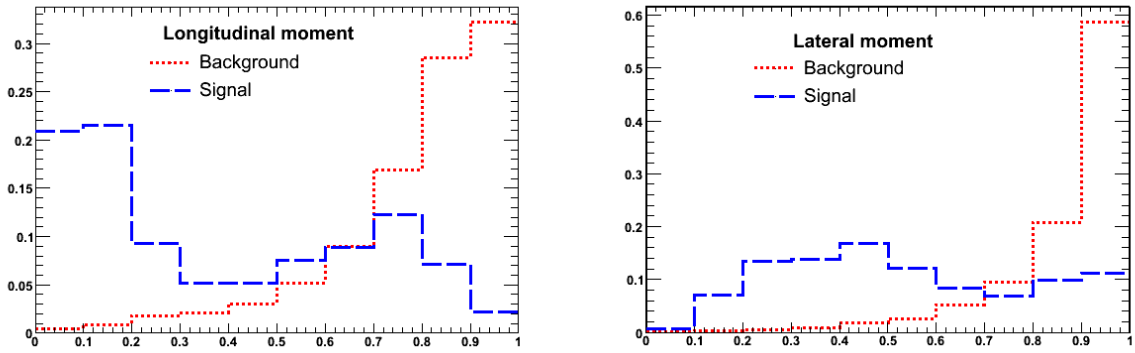

Figure 7.10. The normalized probability density functions of the second longitudinal moment in signal and background (left). The normalized pdf of the second lateral moment in signal and background (right).

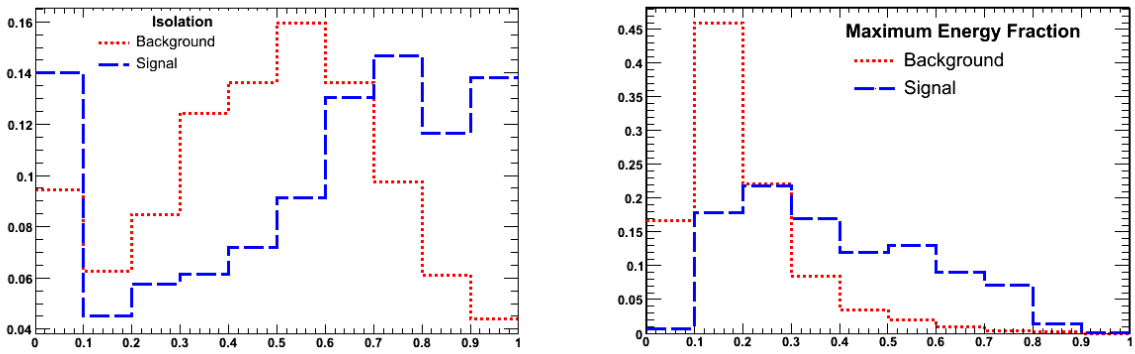

Figure 7.11. The normalized pdf of the isolation variable in signal and background (left). The normalized pdf of the maximum energy fraction in signal and background (right).

The multiplication of these variables gives the overall probability for each cluster to be a real electron $P_s(x)$ or a fake electron $P_b(x)$.

$$P_s(x) = \prod_i P_{s,i}(x_i) = P_s^{Longitudinal} \times P_s^{Lateral} \times P_s^{Isolation} \times P_s^{f_{Emax}} \tag{7.10}$$

$$P_b(x) = \prod_i P_{b,i}(x_i) = P_b^{Longitudinal} \times P_b^{Lateral} \times P_b^{Isolation} \times P_b^{f_{Emax}} \tag{7.11}$$

Figure 7.12 (left) illustrates the likelihood for the partially reconstructed (matched to truth) electrons in ZZ events and fake electrons from $Zb\bar{b}$ events with a good separation between them. For a likelihood cut of 0.3, we obtain 82% signal efficiency versus 20% background efficiency as a fake rate for each background sample as shown in Figure 7.12 (right).

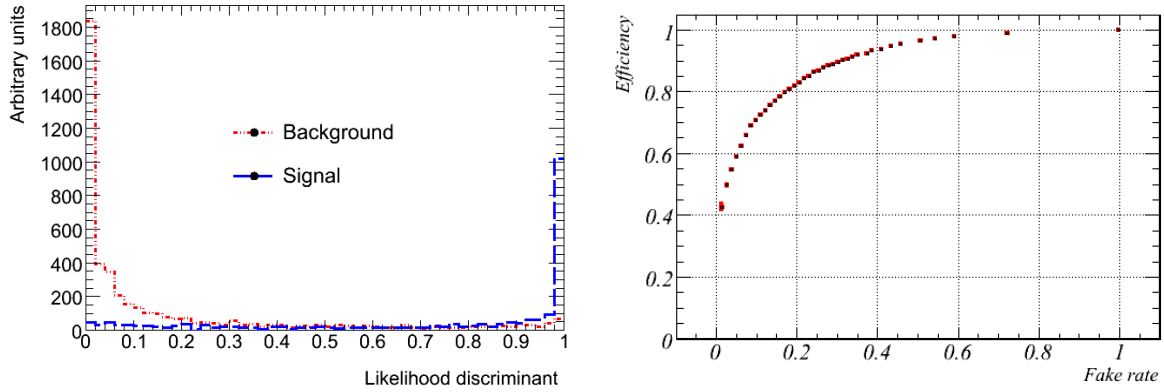

Figure 7.12. The distributions of likelihood for signal and $Zb\bar{b}$ background (left) and efficiency versus fake rate (right).

The choice of the MC background sample from which one can get the probability functions for the likelihood is crucial. To avoid any bias, I compared the background shapes and I found that they are similar as shown in Figure 7.13.

The likelihood can be improved by taking into account the fact that the cell sizes in the calorimeters are not uniform. Therefore, the likelihood is strongly η dependent. I divided the detector into seven regions in which the size of the cell is similar. In order to

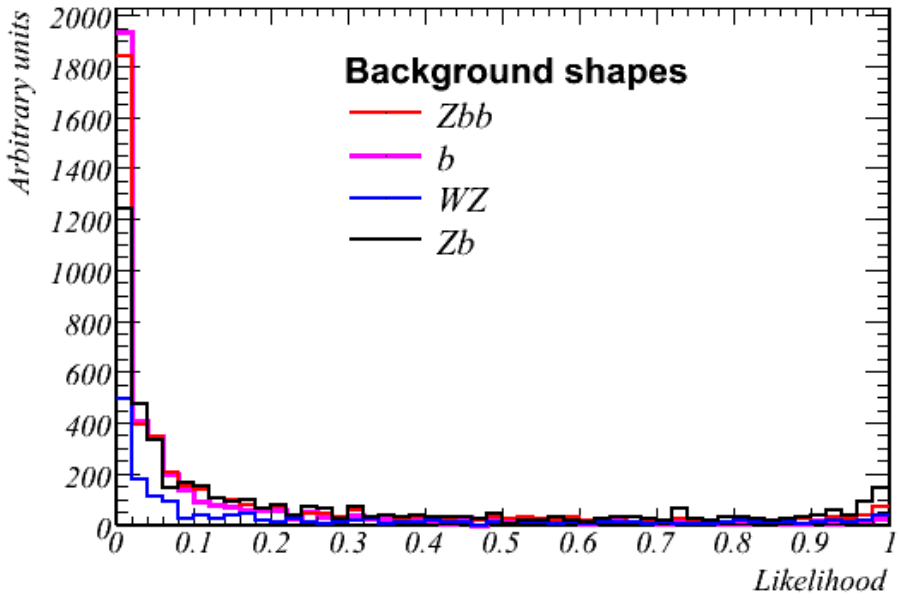

Figure 7.13. Background likelihood shapes.

optimize the likelihood, I used different probabilities in different $|\eta|$ regions. These results show an increase in the signal efficiency accompanied by a decrease in the fake rate as $|\eta|$ increases (Table 7).

The topological cluster has somewhat better efficiency, fake rate, and resolution. Using the jet algorithm to partially reconstruct the unidentified electron will result in a higher background as the anti-b-tagging will cease to be useful at $|\eta| > 2.5$. Given that the background shapes are similar in the likelihood and there are no tracking requirements, I believe that the topological cluster is the most suitable algorithm for our analysis.

η regions	Signal efficiency (%)	$f_b^{Zb\bar{b}}$ (%)	f_q^{WZ} (%)
$\|\eta\| < 0.7$	85±2.1	20±1.1	18±.9
$\|\eta\| > 0.7$ and $\|\eta\| < 1$	84±3.8	16±1.5	16±1.5
$\|\eta\| > 1$ and $\|\eta\| < 1.375$	86±3.1	18±1.4	17±1.3
$\|\eta\| > 1.375$ and $\|\eta\| < 1.9$	83±1.9	21±1.6	21±1.6
$\|\eta\| > 1.9$ and $\|\eta\| < 2.5$	90±1.7	13±1.4	12±1.4
$\|\eta\| > 2.5$ and $\|\eta\| < 3.2$	95±0.8	4±1	2±0.5
$\|\eta\| > 3.2$	89±1.6	3±1	2±0.4

Table 7.4. Signal selection efficiency of the unidentified electron in the ZZ sample and fake rate for two backgrounds ($Zb\bar{b}$ and WZ) in different regions of the detector at $L > 0.3$. The low fake rate in the high $|\eta|$ region is due to the $|\eta|$ cut at the generation level.

Chapter 8

Z BOSON PAIR PRODUCTION SEARCH

Upon investigating the three lepton analysis in Chapter 6, we concluded that finding the unidentified electron is crucial to lower the background. In Chapter 7, I developed a set of techniques to partially reconstruct the unidentified electron. In this Chapter, I apply these methods for the ZZ analysis.

8.1. Kinematics of the Partially Reconstructed Electron

The transverse momentum of the partially reconstructed electrons are similar to those of electrons originating from a Z boson after passing the identification requirements without relying on the truth matching. Figure 8.1 shows the p_T spectra of the partially reconstructed electrons. The electron found via the jet algorithm has a higher p_T in comparison with the ones found via the topological cluster. This is due to the large cone of the algorithm $\Delta R = 0.4$ with respect to the shower of an electron. As mentioned in Chapter 7, the topological clustering algorithm was found to be a better choice as a tool to partially identify electrons.

8.2. Purity of the Partially Reconstructed Electron

In order to check the purity of the partially reconstructed electron, we refer to truth information. After the partially reconstructed electron passed all the particle identification requirements, we evaluated the $\Delta R = \sqrt{\Delta\phi^2 + \Delta\eta^2}$ between the nearest truth electron and the partially reconstructed electron. We consider the partially reconstructed electron to be pure if $\Delta R < 0.2$. We have found that the purity of partially reconstructed electron is 86%±0.2%. The purity of the partially reconstructed electron was found to be 89%±0.2% in the case of the topological cluster.

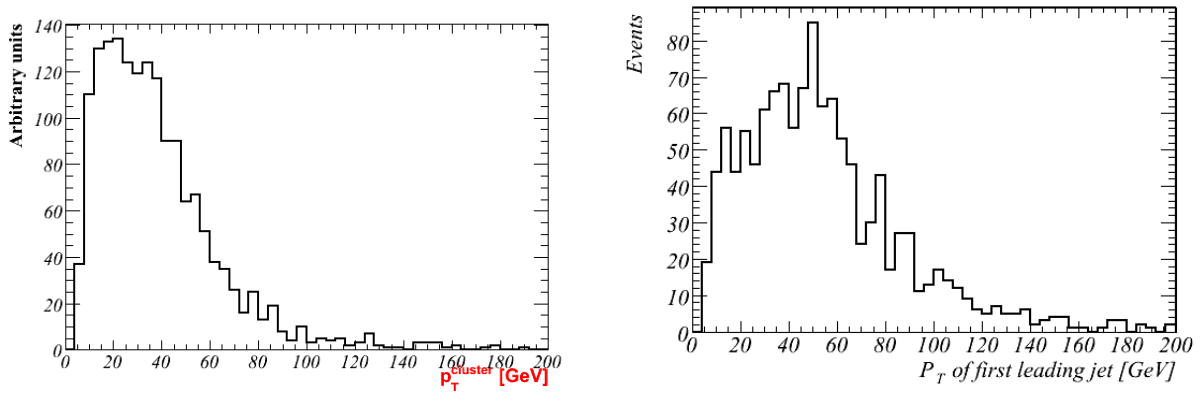

Figure 8.1. p_T spectra of the partially reconstructed electrons found via the topological cluster algorithm (left) and by the jet algorithm (right).

8.3. The Second Z Peak

The leading jet or topological cluster was taken to be the partially reconstructed electron after passing the EM fraction cut and SV2 veto, or the likelihood. In this analysis, the reconstructed electron which was not found to form the Z boson with another reconstructed electron was used to form a second Z with the partially reconstructed electron that passed the particle identification. This mass is termed $M_{Zsecond}$, and is shown in Figure 8.2 for the jet algorithm (left) and for the topological cluster (right). The second Z peak was very pronounced in the case of the ZZ sample while it was very spread in the case of the backgrounds.

The $M_{Zsecond}$ for the jet approach appears to be higher than the nominal mass of the Z boson which is 91.2 GeV. This is due to the size of cone ($\Delta R = 0.4$) of the jet algorithm which is bigger for the size of the shower of an electron. As a result, there is a possibility that parts of a non-electron cluster are in that cone. Moreover, there are two Z bosons in the event as shown in Figure 8.3 (left) which plots M_{Zbest} versus $M_{Zsecond}$ in the case of the jet algorithm. Similarly, Figure 8.3 (right) shows M_{Zbest} versus $M_{Zsecond}$ in the case of the topological cluster. The recovery of the unidentified electron in the signal event provides a strong cut for better background rejection. The main background does not

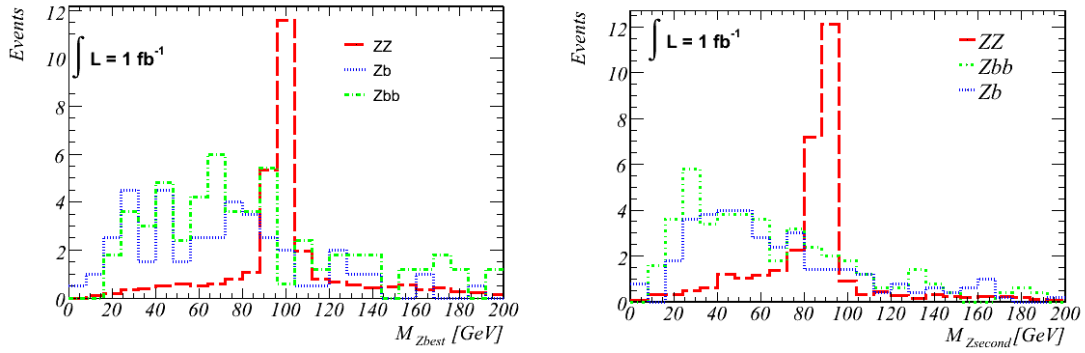

Figure 8.2. $M_{Zsecond}$ as found via the jet algorithm (left) and $M_{Zsecond}$ as found via the topological cluster algorithm (right)for signal and main backgrounds in the $3e$+"e" channel.

have a second Z in the event which make its distribution flat.

8.4. Final Selection Cuts

With the fourth lepton and the second Z boson identified, I designed a 2D cut which requires the two Z's in the ZZ decay to be on-shell in the event. This was done by requiring that M_{Zbest} should be between 75 GeV and 100 GeV and that $M_{Zsecond}$ should be between 85 GeV and 110 GeV simultaneously for the jet algorithm. Figure 8.3 shows a plot of M_{Zbest} versus $M_{Zsecond}$ in the case of the jet algorithm. In the case of the topological cluster, I required that M_{Zbest} and $M_{Zsecond}$ should be between 80 GeV and 100 GeV simultaneously. A summary of the final selection cuts is summarized in Table 8.1.

8.5. Event Yield Calculation

After the selection criteria described above, the background was reduced significantly in both the, $3e$ + "e" and $2\mu 1e$ + "e", channels. I summarize the event selection efficiency as well as the expected number of events for 1 fb^{-1} for both signal and background in Tables 8.2, 8.3, 8.4, and 8.5. Zero background events in the Monte Carlo samples ($Zb\bar{b}$,

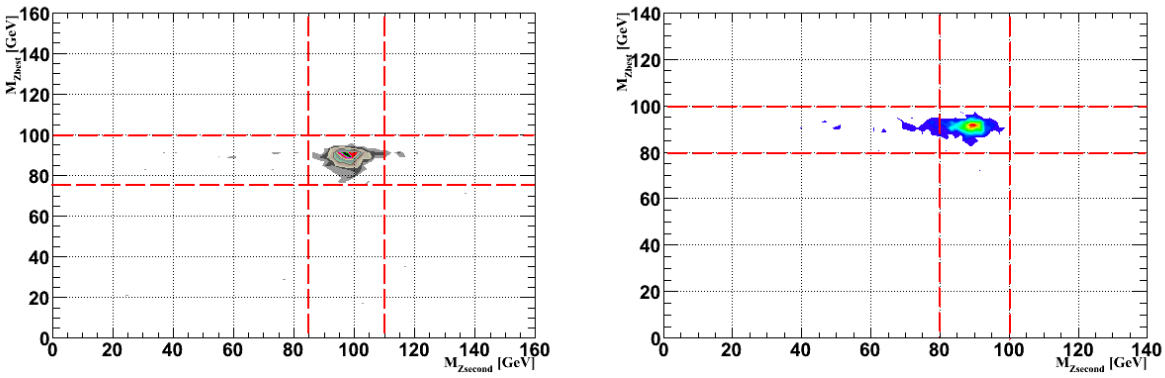

Figure 8.3. M_{Zbest} versus $M_{Zsecond}$ for signal and main backgrounds in case of the jet algorithm (left), and in the case of the topological clusters if likelihood is higher than 0.3 (right) in the $3e$+"e".

Cut	Jet Algorithm	Topological cluster
anti b-tagging	< 0	N/A
EMF (barrel,end-cap)	>0.8, >0.85	N/A
Likelihood	N/A	> 0.6
M_{Zbest}	$75 - 100\ GeV$	$80 - 100\ GeV$
$M_{Zsecond}$	$85 - 110\ GeV$	$80 - 100\ GeV$

Table 8.1. Final selection cuts. The partially identified electron is taken to be the leading cluster passing the identification cuts.

Zb, and $t\bar{t}$) passed the cuts and I assumed one event to estimate the background efficiency. Thus, the background may be overestimated. All the errors are statistical errors. The two algorithms used in partially identifying the electron showed fairly similar performance. The $t\bar{t}$ background becomes negligible after cuts because of $\not\!\!E_T$. The WZ background becomes very low despite its similarity with the signal signature, due to the $\not\!\!E_T$ cut as well as the requirement of having two Z peaks in the event. The $Zb\bar{b}$ and Zb channels are the main backgrounds in this analysis and their cross sections are quite large compared to the signal cross section.

An overall estimated signal-over-background ratio of 5 was reached for an integrated luminosity of 1 fb^{-1} for both algorithms. A search in the four lepton channel resulted in 13 signal events and 0.2 background events [61] for an integrated luminosity of 1 fb^{-1}. For the same luminosity, the $3e$+"e" plus the $2\mu 1e$+"e" channels presented here yield 4.7 signal events and 1.1 background events in the three lepton channel search we conducted. Therefore, a 36 % gain in acceptance can be achieved by considering the three lepton channel. In terms of significance $\frac{S}{\sqrt{S+B}}$, the three lepton channel increases from 3.6 to 4.1.

Channel $2\mu 1e + X$	ZZ	$Zb\bar{b}$	Zb	WZ	$t\bar{t}$
Selection ϵ (%)	4±0.13	(1±1)×10^{-3}	(2.5±2.5)×10^{-3}	(6±6)×10^{-3}	(2.5±2.5)×10^{-4}
Number of event	2.67±0.1	0.1±0.1	0.3±0.3	0.04±0.04	(1.5±1.5)×10^{-3}

Table 8.2. Event yields in 1 fb^{-1} for the $2\mu 1e$ + partially reconstructed electron channel using the jet algorithm.

Channel 3e+X	ZZ	$Zb\bar{b}$	Zb	WZ	$t\bar{t}$
Selection ϵ (%)	2.5±0.11	(3±3)×10^{-3}	(2.5±2.5)×10^{-3}	(2±1)×10^{-2}	(2.5±2.5)×10^{-4}
Number of event	1.67±0.07	0.3±0.3	0.3±0.3	0.1±0.08	(1.5±1.5)×10^{-3}

Table 8.3. Event yields in 1 fb^{-1} for the $3e$ + partially reconstructed electron channel using the jet algorithm.

Channel $2\mu 1e + X$	ZZ	$Zb\bar{b}$	Zb	WZ	$t\bar{t}$
Selection ϵ (%)	4.3±0.13	$(1\pm1)\times10^{-3}$	$(2\pm2)\times10^{-3}$	$(6\pm6)\times10^{-3}$	$(2.5\pm2.5)\times10^{-4}$
Number of event	2.87±0.1	0.1±0.1	0.3±0.3	0.04±0.04	$(1.5\pm1.5)\times10^{-3}$

Table 8.4. Event yields in 1 fb^{-1} for the $2\mu 1e$ + partially reconstructed electron channel using the topological cluster.

Channel 3e+X	ZZ	$Zb\bar{b}$	Zb	WZ	$t\bar{t}$
Selectionϵ (%)	2.7±0.11	$(3\pm3)\times10^{-3}$	$(2.5\pm2.5)\times10^{-3}$	$(2\pm1)\times10^{-2}$	$(2.5\pm2.5)\times10^{-4}$
Number of event	1.81±0.07	0.3±0.3	0.3±0.3	0.1±0.08	$(1.5\pm1.5)\times10^{-3}$

Table 8.5. Event yields in 1 fb^{-1} for the $3e$ + partially reconstructed electron channel using the topological cluster.

8.6. Systematics

The quantities associated with the signal efficiencies and background estimation are sensitive to systematic mis-estimation for different reasons. The uncertainties that can affect the number of observed events can be grouped into two categories, theoretical and experimental.

8.6.1. Theoretical Uncertainties

The main theoretical uncertainties on the production cross sections arise from the pdf uncertainties. The variation of the pdf's in calculating the cross section of Z pair production is of the order of 4 %; the cross section varies from 14.74 pb in CTEQ6M to 15.32 pb in MRST03.

8.6.2. Experimental Uncertainties

The experimental systematic effects on the $ZZ \rightarrow 4l$ analysis arise from the uncertainties of the luminosity determination, lepton energy scale, and lepton energy resolution.

The material distributions in ATLAS affect the lepton energy reconstruction.

- **Luminosity**

  Precise determination of the luminosity can be achieved by using the W and Z production in their leptonic decays. Thus, the luminosity uncertainties may be controlled to 5% in 1 fb^{-1} [62].

- **Lepton Energy Scale**

  Uncertainties of the energy scale of electrons arise from the EM calibration. In order to estimate the impact of this contribution on our analysis, we varied E_T of the reconstructed electrons by $\pm 1\%$. The impact of the energy scale on our analysis is shown for signal and the main backgrounds in Table 8.6. Our cuts are sensitive to the energy scale by $\pm 2.9\%$ for the signal and $\pm 4.7\%$ for the background.

- **Lepton Energy Resolution**

  To account for the electron energy resolution, I smeared the reconstructed electron energies using a Gaussian distribution. I used the smearing function defined as:

  $$\Delta E_T = 0.1 \times E_T \tag{8.1}$$

  From the performance studies [31], I choose the smearing to be around 10 % of the lepton E_T with a Gaussian distribution. Thus the new E_T of the variable will read:

  $$E_T^{new} = E_T \ (1 + \Delta E_T) \tag{8.2}$$

  The effect of the smearing of the electron energies on our cuts is shown in Table 8.6. As a conclusion, our cuts cause a 2% downward shift on our efficiency due to a worsened energy resolution of the electrons.

- **Material Effects in Electron Efficiency**

  The uncertainties in the knowledge of material in the LAr results in uncertainties in electron efficiency. These systematic effects have a direct effect on the shower-shape

discriminants [31] which are part of the electron identification criteria. The mean energy fraction in a core of 3×7 sampling cells normalized to a window of 7×7 cells is an example of these discriminants. As a result the discriminant power of these cuts is reduced. These effects are found to be rather small [31].

	ϵ_{ZZ} (%)	$\epsilon_{Zb\bar{b}}$ (%)
Energy scale (1%)	$\pm$2.9	$\pm$4.7
Resolution	-2.2	-2.1

Table 8.6. Impact, in %, of the systematic uncertainties on the overall selection efficiencies as obtained for $ZZ \rightarrow 3e +$ "e" and $Zb\bar{b} \rightarrow 3e +$ "e" in the case of topological cluster.

8.7. Sensitivity

Although the significance $\frac{S}{\sqrt{S+B}}$, where S and B are the expected yields of signal and background events respectively, is correlated to the number of observed events in a real experiment, it does not completely represent the true sensitivity of a real experiment. This is because some systematics effects can not be modeled and statistics for signal and backgrounds are low and they are Poisson distributed rather than Gaussian distributed.

8.7.1. Statistical Sensitivity

In order to account for the statistical fluctuation, I ran many pseudo-experiments known as ensembles [58]. The estimates of the number of events for the signal and background ensembles were calculated based on random numbers with a Poisson distribution. The mean of the Poisson distribution should be equal to the number of expected events after selection cuts as shown in Tables 8.4 and 8.5. I defined the significance ρ as following:

$$\rho = \frac{N_{ZZ} + N_{Zb} + N_{WZ} + N_{Zb\bar{b}} - \langle N_{BG} \rangle}{\sqrt{N_{ZZ} + N_{Zb} + N_{WZ} + N_{Zb\bar{b}}}} \tag{8.3}$$

The term $\langle N_{BG} \rangle$ is the average number of events for all background channels for each ensemble. The significance ρ was calculated for many luminosity points ranging from 50 pb^{-1} to 2 fb^{-1} after testing 1000 ensembles for each point. Figure 8.4 shows the significance ρ for two luminosity points, 1 fb^{-1} with a mean of 1.95 and 2 fb^{-1} with a mean of 2.83.

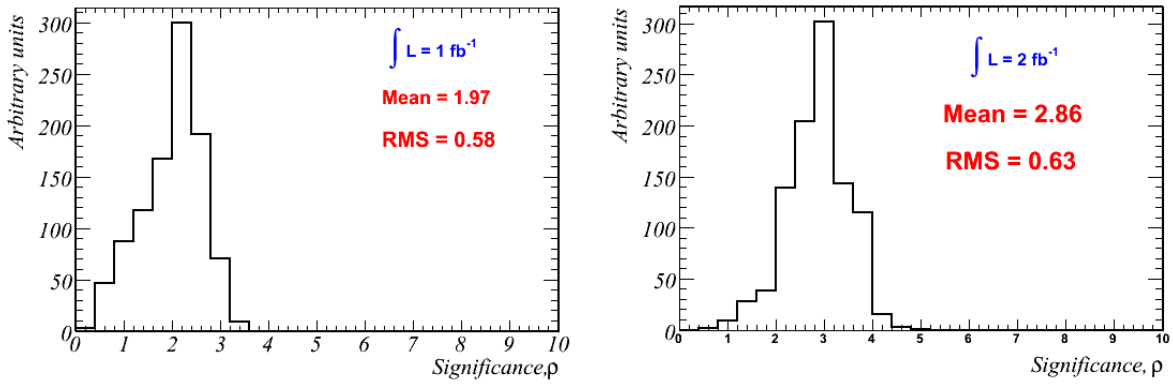

Figure 8.4. Significance, ρ, for integrated luminosities of 1 fb^{-1} (left) and 2 fb^{-1} (right) for the two channels $3e$ + "e" and $2\mu 1e$ + "e".

It is important to get an estimate of the statistical sensitivity over a range of integrated luminosities. For that purpose, I ran a statistical analysis for 40 different integrated luminosity points with 1000 ensembles at each point. The integrated luminosity ranges from 0 to 7 fb^{-1} with increments of 50 pb^{-1}. At each integrated luminosity point, the significance is evaluated over 1000 ensembles and it takes the value of the mean. The expected number of events is scaled from 1 fb^{-1}. Figure 8.5 shows the significance versus integrated luminosity where the curve is fitted. Based on the parameters of the fit, the significance dependence on the integrated luminosity ($\mathcal{L}$) can be expressed by Eq. 8.4. The discovery of ZZ in an exclusive three lepton channel +"e" reaches the discovery limit of $\rho = 5$ at an integrated luminosity of 6.1 fb^{-1}. This is equivalent to a significance $\sigma = \frac{S}{\sqrt{S+B}} = 4.8$.

$$\rho = (2.08 \pm 0.08)\sqrt{\mathcal{L}} - (0.18 \pm 0.15) \tag{8.4}$$

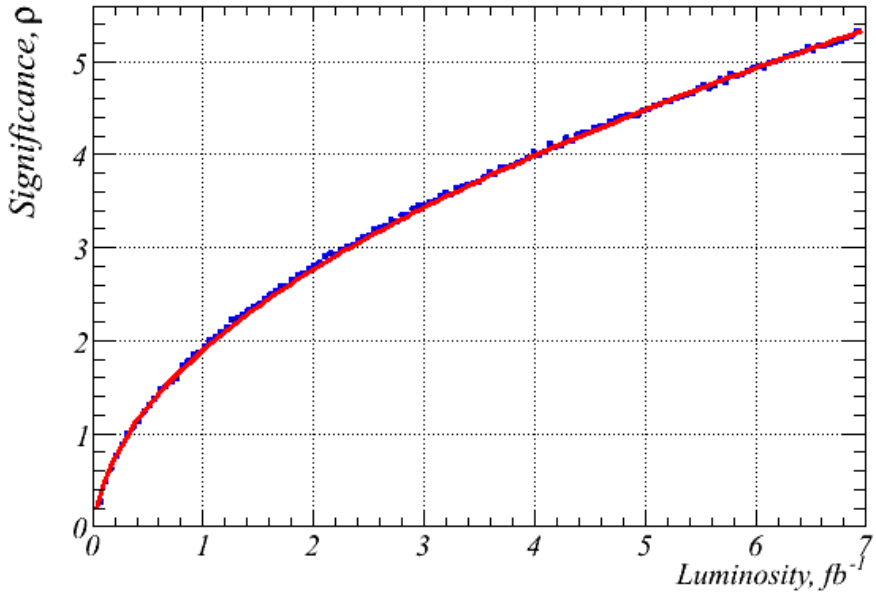

Figure 8.5. Significance, ρ, versus luminosity varying from 0 to 7 fb^{-1}. The data are fitted by the function $p_1\sqrt{\mathcal{L}} + p_0$ (red line). The data points are shown with error bars (blue).

8.7.2. Impact of Systematic Uncertainties

The systematic uncertainties have an impact on the significance as described in the previous section. The number of signal and background events after cuts with statistical and systematic errors are shown in Table 8.7.

Taking into consideration the systematics and statistical uncertainties in the three lepton +"e" channel and the fully reconstructed four lepton channel, the significance is:

process	N_{events}	$\sigma_{statistical}$	$\sigma_{systematics}$
ZZ	4.68	0.12	+0.07/-0.3
$Zb\bar{b}$	0.4	0.3	+0/-0.02
Zb	0.6	0.4	+0/-0.03
WZ	0.14	0.09	+0.002/-0.008
$t\bar{t}$	0.0015	0.002	+0/-0
Total BG	1.1	0.5	+0.002/-0.03

Table 8.7. Number of signal and backgrounds events from $3e$ + cluster and $2\mu 1e$ + cluster channels after all cuts, with statistical and systematic errors.

$$\sigma = \frac{S}{\sqrt{S+B}} = 4.09 \pm 0.02 \tag{8.5}$$

Chapter 9

HIGGS SEARCH

The Higgs boson search in the four lepton channel covers a wide range of the possible Higgs boson mass with a clean signature and low background. In this chapter, I describe a Higgs boson search in the mass range of $m_H \geq 180$ GeV in a three lepton channel, but also provide some indications of how one fares for a lower mass study. In this Analysis, I use the techniques that I developed to partially identify electrons and described in Chapter 7. Moreover, the event selection criteria that I used in the ZZ analysis will be the same criteria applied to the Higgs analysis.

9.1. Three Lepton Selection

I consider the two channels $H \rightarrow ZZ \rightarrow 3e$ and $H \rightarrow ZZ \rightarrow 2\mu 1e$ where one electron is not identified as medium electron. The lepton identification and kinematic selection are similar to those of ZZ diboson as discussed in detail in Chapters 6, 7, and 8. I summarize them very briefly.

9.1.1. Lepton Identification

Reconstructed electrons were required to pass the ATLAS "medium" electron criteria. Muons were identified using the STACO algorithm. As leptons from b quarks in Zb and $Zb\bar{b}$ events are most likely to originate from displaced vertices, the impact parameter significance is used to eliminate those leptons. I require also lepton isolation which I defined in Chapter 5 to reduce the non-isolated leptons which are more likely originating from a background.

9.1.2. Kinematic Selection

The Higgs boson selection in this analysis is based on events with three fully reconstructed leptons in decay samples. A $p_T > 10$ GeV cut was applied for all reconstructed leptons. In the high Higgs boson mass region ($m_H \geq 180$ GeV), The two Z bosons are on-shell, and decay into high p_T leptons. The kinematics of the $H \rightarrow ZZ \rightarrow 4e$ decay leads to a distinct set of momentum distributions when ordered by p_T as shown in Figure 6.3. The background kinematic distributions may be grouped into two categories: those in which the lepton with the third highest p_T originates from a b quark, and those in which it originates from the decay of a heavy boson. These kinematics can be used to further discriminate signal from background. Furthermore, as the WZ and $t\bar{t}$ decays are characterized by large transverse energy $\not{E}_T$, we required $\not{E}_T < 24$ GeV to reduce the backgrounds. We also used the same kinematic variable M_{Zbest} defined in Chapter 6. It is the invariant masses of two lepton combinations from the three reconstructed medium electrons with verified opposite charges which came closest to the nominal Z mass, as shown in Figure 9.1.

The background is still overwhelming as the σ_H is less than σ_{ZZ} by a factor of 12 in the case of $m_H = 180\ GeV$. Again, the need for the unidentified electron is crucial to suppress the background. This mass range has two on-shell $Z's$ which helps suppress the non-ZZ background as in the ZZ search. Moreover, the Higgs is a resonance which makes the Higgs analysis a search for a peak on the top of a ZZ continuum.

9.2. Partially Identified Electron

The jet cone algorithm and topological clusters are the most efficient algorithms in finding the unidentified electron as seen in the ZZ analysis. I will use them in the same manner as described in Chapter 7 to find the unidentified electron. Moreover, particle identification is required on the partially reconstructed electron for better background rejection.

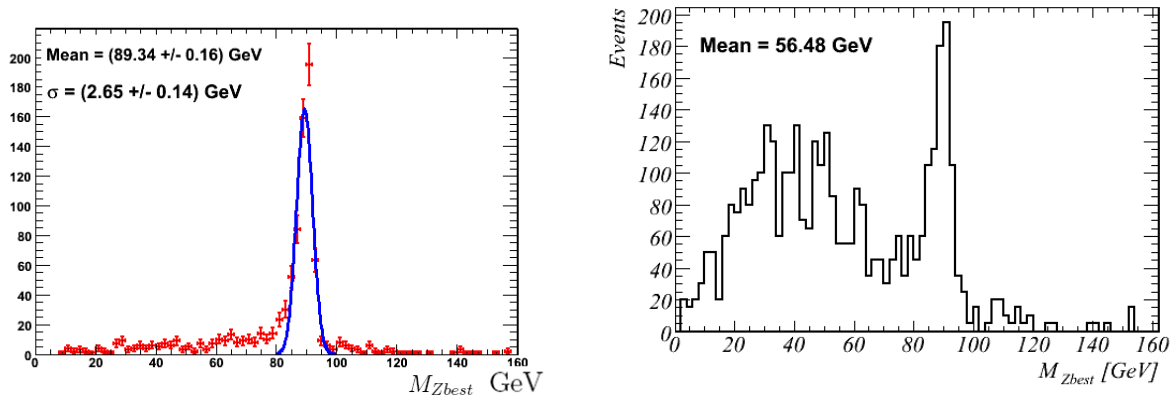

Figure 9.1. M_{Zbest} in the Higgs (m_H = 180 GeV) sample in the three electron channel (left) and M_{Zbest} in the case of the main background $Zb\bar{b}$ where most of the distribution is not in the Z peak (right).

9.2.1. The Second Z Peak via the Jet Algorithm

In a similar way as described in the ZZ analysis, in order to reject the background from b-jets, the partially reconstructed electron was chosen in order to exclude those jets which originated from the b quarks. This was done using the secondary vertex finding in the ATLAS b-tagging algorithm. As a further identification cut on the partially reconstructed electron, I used the EM fraction (EMF). As an electron will leave most of its energy in the EM calorimeter, only partially reconstructed electrons with an EMF higher than 80 % in the barrel (85% in endcap) were selected as shown in Figure 7.6. After the partially identified electron passes the EMF cut, the first leading jet in the event is taken to be the potential unidentified electron as in ZZ analysis. The reader may refer to Chapter 7 for more details. The second Z peak was recovered by the partially identified electron for the $3e$ channel and the other reconstructed electron in the $2\mu 1e$ channel as shown in Figure 9.2.

9.2.2. The Second Z Peak via the Topological Cluster Algorithm

The p_T resolution is comparable to that of the standard sliding window algorithm for the case of the topological cluster algorithm. I show some performance aspects of the

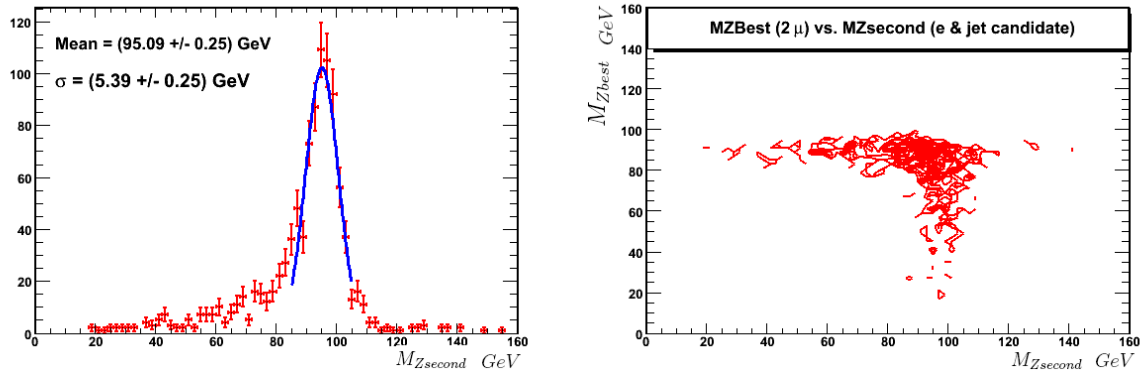

Figure 9.2. The second Z peak formed during an electron and a partially reconstructed electron by the jet algorithm in $H \rightarrow 2\mu 1e$ ($m_H = 180$ GeV) (left). M_{Zbest} (2μ) versus the $M_{Zsecond}$ peak (right).

topological cluster in the Higgs sample in Figure 9.3.

In the particle identification applied to the topological cluster, I used a likelihood method as described in Chapter 7. It is based on four variables previously defined which are the longitudinal and lateral moments, the isolation, and the leading cell energy fraction. Figure 9.4 shows the likelihood discriminant for the Higgs signal and the $Zb\bar{b}$ background as well as the signal efficiency versus fake rate.

We are able to recover a second Z peak in the event; we can therefore apply a 2D cut which requires two Z's in the event within a certain mass window. Figure 9.5 shows the first Z peak in the event (M_{Zbest} variable) versus the second Z peak ($M_{Zsecond}$).

In the Higgs search, I am searching for a resonance. The invariant mass of the three reconstructed leptons and the partially reconstructed electron should result in a peak at the Higgs mass. Figure 9.6 shows the invariant mass of two muons, one fully reconstructed electron and the partially reconstructed electron. Only the Gaussian region of the distribution is considered for the fit.

In order to optimize the likelihood efficiency, I used different probabilities in different η regions as they differ due to the nonuniform cell sizes. Table 9.1 shows the electron efficiency and fake rate for two backgrounds ($Zb\bar{b}$ and WZ) for a likelihood cut of $L > 0.6$

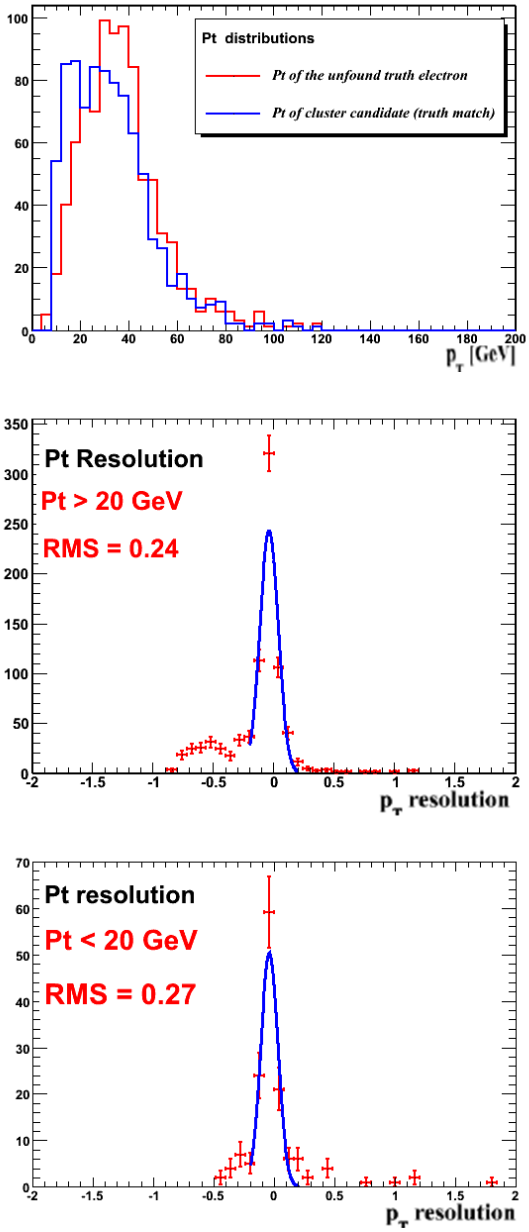

Figure 9.3. p_T of the unfound truth electron matching a topological cluster (upper). Transverse momentum resolution in the case $p_T > 20$ GeV (center) and in the case $p_T < 20$ GeV (bottom). The channel considered is $3e$+"e" for $m_H = 180$ GeV.

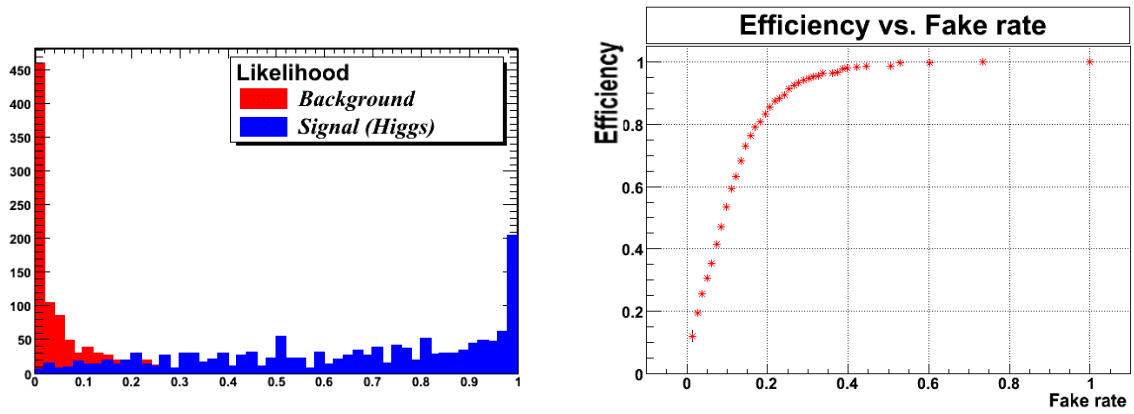

Figure 9.4. The likelihood ratio for Higgs ($m_H = 180$ GeV) and $Zb\bar{b}$ background (left). The signal efficiency versus the fake rate of the main background (right).

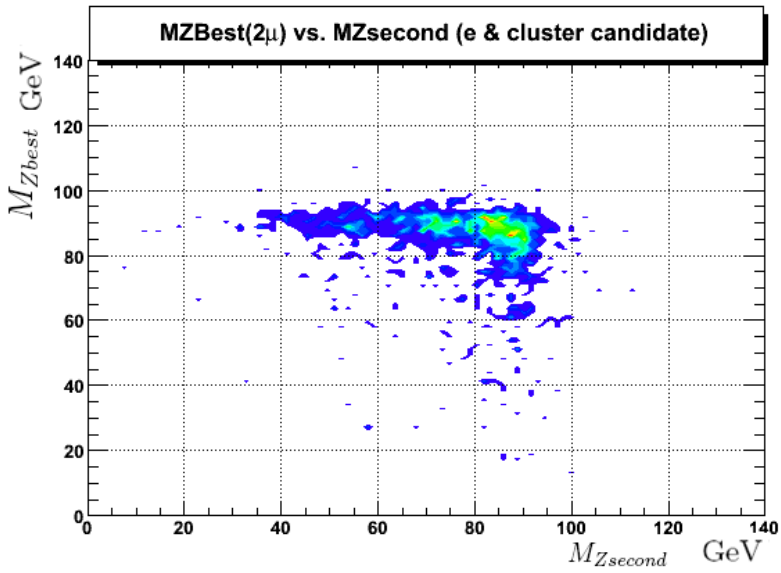

Figure 9.5. M_{Zbest} (2μ) versus the $M_{Zsecond}$ peak. The unidentified electron was found using the topological cluster algorithm and $L > 0.3$ ($m_H = 180$ GeV).

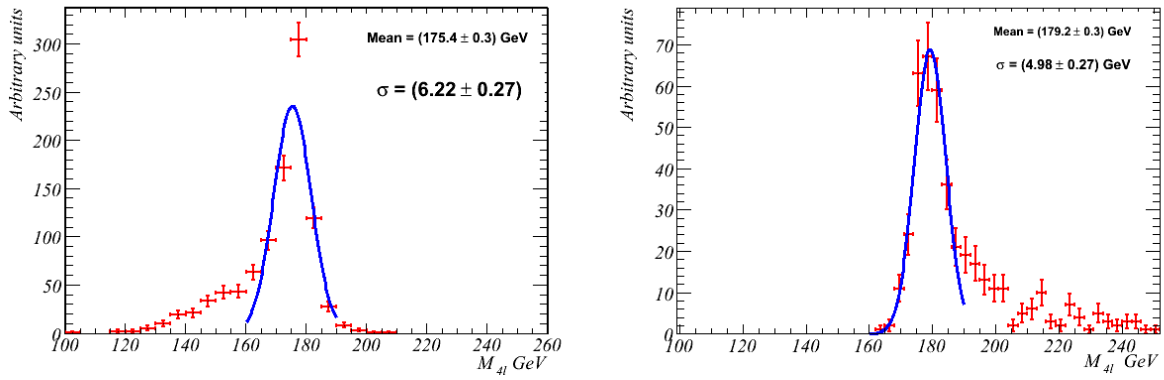

Figure 9.6. The Higgs mass reconstructed by $2\mu 1e$ and a topological cluster matching the truth unfound electron (left). The Higgs mass reconstructed by $2\mu 1e$ and a topological cluster with a likelihood > 0.3 and two Z's in the event (no truth information) (right).

to keep the electron efficiency ∼90% and fake rate ∼15%.

9.3. Event Yields

The signal efficiencies achieved via both algorithms are shown in Table 9.2. I considered three mass points for the Higgs boson, 180 GeV, 200 GeV, and 300 GeV. The topological cluster leads to a higher event selection efficiency than the the jet algorithm. All the errors shown are statistical. The background efficiencies are the same as those discussed in Chapter 8 as I used the same cuts as those of the ZZ analysis. I looked in different mass intervals for each mass point where the Gaussian distribution is. Table 9.3 shows the expected Higgs events in that given window as well as the backgrounds.

Figure 9.7 shows a reconstructed 4-lepton mass for signal and background processes for a normalized luminosity of 30 fb^{-1}. The signal appears as a resonance peak on the top of a background.

Eta regions	Signal efficiency (%)	Zbb fake rate (%)	WZ fake rate (%)
$\|\eta\| < 0.7$	89±1.7	16±1.1	14±1.5
$\|\eta\| > 0.7$ and $\|\eta\| < 1$	88±2.8	14±1.2	15±1.3
$\|\eta\| > 1$ and $\|\eta\| < 1.375$	84±2.9	15±1.3	14±1.4
$\|\eta\| > 1.375$ and $\|\eta\| < 1.9$	83±2.1	17±1.1	17±1.3
$\|\eta\| > 1.9$ and $\|\eta\| < 2.5$	89±1.9	11±1.4	11±1.5
$\|\eta\| > 2.5$ and $\|\eta\| < 3.2$	90±2.8	3±1	2±1
$\|\eta\| > 3.2$	89±1.9	2±1	2±1

Table 9.1. Signal efficiency and background fake rates in different $|\eta|$ ranges for L=0.6 for signal ($m_H = 180$ GeV) and two main backgrounds ($Zb\bar{b}$ and WZ). The low fake rate at high pseudorapidity is due to an $|\eta|$ cut at the generation level.

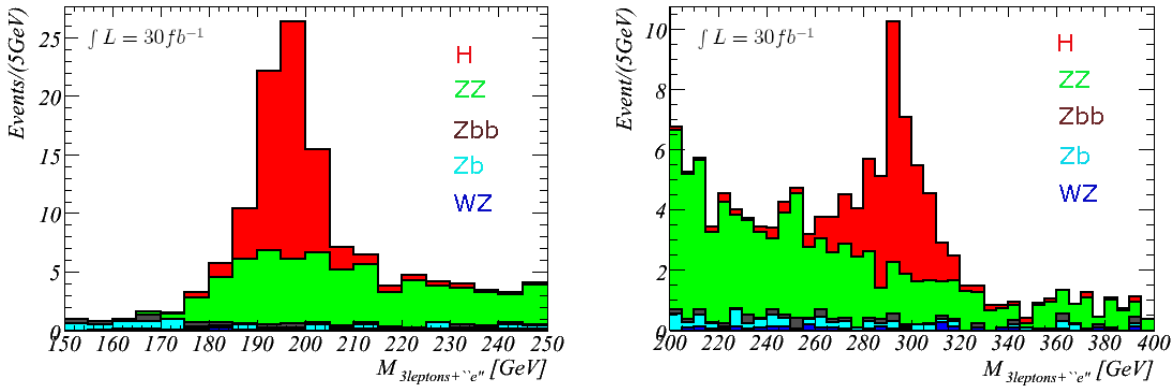

Figure 9.7. Higgs and background channels normalized for an integrated luminosity of 30 fb^{-1}. Left plot is for $m_H = 200$ GeV, right is for $m_H = 300$ GeV.

Selection		Jet algorithm	Topological cluster
180			
$3e$+cluster	selection ϵ (%)	2.1±0.1	2.3±0.1
	N_{evts} $(10fb^{-1})$	1.1±0.001	1.2±0.002
	N_{evts} $(30fb^{-1})$	3.3±0.003	3.7±0.006
$2\mu 1e$+cluster	selection ϵ (%)	3.3±0.1	3.4±0.1
	N_{evts} $(10fb^{-1})$	1.8±0.001	1.8±0.003
	N_{evts} $(30fb^{-1})$	5.4±0.003	5.5±0.009
200			
$3e$+cluster	selection ϵ (%)	2.62±0.07	4.05±0.08
	N_{evts} $(10fb^{-1})$	5.33±0.003	8±0.003
	N_{evts} $(30fb^{-1})$	15.99±0.009	24±0.009
$2\mu 1e$+cluster	selection ϵ (%)	4.71±0.09	4.95±0.09
	N_{evts} $(10fb^{-1})$	9.64±0.004	9.9±0.004
	N_{evts} $(30fb^{-1})$	28.92±0.012	29.7±0.012
300			
$3e$+cluster	selection ϵ (%)	3.1±0.1	4.3±0.2
	N_{evts} $(10fb^{-1})$	3.99±0.003	5.7±0.008
	N_{evts} $(30fb^{-1})$	11.97±0.009	17.1±0.016
$2\mu 1e$+cluster	selection ϵ (%)	4.4±0.2	4.7±0.2
	N_{evts} $(10fb^{-1})$	5.86±0.01	6.23±0.009
	N_{evts} $(30fb^{-1})$	17.58±0.02	18.69±0.018

Table 9.2. Summary table of signal selection efficiencies and expected number of events for 10 fb^{-1} and 30 fb^{-1} in both channels using the topological cluster algorithm and jet algorithm to partially reconstruct the unidentified electron for three points with Higgs masses of ($m_H = 180$, $m_H = 200$, and $m_H = 300$ GeV).

Mass (GeV)		**180**	**200**	**300**
Selection		in (175-185)GeV	in (190-210)GeV	in (290-310)GeV
	Higgs	1.55	14	6.21
	ZZ	1.98	7.54	2.08
$3e$+cluster	$Zb\bar{b}$	0.18	0.11	0.3
&	Zb	0.27	0.24	0.36
$2\mu 1e$+cluster	WZ	0.1	0.03	0.06
	Total BG	2.53	8.26	2.46

Table 9.3. Event yields for 10 fb^{-1} in signal events and backgrounds

9.4. Systematics

The systematics affecting the Higgs analysis are similar to those of the ZZ analysis. I see that my cuts are sensitive to the energy scale and to the energy resolution.

	$\epsilon_{m_H=200\ GeV}$ %	$\epsilon_{m_H=300\ GeV}$ %	$\epsilon_{Zb\bar{b}}$ %
Energy scale (1%)	$\pm$2.2 %	$\pm$0.2 %	$\pm$4.7 %
Resolution	-6.6 %	-5.3 %	-2.1 %

Table 9.4. Impact, in % of the systematic uncertainties on the overall selection efficiencies as obtained for $H \rightarrow 3e +$ "e" (200 GeV and 300 GeV in masses) and $Zb\bar{b} \rightarrow 3e +$ "e".

9.5. Significance and Sensitivity

As the Higgs search will be a resonance search analysis, we looked in certain mass intervals for each Higgs mass point to evaluate the significance $\frac{S}{\sqrt{S+B}}$ for 10 fb^{-1}. The results are shown in Table 9.5.

Moreover, a combination of the three lepton channel+"e" search with the four fully reconstructed lepton search [51] improves the significance. The results are shown in Table 9.6. For the $m_H = 200$ GeV, the significance increases from 6.19 to 7.07 which is an improvement of 12.44%. Moreover, to reach 5"σ" with the four fully reconstructed leptons,

Mass (GeV)		**180**	**200**	**300**
Selection		in (175-185)GeV	in (190-210)GeV	in (290-310)GeV
Significance	$\frac{S}{\sqrt{S+B}}$	0.76	2.96	2.1

Table 9.5. Significance for 10 fb^{-1} in signal events and backgrounds.

Higgs mass (GeV)	180	200	300
Expected signal events (4lepton channel)	13.2	56.6	31.5
Expected background events (4lepton channel)	8.9	26.77	10.1
Significance (4lepton channel)	2.80	6.19	4.88
Combined significance (4l and 3l+"e")	2.88	7.07	5.45

Table 9.6. Number of selected events for signal and background for the combination of the four lepton channels ($4e$, 4μ, $2e2\mu$) [51] and significance ($\frac{S}{\sqrt{S+B}}$) compared with those of the three lepton channel and a cluster for an integrated luminosity of 10 fb^{-1}

we need a luminosity of 6.8 fb^{-1}. However, by including the three lepton channel, we can reach the 5"σ" significance with luminosity of 5.4 fb^{-1}; this is to say 21% less data needed.

In order to account for the statistical fluctuations as we described in the ZZ analysis by running pseudo-experiments, I calculate the significance ρ for Higgs of masses 200 GeV and 300 GeV as shown in Figure 9.8.

9.6. Low Mass Higgs Search

The most challenging mass region in the $H \rightarrow ZZ \rightarrow 4l$ search is between $130 - 160$ GeV where one of the Z bosons is off-shell giving low p_T leptons. An attempt for a search for the Higgs boson at low mass was done by using a Monte Carlo sample at the Higgs mass of 150 GeV. In that mass range, we require to have only one on-shell Z in the event. Using the topological cluster to partially reconstruct the unidentified electron, we achieved a signal efficiency of 3.5± 0.2% for the $2\mu 1e$ + "e" and 3.2± 0.1 for the $2\mu 1e$ + "e" for a likelihood cut of 0.6. Given that the requirement of only one on-shell Z in the

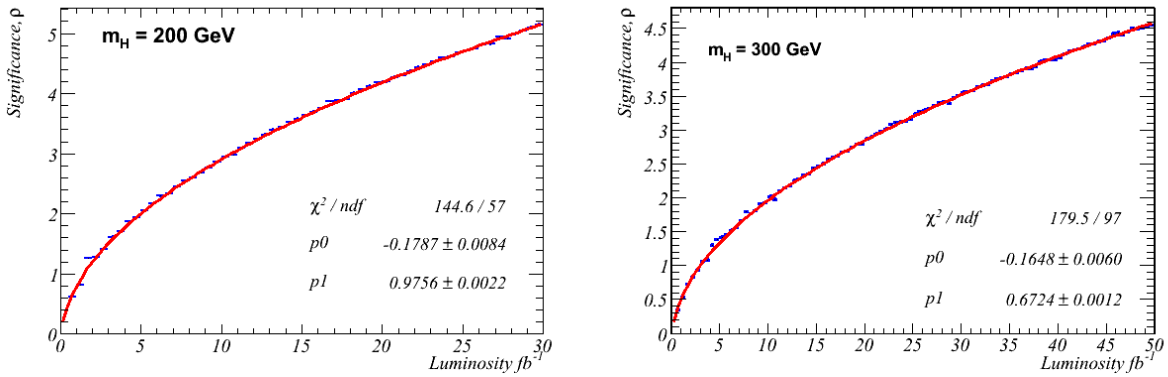

Figure 9.8. Significance versus luminosity in case of Higgs mass of 200 GeV (left) and 300 GeV (right).

event, we expect that the background will be significant. The ZZ backgrounds are lower than at high mass. However, I estimate $\frac{S}{B} \sim 1$ at $m_H = 150$ GeV with this selection.

Chapter 10

CONCLUSION

An exclusive $ZZ \rightarrow 3l$ analysis has been conducted using a Monte Carlo data sample for a pp collision at a center of mass energy of 14 TeV. The presented results, for 1 fb^{-1}, show an acceptance gain of 36% with respect to the $ZZ \rightarrow 4l$ channel. Thus, the significance defined as $\frac{S}{\sqrt{S+B}}$ increases from 3.6 to 4.1. The search was done by considering ZZ events where only three leptons were reconstructed, $3e$ or $2\mu 1e$, and one electron does not get fully reconstructed. I used different algorithms which include the forward region ($|\eta| > 2.5$) to find the missing electron. Moreover, I recover also an electron that has failed one of the criteria required by the standard electron algorithm in the central region. Possible backgrounds in the three lepton channel are due to $Zb\bar{b}$, Zb, $t\bar{t}$, and WZ processes. A 5"σ", where $\sigma = \frac{S}{\sqrt{S+B}}$, can be reached at 2 fb^{-1} with the four fully reconstructed leptons. However, a combined results of the three lepton channel and the four fully reconstructed leptons reduces the required integrated luminosity to 1.5 fb^{-1} which is 25% less data needed.

The Higgs search is also considered in this thesis. We emphasized a Higgs search in the mass range of $m_H \geq 180$ GeV in the channel $H \rightarrow ZZ \rightarrow 4l$, where the two Z's are on-shell. This allowed us to use the same event selection criteria used in the case of a ZZ diboson. The results shown are for an integrated luminosity of 10 fb^{-1}. For a Higgs mass of 200 GeV, the 5"σ" as defined above can be reached at 6.8 fb^{-1} with the four fully reconstructed leptons. However, a combined results of the three lepton channel and the four fully reconstructed leptons reduces the required integrated luminosity to 5.4 fb^{-1} which is 21% less data needed. The most challenging mass region in the $H \rightarrow ZZ \rightarrow 4l$ search is between $130 - 150$ GeV where one of the Z bosons is off-shell giving low p_T leptons. Although further work is needed, $\frac{S}{B} \sim 1$ can already be achieved and better

understanding of the background in that region of the search is very crucial.

A test of the partially identified electron technique is possible in early data by considering single Z boson as its production cross section is high. One can require stringent criteria on one electron, "tag", and probe for the missing electron in $Z \rightarrow e^+e^-$ using the techniques developed in this thesis. Moreover, this will allow one to calculate efficiencies of different algorithms using real data.

REFERENCES

[1] Gorini, Rosanna, Journal of the International Society for the History of Islamic Medicine 2 (4)

[2] Steffens, Bradley (2006), Ibn al-Haytham: First Scientist, Morgan Reynolds Publishing, ISBN 1-59935-024-6.

[3] Carl B. Boyer, A History of Mathematics, Second Edition (Wiley, 1991)

[4] Galileo Galilei. Dialogue Concerning the Two Chief World Systems, 1632

[5] Sir Isaac Newton. Philosophiæ Naturalis Principia Mathematica, first edition (1687)

[6] Maxwell, James Clerk. A dynamical theory of the electromagnetic field (1864)

[7] Albert Einstein (1905) Zur Elektrodynamik bewegter Körper, Annalen der Physik 17: 891

[8] A. Einstein, Annalen der Physik. 18:639, 1905 (Translated by Perrett and Jeffery)

[9] Erwin Schrdinger, Annalen der Physik, (Leipzig) (1926)

[10] W. Heisenberg, ber quantentheoretishe Umdeutung kinematisher und mechanischer Beziehungen, Zeitschrift fr Physik, 33, 879-893, 1925 (received 29 July 1925). [English translation in: B. L. van der Waerden, editor, Sources of Quantum Mechanics (Dover Publications, 1968) ISBN 0-486-61881-1

[11] F. Englert and R. Brout (1964). Broken Symmetry and the Mass of Gauge Vector Mesons. Phys. Rev. Lett.13.321.

[12] Peter W. Higgs (1964). Broken Symmetries and the Masses of Gauge Bosons. Phys. Rev. Lett.13.508.

[13] G. S. Guralnik, C. R. Hagen, and T. W. B. Kibble (1964). Global Conservation Laws and Massless Particles. Phys. Rev. Lett.13.585.

[14] Gerald S. Guralnik (2009). The History of the Guralnik, Hagen and Kibble development of the Theory of Spontaneous Symmetry Breaking and Gauge Particles.International Journal of Modern Physics A24: 26012627.

[15] S. Weinberg, S. Phys. Rev. Lett. 19 1264-1266 (1967).

[16] F. Halzen, A.D. Martin. Quarks and Leptons: An Introductory Course In Modern Particle Physics. John Wiley and Sons Inc., 1984.

[17] P. W. Higgs, Phys. Rev. 145, 1156 (1966).

[18] Ta-Pei Cheng, Ling-Fong Li. Gauge Theory of elementary Particle Physics. Oxford science publications, 1984.

[19] B. W. Lee, C. Quigg, and H. Thacker, Phys. Rev. D16, 1519 (1977)

[20] K. Hagiwara, R. D. Peccei, D. Zeppenfeld, and K. Hikasa, Nucl. Phys. B282, 253 (1987)

[21] G.J. Gounaris, J. Layssac, and F.M. Renard, "Signatues of the anomalous $Z\gamma$ and ZZ production at lepton and hadron colliders", Phys. Rev. D 61, 073013 (2000).

[22] G.J. Gounaris, J. Layssac, and F.M. Renard, "New and standard physics contributions to anomalous Z and γ self-coupling", Phys. Rev. D 62, 073013 (2000).

[23] http://lepewwg.web.cern.ch/LEPEWWG/

[24] http://lepewwg.web.cern.ch/LEPEWWG/plots/summer2008/

[25] Combined CDF and DZero Upper Limits on Standard Model Higgs-Boson Production with up to 4.2 fb^{-1} of Data arXiv.org arXiv:0903.4001

[26] E. W. N. Glover and J. J. van der Bij "Vector Boson Production via Gluon Fusion," Phys. Lett. B219,4 488-492 (1989)

[27] T. Binoth, N. Kauer, P. Mertsch, Gluon-induced QCD Corrections to $pp \to ZZ \to l\bar{l}l'\bar{l}'$ arXiv:0807.0024v1 [hep-ph]

[28] U. Baur and D. Rainwater "Probing neutral gauge self-interaction in ZZ production at hadron colliders," Phys. Rev. D62:113011 (2000)

[29] Samira Hassani com-phys-2002-013

[30] M. Kobayashi, T. Maskawa, CP violation in the renormalizable theory of weak interaction, Prog. Theor. Phys, (1973)

[31] M. Aharrouche et al. Reconstruction and Identification of Electrons ATL-PHYS-PUB-2009-004 (2009).

[32] J. Hoffman, V. Maleev, D. Froidevaux, "Electrons in cracks and TR performance for 12.0.4", Talk given at ATLAS egamma working group, December 14, 2006 http://indicobeta.cern.ch/getFile.py/access?contribId=3&resId=1&materialId=slides&confId=a058238

[33] J. Hoffman, H to ZZ to 3l(+1). Talk given at ATLAS Higgs working group, November 16, 2007 http://indicobeta.cern.ch/getFile.py/access?contribId=6&resId=1&materialId=slides&confId=24020

[34] D.A. Edwards, M.J. Syphers. An Introduction to the Physics of High Energy Accelerators, Wiley series, (1993) ISBN 0-471-55163-5.

[35] ATLAS Collaboration, Detector and Physics Performance Technical Design Report, CERN/LHCC/99-14/15 (1999).

[36] ATLAS Collaboration, The ATLAS Experiment at the CERN Large Hadron Collider, ATL-COM-PHYS-2007-042 (2007) submitted to JINST

[37] M. Aleksa et al. 2004 ATLAS Combined Testbeam:Computation and Validation of the Electronic Calibration Constants for the Electromagnetic Calorimeter ATL-LARG-PUB-2006-003

[38] A. Kasmi, R. Ishmukhametov and R. Daya Ramp analysis presentations presented at the LAr meetings in summer of 2007. August 16, 2007 http://indicobeta.cern.ch/getFile.py/access?contribId=3&resId=1&materialId=slides&confId=17833

[39] Calorimter Trigger Groups, JINST 3 (2008) P03001

[40] Central Trigger Group, IEEE Trans. Nucl. Sci. 52 (2005) 3211-3215.

[41] ATLAS Collaboration, Muon Spectrometer Technical Design Report, CERN/LHCC/97-022,(1997)

[42] S. Veneziano et al., IEEE Trans. Nucl. Sci. 51 (2004) 1581-9

[43] J.M. Butterworth, Jeffrey R. Forshow, M.H. Seymour, Multiplication interactions in photoproduction at HERA, Z.Phys.C72:637-646,1996.

[44] S. Frixione and B. R. Webber, "The MC@NLO 3.4 Event Generator" *http* : *//www.hep.phy.cam.ac.uk/theory/webber/MCatNLO/MCatNLO*$_m$*an*34*.pdf*

[45] T. Sjostrand, S. Mrenna, P. Skands PYTHIA Physics and Manual hep-ph/0603175

[46] G. Corcella "HERWIG 6.5 Release Note" hep-ph/0210213

[47] S. Frixione and B. R. Webber, "Matching NLO QCD Computations and Parton Shower Simulation," JHEP 0206 (2002) 029 [hep-ph/0204244].

[48] B. P. Kersevan and E. Richter-Was "The Monte Carlo Event Generator AcerMC 2.0 with Interfaces to PYTHIA 6.2 and HERWIG 6.5" [hep-ph/0405247]

[49] http://madgraph.hep.uiuc.edu/

[50] http://cp3wks05.fynu.ucl.ac.be/twiki/pub/Software/HELAS/helas.pdf

[51] C. Anastopoulos et al. Search for the Standard Model $H \to ZZ^* \to 4\ell$ ATL-PHYS-PUB-2009-054 (2009).

[52] https://twiki.cern.ch/twiki/bin/view/Atlas/TapmMainPage

[53] http://geant4.web.cern.ch/geant4/

[54] The ATLAS Collaboration, Inner Detector: Technical Design Report, CERN/LHCC/97-016/017 (1997).

[55] A. Salzburger, The ATLAS Track Extrapolation Package, ATLAS Note ATL-SOFT-PUB-2007-005 (2007).

[56] G. Aad et al., Performance of the ATLAS b-tagging Algorithms. ATL-PHYS-PUB-2009-018.

[57] P. Loch et al., Jet Algorithm Performance in ATLAS.

[58] Search for supersymmetry in a three lepton plus jets signature, Ph.D. thesis 2008

[59] ATLAS Collaboration. EM calorimeter calibration and performance. CSC-EG-6, 2008.

[60] ATLAS Collaboration, G. Aad et al., The ATLAS experiment at the CERN Large Hadron Collider, JINST 3 S08003 (2008).

[61] K. Bachas et al. Dibosons Physics Studies ATL-PHYS-PUB-2009-038 (2009).

[62] M. Dittmar, F. Pauss, D. Zuercher, Phys. Rev. D 56, 7284-7290 (1997).